A Double-walled Aortic Stent-graft for Reduced Impact on Arterial Stiffness and Hemodynamics

A DISSERTATION

SUBMITTED TO THE FACULTY OF THE

UNIVERSITY OF MINNESOTA

BY

Shannen Belle Kizilski

IN PARTIAL FULFILLMENT OF THE REQUIREMENTS

FOR THE DEGREE OF

DOCTOR OF PHILOSOPHY

Adviser:

Professor Victor H. Barocas

March 2021

© Shannen Belle Kizilski 2021

Acknowledgements

I would like to thank everyone who contributed to my completion of this thesis project. My adviser Victor Barocas formulated this design-based project to accommodate my interest in medical device design, despite it being a topic outside of his comfort zone. He supported the direction that I wanted to take the project, and he offered valuable insights at critical decision points. Victor always prioritized my personal growth, and he pushed me to identify a career path that I would find most rewarding. Rumi Faizer, a vascular surgeon at the University of Minnesota, originally identified the problem with stiff stent-grafts in-clinic and has been the positive energy and motivator behind this project. Omid Amili and Filippo Coletti advised me on the fluid mechanics aspects of the project, and Omid was particularly helpful when I was setting up and troubleshooting the flow loop experiments.

Members of my preliminary and final exam committees – Victor Barocas, Jim Van de Ven, Tim Kowalewski, Pat Alford, Filippo Coletti, Will Durfee, and Bob Tranquillo – took the time to understand my project and to provide thoughtful feedback that helped me to critically review and revise my work.

The Clinical and Translational Science Institute at the University of Minnesota accepted me into their first cohort of TL1 scholars, an opportunity that enriched my graduate school career by exposing me to best practices in translational science across a range of academic fields and by giving me protected time to focus on the translational potential of my project. The Anatomy Bequest Program at the University of Minnesota generously provided critical resources for my experimental work, including pumps and tubing for my flow loop studies. The Minnesota Supercomputing Institute provided me with access to computational resources that I used to conduct fluid flow simulations at various stages of my project.

Abstract

The aorta is the largest artery in the body, responsible for delivering oxygenated blood from the heart to the vital organs. The elasticity of the aortic wall allows it to play a critical role as a capacitor for the arterial system, regulating blood pressure and providing steady blood flow during cardiac diastole. Loss of this capacitive function, either due to age-related aortic stiffening or due to placement of a rigid stent-graft for disease treatment, can lead to significantly increased risk of cardiovascular, and all-cause, morbidity and mortality. In this thesis, a novel double-walled aortic stent-graft (DWSG) design is introduced that aims to restore the capacitive function of the aorta through use of a compressible gas layer. This concept was evaluated through a series of computational and *in vitro* experimental models, each of which provided new insights into the various design considerations that affect device performance. Across all models, the DWSG led to reduction in one or more measures of blood pressure compared to a standard stent-graft, with increasing effect as the amount of contained gas was increased. In measurements of pulse wave velocity, which provide an estimate of arterial stiffness, the DWSG again demonstrated the ability to reduce values compared to a standard stent-graft. In models with a very stiff vessel wall, the DWSG exhibited pulse wave velocity measurements significantly lower than the unstented vessel. Design details of the DWSG were refined across the various studies, and finally an optimization study was conducted to identify potential configurations for the gas layer. In the final chapter, the potential impact of the DWSG is discussed and next steps are addressed.

Table of Contents

List of Tables ..... **viii**

List of Figures ..... **ix**

Chapter 1: Background & Project Introduction **1**

1.1 The Aorta is a Reservoir **1**

1.1.1 Anatomy and Physiology 1

1.1.2 Regional Mechanical Properties 2

1.1.3 Hemodynamics 3

1.1.4 Blood Pressure 5

1.2 Aortic Pathophysiology **6**

1.2.1 Aortic Stiffness 6

1.2.2 Hypertension 8

1.2.3 Aortic Aneurysm and Dissection 10

1.3 The Role of Stent-grafts in Aortic Disease **11**

1.4 An Opportunity to Improve Aortic Interventions **13**

1.5 Research Aims & Outcomes **15**

Chapter 2: Parameters that Impact Aortic Stiffness and Blood Pressure **17**

2.1 Introduction **17**

2.2 Methods **18**

2.2.1 Modified Windkessel Model 18

2.2.2 Sweep of Model Parameters 19

2.2.3 Study Design 21

2.3 Results & Discussion **22**

2.3.1 Effects of Resistance and Capacitance on Blood Pressure 22

2.3.2 The Physical Tradeoffs between Resistance and Capacitance 25

Chapter 3: Double-Walled Stent-Graft: Proof of Concept 28

3.1 Introduction 28

3.2 Device Design 31

3.2.1 Design Concept 31

3.2.2 Initial Prototypes 34

3.3 Experimental Methods 34

3.3.1 Static Inflation 35

3.3.2 Flow Loop 36

3.3.3 Experimental Design 39

3.4 Computational Methods 39

3.4.1 DWSG Finite Element Model 40

3.4.2 Windkessel Model 42

3.4.2.1 Flow Loop Model 42

3.4.2.2 Arterial Model 44

3.5 Summary of Results 46

3.6 Characterizing the DWSG 46

3.6.1 DWSG Capacitance 46

3.6.2 DWSG Resistance 50

3.7 Dynamic Behavior 50

3.7.1 Flow Loop Measurements 50

3.7.2 Physiologic Predictions with the Windkessel Model 52

3.8 Discussion 56

3.8.1 Double-walled Stent-graft (DWSG) Design 56

3.8.2 DWSG Capacitance and Resistance 57

3.8.3 Pressure Reduction with the DWSG 58

Chapter 4: Effect of the Double-Walled Stent-Graft on Pulse Wave Velocity .. 60

4.1 Introduction 60

4.2 Computational Methods 61

4.2.1 Computational Model 61

4.2.2 Stent-graft Properties 62

4.2.3 Boundary Conditions 63

4.2.4 Study Design 64

4.3 Experimental Methods 64

4.3.1 Stent-graft Prototypes 64

4.3.2 Flow Loop System 65

4.3.3 Study Design 67

4.4 FSI Results 67

4.4.1 Approximated DWSG Properties 67

4.4.2 Pulse Wave Velocity and Blood Pressure 68

4.5 Flow Loop Results 70

4.5.1 Pulse Wave Velocity 70

4.5.2 Systolic Pressure 71

4.5.3 Pulse Pressure 72

4.6 Discussion 75

Chapter 5: Shape Optimization of the Double-Walled Stent-Graft Gas Layer. 77

5.1 Introduction 77

5.2 Device Design 79

5.3 Design Optimization Metrics 82

5.3.1 Gas Volume 82
5.3.2 Flow Resistance 82
5.3.3 Time-Averaged Wall Shear Stress 83
5.3.4 Oscillatory Shear Index 83
5.3.5 Relative Residence Time 84
5.4 Device Models 84
5.4.1 Longitudinal Profile (**Figure 5.2**) 84
5.4.1.1 Computational Domain 84
5.4.1.2 Profile Parameterization 86
5.4.1.3 Geometric Constraints 86
5.4.1.4 Model Parameters and Boundary Conditions 87
5.4.2 Circumferential Discretization (**Figure 5.3**) 87
5.4.2.1 Domain 87
5.4.2.2 Profile Parameterization 88
5.4.2.3 Geometric Constraints 88
5.4.2.4 2D Performance Metrics 88
5.5 Optimization Setup 89
5.5.1 Longitudinal Profile 89
5.5.1.1 Objectives 89
5.5.1.2 Constraints 91
5.5.1.3 Algorithm 91
5.5.2 Circumferential Discretization 92
5.5.2.1 Objectives 93
5.5.2.2 Constraints 94

5.5.2.3 Algorithm 94

5.6 Implementation 95

5.6.1 Longitudinal Profile 95

5.6.2 Circumferential Discretization 98

5.7 Results 99

5.7.1 Longitudinal Profile 99

5.7.1.1 Evaluated Objective Space 99

5.7.1.2 Pareto Front – Flow Field 102

5.7.2 Circumferential Discretization 106

5.8 Discussion 108

5.8.1 Longitudinal Profile 108

5.8.2 Circumferential Discretization 110

5.8.3 Conclusions 110

Chapter 6: Conclusions and Future Directions 112

6.1 Summary of Findings 112

6.2 Potential Impact of the DWSG 113

6.3 Next Steps in Device Development 115

6.3.1 Deployment 115

6.3.2 Materials & Durability 116

6.3.3 Validation Study in Cadaveric Aortas 117

Bibliography 119

List of Tables

Chapter 2: Parameters that Impact Aortic Stiffness and Blood Pressure

Table 2.1: Breakdown of aortic capacitance …….. 20

Chapter 3: Double-Walled Stent-Graft: Proof of Concept

Table 3.1: DWSG configurations tested in static and flow loop experiments …… 39

Table 3.2: Properties of the aorta found in literature …….. 45

Table 3.3: Coefficients for the linear models relating normalized peak and pulse pressures to design variables ……. 52

Table 3.4: Capacitance and resistance measurements of the DWSG used for physiologic predictions in the Windkessel model ……. 54

Chapter 4: Effect of the Double-Walled Stent-Graft on Pulse Wave Velocity

Table 4.1: Storakers model parameters for the gas layer solid analog …….. 68

Chapter 5: Shape Optimization of the Double-Walled Stent-Graft Gas Layer

Table 5.1: List of constraints enforced for the 3D axisymmetric optimization ……. 92

Table 5.2: Constraints enforced for the 2D axial cross section optimization …… 94

Table 5.3: Artificial optimization results for unmet constraints ……. 96

Table 5.4: Mesh parameters used for each 3D axisymmetric model ……. 97

Table 5.5: Parameters used to run CFD simulations with SimVascular's svSolver …….. 98

List of Figures

Chapter 1: Background & Project Introduction

Figure 1.1: Anatomy and branches of the aorta ……..... 2
Figure 1.2: Diagram of carotid-femoral pulse wave velocity measurement in a patient …..... 5
Figure 1.3: Pressure wave diagram …….. 6
Figure 1.4: Blood pressure levels and their associated hypertension diagnoses …….. 9
Figure 1.5: Stent-graft diagram ……..... 12

Chapter 2: Parameters that Impact Aortic Stiffness and Blood Pressure

Figure 2.1: Modified Windkessel model …….. 19
Figure 2.2: Results of Windkessel parameter sweep …… 23
Figure 2.3: Effect of a standard stent-graft on blood pressure ……. 24

Chapter 3: Double-Walled Stent-Graft: Proof of Concept

Figure 3.1: Proof-of-concept study flowchart …….. 31
Figure 3.2: Double-walled stent-graft (DWSG) preliminary prototype …….. 33
Figure 3.3: Experimental flow loop diagram …… 37
Figure 3.4: Calculation of DWSG capacitance ……..... 41
Figure 3.5: Windkessel model and input flow rates ……. 43
Figure 3.6: DWSG static finite element model ……. 48
Figure 3.7: Capacitance measurements of the DWSG ……. 49
Figure 3.8: DWSG flow resistance …….. 51
Figure 3.9: Flow loop pressure measurements ……. 53
Figure 3.10: Windkessel pressure predictions …….. 55

Chapter 4: Effect of the Double-Walled Stent-Graft on Pulse Wave Velocity

Figure 4.1: FSI model configuration ……..…… 63
Figure 4.2: Flow loop and DWSG prototype for PWV measurement …….. 66
Figure 4.3: Approximating the DWSG gas layer as a solid ……. 68
Figure 4.4: PWV and pressure FSI results …… 69
Figure 4.5: FSI flow field at DWSG inlet …… 70
Figure 4.6: Flow loop PWV measurements …….. 73
Figure 4.7: Flow loop pressure measurements ……. 74

Chapter 5: Shape Optimization of the Double-Walled Stent-Graft Gas Layer

Figure 5.1: Diagram of DWSG profiles ……..…….. 80
Figure 5.2: CFD model for longitudinal profile optimization …….. 85
Figure 5.3: Sequence for generation of 2D axial cross section models …… 87
Figure 5.4: Flowchart of optimization procedure for the longitudinal profile ……. 90
Figure 5.5: Flowchart of optimization procedure for the circumferential gas layer discretization …… 93
Figure 5.6: Plot of decaying change in objectives for circumferential gas layer discretization 95
Figure 5.7: Optimization results for the longitudinal profile …… 100
Figure 5.8: Map of RRT constituent parameters onto the normalized objective space …… 101
Figure 5.9: Map of additional hemodynamic parameters onto the normalized objective space 102
Figure 5.10: Velocity streamlines and pressure for selected CFD simulations ……. 104
Figure 5.11: TAWSS and OSI maps for selected CFD simulations ……. 105
Figure 5.12: Pareto front for circumferential gas layer optimization …… 107
Figure 5.13: Histograms of the design variables in the pareto front for circumferential profile optimization ……. 108

Chapter 1

Background & Project Introduction

The cardiovascular system works tirelessly to circulate over 7,200 liters of blood per day, providing organs and tissues with the nutrients they need to live and function [1]. Although the heart gets most of the credit for this work, several vascular structures contribute both actively and passively to the movement of blood throughout the body. In this introduction, I draw attention to the critical role of the aorta in controlling arterial blood flow and how disruption to this function can lead to significant cardiovascular morbidity. In this thesis, I propose a new stent-graft design that is intended to restore the aorta's flow-control function through the inclusion of a compressible gas layer that passively expands and contracts with changing blood pressure.

1.1 The Aorta is a Reservoir

1.1.1 Anatomy and Physiology

The aorta is the largest artery in the vascular system, originating at the aortic valve, at the outlet of the heart's left ventricle, and running through the thoracic cavity into the abdomen, where it eventually bifurcates to form the iliac arteries (**Fig 1.1**). The aorta is divided into thoracic and abdominal regions corresponding to anatomical location, with the thoracic region further divided into ascending, arch, and descending segments based on orientation. The coronary arteries, which supply the heart muscle with oxygenated blood, branch off of the ascending thoracic aorta just distal to the aortic valve. Along the arch, a few key vessels branch off to deliver blood to the head and arms. Notable branches from the abdominal aorta include the renal arteries, the hepatic artery, and mesenteric arteries. Although there are no major branches from the descending thoracic aorta, several smaller vessels originating in this segment feed structures such as the diaphragm, chest wall, and spine.

The heart can be thought of as a positive displacement pump because it works to deliver the required volume of blood during each cardiac cycle without much response to the resulting pressures. Due to its direct connection to the left ventricle, the ascending aorta receives the entire bolus of blood ejected from the heart during cardiac systole, a quantity referred to as the stroke volume. In adults, stroke volume ranges from 50 to 100 mL depending on activity level and cardiovascular health [2]. Although the cardiac cycle normally has a period between 0.5 and 1 second, the stroke volume is delivered to the aorta only during systole, which comprises about one third of this period. As a result, flow rates in the ascending aorta often reach peak values of 500 mL/s, or about 90 cm/s velocity.

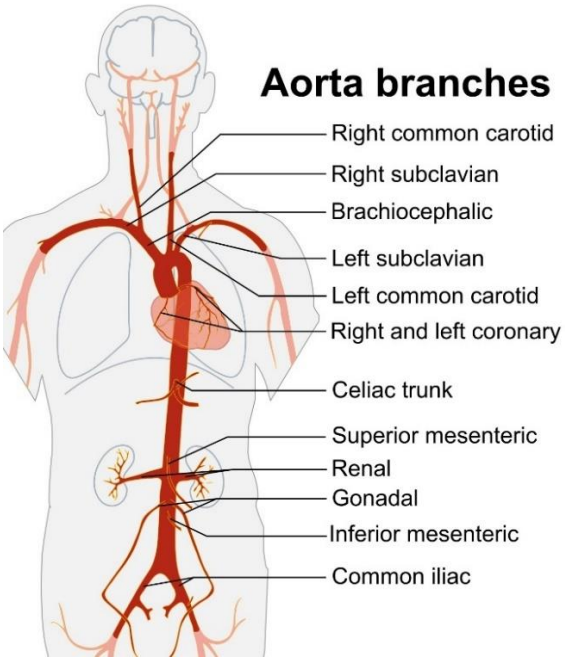


Figure 1.1: Anatomy and branches of the aorta. Image by Mikael Häggström. This file is licensed under the Creative Commons Attribution-Share Alike 3.0 Unported license.

1.1.2 Regional Mechanical Properties

The aortic wall in a young adult is composed of roughly 20% collagen and 40% elastin (dry weight), with the remaining mass consisting of smooth muscle cells and the surrounding ground matrix [3,4]. Although collagen is about 1000 times stiffer than elastin, the crimped nature of

collagen fibers in the aortic wall allows elastin to dominate the low-strain stiffness of the vessel. As a result, the aorta is highly compliant at low strains and then exhibits a sharp increase in stiffness when the collagen fibers engage at a tissue strain of about 30% [5]. The highest concentration of elastin is found in the ascending aorta, with the elastin level decreasing toward the distal end at the iliac arteries. The lower proportion of elastin in the abdominal aorta causes the tissue in that region to be more than three times stiffer than that of the ascending aorta [6,7]. In a healthy, young person, the ascending aorta undergoes about 11% circumferential strain over the cardiac cycle [8].

1.1.3 Hemodynamics

Much like the mechanical properties, the nature of blood flow in the aorta is highly dependent on the region. Blood exits the heart at a high velocity, causing flow in the ascending aorta to exhibit significantly turbulent behavior [9]. Along the arch, about 30% of the blood volume exits through branching vessels, resulting in lower flow rates in the descending aorta [10]. Although instantaneous velocities cause Reynolds number to peak at about 3400 in the descending aorta, the average value is 1000, which places it in the transitional zone [11]. Velocity is further reduced in the abdominal aorta after 70% of the remaining blood volume is diverted to the kidneys, liver, and other abdominal organs [10]. The moderate Reynolds numbers and regional variation in flow along the aorta have led to significant heterogeneity in modeling choices for computational fluid dynamics studies. Many researchers include turbulence models when simulating aortic flow [10,12–15], while others argue that it can reasonably be excluded without invalidating the results [16–20].

The compliance of the aortic wall has a major impact on local and systemwide hemodynamics. Aside from its obvious role as a central conduit in the arterial system, the aorta also acts as a reservoir. When blood rushes into the aorta during systole, the vessel dilates to accommodate the increased blood volume. During diastole, the blood flows out of the aorta into the peripheral vasculature, and the blood pressure and the diameter of the vessel decrease. This storage and release

of blood over the cardiac cycle contributes to steady downstream flow and promotes healthy blood pressure by augmenting diastolic blood pressure [21].

Due to the dilation and contraction of the aortic wall over the cardiac cycle, the pressure wave moves at a finite, measurable speed. The pulsatile pressure measured somewhere far away from the heart will be delayed compared to the pressure wave measured proximal to the heart. As the aorta and other large arteries stiffen, the wave travels faster and less delay is measured. This effect can be quantified as the pulse wave velocity (PWV), an established method for assessing aortic stiffness *in vivo* [22]. PWV depends on aortic stiffness based on the relationship given by the Moens-Korteweg equation (Eq. 1.1), which states that wave speed in an elastic vessel depends on tangent modulus E, vessel thickness h, fluid density ρ, and vessel radius r [23].

$$PWV = \sqrt{\frac{Eh}{2\rho r}} \tag{1.1}$$

This quantity can be measured noninvasively in a patient by simultaneously measuring blood pressure at two locations in the arterial tree and measuring the time delay between the two pressure waves (**Fig. 1.2**). Wave speed is calculated by dividing the distance Δx between the pressure measurements by the time delay Δt between the feet of the pressure waves. The PWV measurement is typically qualified by which locations were chosen for the pressure measurements; carotid-femoral measurements (cf-PWV) are most representative of aortic stiffness since the measurements are taken just proximal and distal to the aorta, in contrast to ankle-brachial PWV, which includes a significant amount of arterial length in addition to the aorta [24]. With any *in vivo* measurements of PWV, the biggest uncertainty is the path length between the two pressure measurements [25]. Although the distance between the measurement sites can be measured on the surface of the patient, this technique does not account for the potentially tortuous path that the vessels follow between those sites. Normal values of cf-PWV increase with age, starting at 6.2 ± 0.8 m/s (mean ± SD) in people under 30 years and climbing to 10.9 ± 2.7 m/s in people over 70 years old [26].

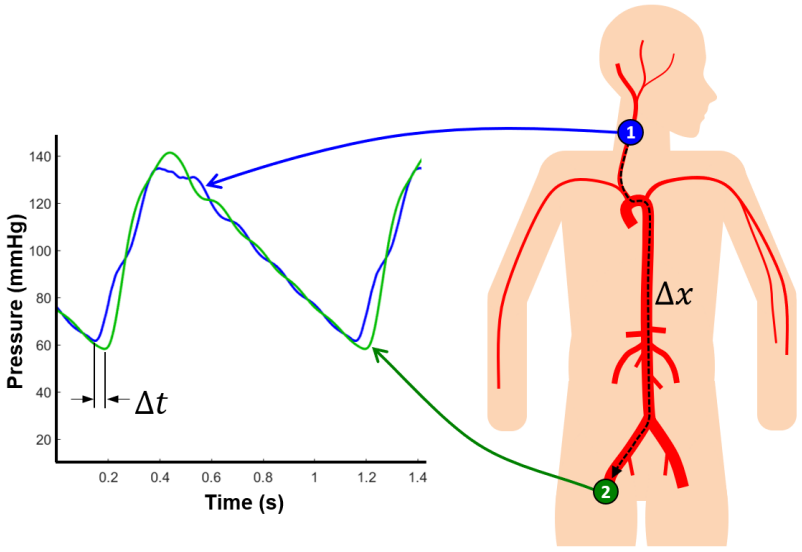


Figure 1.2: Diagram of carotid-femoral pulse wave velocity measurement in a patient. The key elements of PWV measurement are the distance Δx between pressure probes and the time delay Δt between the two pressure waves.

1.1.4 Blood Pressure

Figure 1.3 shows a representative blood pressure wave measured in the ascending aorta. The incisura is a dip that occurs after peak pressure when the aortic valve closes, marking the end of cardiac systole. Pulse pressure PP is the overall span of the pressure wave, calculated as the difference between SBP (P_2 in Fig. 1.3) and DBP. The value of ΔP, the difference between SBP and pressure at a preceding inflection point (P_1), increases with aortic stiffness and is usually zero for patients under 35 years old [27]. The jump in pressure from P_1 to P_2 occurs when the pulse wave reflects too early and augments systolic pressure. The Augmentation Index is often used to quantify the effect of wave reflection on systolic pressure and is defined as the ratio of ΔP to PP [24,27–29].

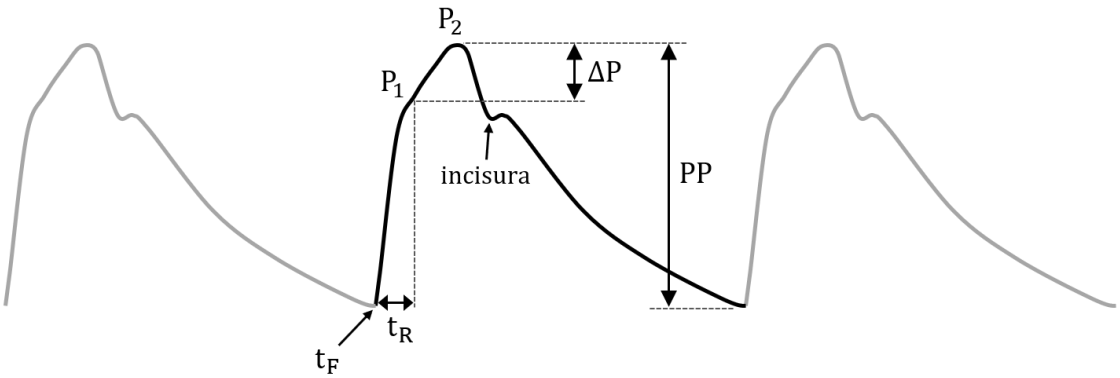


Figure 1.3: Pressure wave diagram. Pulse pressure (PP), augmented pressure (ΔP), reflection time (t_R), and time of the foot of the wave (t_F) are drawn on the figure.

1.2 Aortic Pathophysiology

1.2.1 Aortic Stiffness

The thoracic aorta increases in stiffness by about 40% from age 40 to 60 and continues to stiffen with aging [30]. When the aorta stiffens, it can no longer adequately expand to receive the systolic bolus of blood, and subsequently it does a poor job of pushing the blood downstream through contraction during diastole. Another consequence of the stiffer aorta is that the blood pressure wave travels faster (see Eq. 1.1), causing wave reflections to occur before the end of systole. Not only does the earlier reflection increase systolic pressure and afterload on the heart [30], but it also fails to augment the diastolic pressure wave, reducing perfusion through the coronary arteries [31]. Both the decreased capacitance and increased wave speed lead to higher systolic and pulse pressures in the cardiovascular system. The higher pressure has a detrimental positive feedback effect; the arteries, which are now experiencing increased loading, thicken and deposit extra collagen fibers to return to their target stress state. This process, however, results in further stiffening of the already stiffened vessels. Based on the changes discussed above that result from a stiffer aorta, it should not be surprising that several studies [32–35] now have shown that arterial stiffness on its own is a reliable predictor for risk of cardiovascular disease.

Stiffness of the aorta is dictated by both passive and active properties of the tissue. A vessel wall with higher collagen content is likely to dilate less at a given pressure than one with a higher proportion of elastin [36]. Active contraction of the smooth muscle cells in the vessel wall also influences the stiffness (and diameter) of the aorta [37,38]. Two driving factors behind smooth muscle tone and remodeling in the aorta are blood pressure and wall shear stress (WSS), stimuli that are sensed by the endothelial cells that line the vessel lumen. When the aorta is subjected to sustained high pressures, it thickens and dilates through deposition of additional material and growth of the smooth muscle cells [39]. The response to WSS is more complex, because both low and high WSS can have detrimental effects on aortic remodeling. Low WSS ($< 4\ \mathrm{dyn/cm^2}$), associated with areas of circulating or stagnant flow, is associated with wall thickening and formation of atherosclerotic lesions [40,41]. On the other hand, excessively high WSS ($> 400\ \mathrm{dyn/cm^2}$) is thought to lead to injury of the endothelial cells and subsequent platelet activation [41–43].

The main strategies for controlling and minimizing hypertension are lifestyle changes and medication. Because hypertension and arterial stiffness are closely related conditions, the recommended treatments are similar for both. Meneton et al. [44] wrote an extensive review of studies that demonstrated a link between daily salt intake and blood pressure. The effect of salt intake on arterial stiffness is not as well documented, but one study showed that reduced salt intake led to increased arterial distensibility, interpreted from reduced PWV, in normotensive subjects [45]. One theory behind this finding is that high sodium intake leads to an increase in smooth muscle tone, which adversely affects artery distensibility [46]. In another study, endothelium-derived nitric oxide, which normally acts as a vasodilator for arteries, was experimentally inhibited in normotensive patients and caused significant increase in PWV [47]. The authors of this study concluded that a natural reduction in nitric oxide with age may be a cause of arterial stiffening, and therapy including vasodilators may be effective in counteracting arterial stiffness.

While vasoconstriction is one treatable factor contributing to arterial stiffening, other age-related changes such as elastin fragmentation and collagen remodeling are also significant and not as simple to solve. Unlike collagen, which is constantly being produced and deposited in our vessels, elastin cannot be repaired or replaced when it inevitably becomes damaged from injury or aging [48]. More than any other component of the arterial wall, elastin is responsible for maintaining the elasticity that aids in propagating blood flow during diastole. Even if vasodilators and other treatments are used to reduce stiffness of the arteries, this will have limited value in restoring the elastic recoil that a large vessel like the aorta needs in order to perform its critical role as a capacitor for the cardiovascular system.

One treatment that aims to address the need for elastic recoil in arteries is called enhanced external counterpulsation (EEC) [31]. Pneumatic cuffs placed on the extremities apply pulsatile pressure to aid blood flow returning to the heart [49]. This system is recommended for patients with angina, whose circulation cannot adequately deliver oxygenated blood to the heart as a result of coronary artery disease or a similar condition. The external cuffs perform the contractile action that the stiffened arteries cannot, effectively restoring the diastolic pressure to an adequate state. This treatment is effective, though a one-time invasive intervention (e.g. stent, ablation, bypass) to solve the underlying problem is preferred for patients who can tolerate it [49].

1.2.2 Hypertension

Hypertension affects 32% of Americans, and another third of the population has prehypertension [50]. **Figure 1.4** shows the AHA guidelines for hypertension diagnosis, based on systolic (SBP) and diastolic (DBP) blood pressure measurements [51]. Hypertension is classified as Stage 1 or Stage 2, based on how high pressure is compared to healthy levels. Optimal blood pressure is SBP below 120 mmHg and DBP below 80 mmHg.

Medication is the primary intervention for hypertension, though lifestyle changes such as diet, exercise, and smoking cessation are also recommended. About 76% of people with hypertension

report using antihypertensive medications, but little over half of this group finds that their condition is well controlled [52]. Treatment for hypertension is almost exclusively limited to medication and lifestyle change, while treatment for complications of hypertension (aortic aneurysm, stroke, etc.) often involves risky surgical procedures. Due to the high mortality rate in CVD and related interventions, there is strong motivation to develop long-term, reliable treatment options for hypertension [53].

		SBP (mm Hg) →				
		<120	120–129	130–139	140–159	160+
← DBP (mm Hg)	<80	Normal	Elevated	Stage 1	Stage 2	Stage 2
	80–89	Stage 1	Stage 1	Stage 1	Stage 2	Stage 2
	90–99	Stage 2	Stage 2	Stage 2	Stage 2	Stage 2
	100+	Stage 2	Stage 2	Stage 2	Stage 2	Stage 2

Figure 1.4: Blood pressure levels and their associated hypertension diagnoses [51]

The overall prevalence of hypertension in 2017 was 32%, compared to 29.1% in 2012, which is consistent with the fact that prevalence is following an increasing trend. Incidence is higher in the elderly population, with 65% of people 60 years or older having hypertension compared to only 7.3% of people under age 40 [52]. As the body ages, the vascular system stiffens, which leads to higher pressures required to propel the same volume of blood [30,54–58]. Stiffening occurs due to factors such as decreased water presence and increased collagen deposition and crosslinking [59]. Particularly in large arteries such as the aorta, fragmentation and calcification of elastin lead to a loss in distensibility and elasticity, which are critical for healthy cardiovascular function [24,31,32,60].

1.2.3 Aortic Aneurysm and Dissection

The two main pathologies that can develop within the aorta are aneurysm and dissection, both of which threaten the vessel's ability to provide adequate blood flow to the body. Aneurysm is characterized by a ballooning of a segment of the aorta, which makes the vessel wall weak and prone to life-threatening rupture. Abdominal aortic aneurysm (AAA) is the most common form of the disease with a prevalence of over 1.4% in Americans over age 50 [61]. Thoracic aneurysm is less common with an incidence of about 13 per 100,000 people per year, though aneurysm of the ascending aorta is found in 40% of patients with bicuspid aortic valve [62,63]. For aneurysm at any position along the aorta, the primary concern is rupture of the vessel, which is a devastating event associated with a 30-day mortality rate of 50-70% for patients who make it to the hospital for intervention [62,64]. Depending on location, aneurysms are treated through open surgical repair or endovascular stent-graft placement.

Aortic dissection is characterized by one or more partial-thickness tears in the aortic wall that lead to development of a false lumen with blood flowing into the space between the layers of the vessel wall. The overall prevalence of dissection is estimated between 0.2-0.8% based on autopsy results [65]. Type of dissection is categorized by the location of the most proximal tear, with the first tear in the ascending aorta classified as Type A and first tear in the descending aorta as Type B (T_BAD). In 20-50% of patients, secondary flow in the false lumen interferes with blood perfusion to the rest of the body, weakens the aortic wall, and makes it susceptible to complete rupture. Whereas Type A dissection is always treated as a medical emergency, T_BAD can be classified as acute or chronic – a distinction that identifies whether the symptoms of dissection are progressing quickly or if the condition has stabilized [66]. Type A dissection comprises 70% of cases and requires immediate surgical intervention to replace the aorta due to high rate of rupture [67]. T_BAD, on the other hand, constitutes the remaining 30% of cases and follows a different treatment profile. Resection of the descending thoracic aorta is typically not recommended due to high risk of renal

damage or even paraplegia [67,68]. Instead, T_BAD is closely monitored, and the preferred treatment is for the patient to take antihypertensive medications to reduce the risk of rupture [67–70]. Recently, however, studies have shown evidence that stent-graft placement should be considered for patients with T_BAD to improve long-term outcomes, even if the dissection appears to be stable with medical therapy [71,72].

1.3 The Role of Stent-grafts in Aortic Disease

Endovascular aortic repair (EVAR) through placement of a stent-graft is increasingly becoming the intervention of choice for aneurysm and dissection in both the thoracic and abdominal regions [73,74]. Rather than removing the diseased segment of aorta and replacing it with an artificial graft during open surgery, EVAR facilitates minimally invasive placement of a wire-reinforced graft *within* the diseased aorta, creating a protective layer to shield the aneurysm sac or dissection tear from dynamic blood flow (**Fig. 1.5B**). By shielding the diseased tissue from blood flow, the stent-graft allows the aorta to remodel to shrink the aneurysm sac or false lumen and restore normal hemodynamics [75]. Several companies offer a range of stent-grafts for different regions of the aorta and different conditions, but they all follow the same design language of a stiff fabric tube attached to crimped metal rings that provide radial fixation force (**Fig. 1.5A**). The main differences among different products is the longitudinal flexibility of the device, diameter of deployment system, and shape-memory or balloon-expansion deployment mechanism [76].

EVAR has been used to treat AAA since 1990, and it has advanced such that it is associated with one-third the risk of perioperative mortality compared to open surgical repair [77,78]. Although EVAR had been developed several years earlier, it wasn't applied as an intervention for T_BAD until 1999 [79]. The stent-grafts, which were originally designed for treatment of aneurysms, consist of a metal wire mesh covered with a nonporous fabric. The metal stent provides the rigid structure necessary to maintain lumen patency, and the fabric isolates flow in the stented lumen from the occluded aneurysm sac. When used to treat dissection, the metal stent is placed against

the aorta wall, and the fabric acts as a barrier to prevent flow from entering the false lumen. The stent-graft must cover all entrance tears to the dissection, meaning that in some cases a patient may require a significant proportion of the aorta to be stented to fully block the tears.

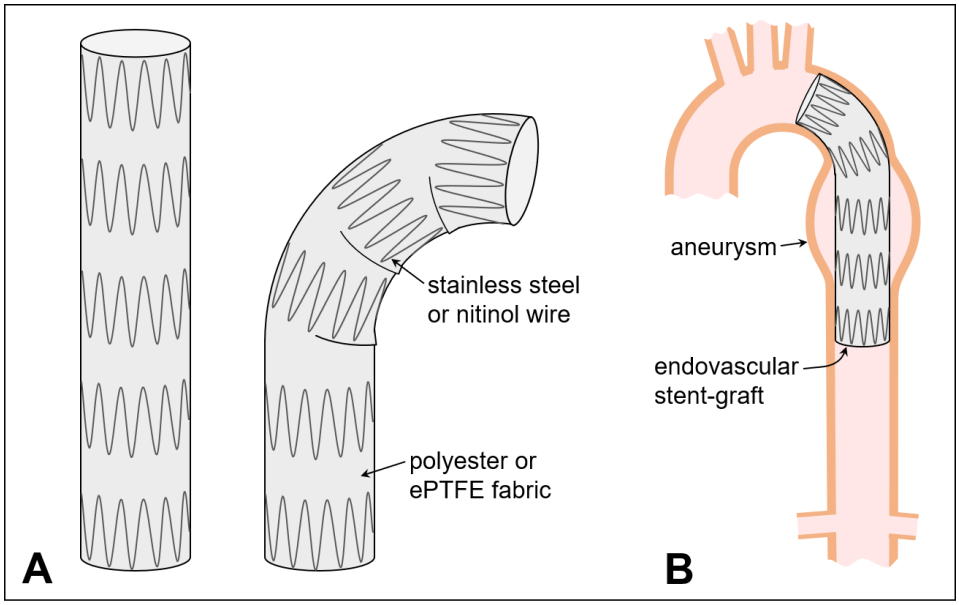


Figure 1.5: Stent-graft diagram. (A) Representative diagram of an aortic stent-graft consisting of a fabric tube and metal wire rings. (B) Example placement of a stent-graft in a descending thoracic aortic aneurysm.

The benefits of thoracic endovascular aortic repair (TEVAR) for T_BAD are often disputed, with the main arguments against the procedure being a relatively high occurrence of operative and post-operative complications. Major complications are reported in 11% of cases, most often including spinal injury, stroke, or retrograde Type A dissection [68,79,80]. In 40% of cases, placement of the stent-graft blocks the left subclavian artery [79], though a review showed that the effects of occluding this artery are usually limited to upper limb ischemia [81]. Survival rate after TEVAR for patients with chronic T_BAD is not significantly different from patients who are instead treated with medication and surveillance, though aortic-related deaths are reduced in TEVAR patients [68].

There has been a push in the industry to increase the number of devices available for TEVAR, including highly flexible branched or fenestrated stent-grafts that are designed for placement in the aortic arch [82–84]. The complex geometry and branching patterns of the ascending aorta and arch make it a challenging target for TEVAR, but increased availability of TEVAR for Type A dissection and ascending thoracic aortic aneurysm would increase access to early intervention and reduce overall mortality [85].

1.4 An Opportunity to Improve Aortic Interventions

In addition to the difficulty in deploying stent-grafts in the geometrically complex thoracic aorta, there is increased importance of stent-graft compliance for placement in the thoracic region. We know that compliance of the aorta is critical to maintenance of healthy blood pressure and cardiac afterload. As TEVAR procedures have become more prevalent, a growing number of studies have demonstrated that these stiff implants contribute significantly to increased arterial stiffness [86–88]. Although great strides are being made in the ability to perform the TEVAR procedure in a range of patients, very little attention is being paid to the consequences of increased aortic stiffness. The most obvious target for a more compliant stent-graft would be patients with T_BAD. TEVAR procedures for this condition are gaining popularity, and healthy compliance in the descending thoracic aorta is significantly higher than compliance in the abdominal aorta [30,71]. Still, a more compliant stent-graft stands to benefit any patient undergoing EVAR.

Because people with cardiovascular disease, including aortic dissection, often present with comorbidities, some level of risk will always be associated with interventions like TEVAR. Patients, however, should not have to settle for complications following TEVAR for T_BAD that arise specifically due to inappropriate design of the stent-graft. Current stent-grafts are designed as rigid tubes to meet the needs for aneurysm repair – maintain patency in a vessel after exclusion of an aneurysm sac [89]. But in the case of dissection, where 75% of patients have chronic hypertension [90], placing a rigid stent in the already-stiffened aorta is likely to worsen that condition.

Stent-graft induced new entry (SINE) is a major concern following TEVAR, in which placement of the stent-graft appears to cause a new (or newly lengthened) dissection. One of the most serious complications associated with TEVAR for T_BAD is retrograde Type A dissection. This condition constitutes the subset of SINE where the tear propagates backward toward the ascending thoracic aorta, creating an acute condition that requires immediate intervention. This complication carries a 33.6% mortality rate and has a higher incidence rate when TEVAR is treating dissection (4%) as opposed to aneurysm (0.9%) [68]. The higher risk associated with T_BAD can be attributed to the fragility of the aortic wall [68,89–96]. Because the dissected aorta is prone to tears, it is believed that stresses from manipulation, balloon dilation, and stent fixation during TEVAR are likely to cause damage. Risk is directly correlated with stent oversizing because higher radial forces from an oversized stent increase the likelihood of new or propagated tears in the brittle wall [68,90]. Several researchers have commented that for dissection repair, stent-grafts should impose substantially less radial force on the aorta since fixation occurs along the entire length of the stent, instead of only on the proximal and distal ends [89,90,95]. The same issue arises, if only briefly, when a balloon is inflated to expand the stent-graft into position. Additionally, prodding from thin, rigid wire such as the guidewire that leads the endovascular tools into the aorta, or the barbed ends of the stent used for fixation, pose a substantial threat to the dissected aorta, in contrast to the healthier tissue surrounding an aneurysm.

A less severe but more common complication arises when SINE occurs distal to the stented section of the aorta. One study of 108 patients who underwent TEVAR for T_BAD reported distal re-entry tear in 26.6% of patients, sometimes undetected until years after the TEVAR procedure [90]. Distal SINE was controlled in more than 40% of patients with medical therapy aimed at maintaining blood pressure below levels that may lead to rupture of the dissection. In the remaining patients, another TEVAR or open repair was performed due to symptoms such as malperfusion or consistent growth in aorta diameter.

Another issue with TEVAR for T_BAD is that it inherently exacerbates the hypertensive condition that most patients have prior to treatment. Placement of a rigid stent-graft blocks expansion and contraction of the aorta in that segment, reducing the capacitance and increasing the stiffness of the entire aorta. If the stent-graft worsens hypertension, then there is a strong chance of cardiovascular disease progression, including re-dissection, even without direct injury to the aorta during the TEVAR procedure [89].

1.5 Research Aims & Outcomes

The goal of my work was to design a new aortic stent-graft that improved upon currently available devices by increasing device compliance without compromising its protective function. The key research studies that contributed toward realization of this goal are described in the following four chapters of this thesis. A brief summary of each chapter is given below.

Chapter 2: Parameters that Impact Aortic Stiffness and Blood Pressure. The first step toward developing an improved stent-graft was to study the effects of different aortic parameters on the effective stiffness of the arterial system and, subsequently, blood pressure. A modified Windkessel model was developed to sweep over a range of resistance and capacitance (compliance) parameters in the descending thoracic region of the aorta. The information gathered from this study informed the design concept that was pursued for the remainder of the thesis.

Chapter 3: Double-Walled Stent-Graft: Proof of Concept. This chapter introduces the double-walled stent-graft (DWSG) concept, which leverages the compressibility of a biocompatible gas to incorporate capacitance within the lumen of a standard stent-graft. Preliminary prototypes of the DWSG were subjected to static inflation experiments to characterize capacitance and resistance, and the dynamic behavior was compared to these static measurements through pulsatile flow loop experiments. The parameters estimated from these experiments were input into the modified

Windkessel model from Chapter 2 and used to predict behavior of the DWSG under physiologic conditions.

Chapter 4: Effect of the Double-Walled Stent-Graft on Pulse Wave Velocity. A fluid-structure interaction (FSI) computational model was developed to assess the impact of the DWSG on aortic stiffness. Pulse wave velocity was calculated through measurement of the time delay between pressure waves upstream and downstream of the DWSG. The gas layer of the DWSG was modeled as a highly compressible solid material with coefficients that matched pressure-volume behavior of the true gas layer. The same measurements were conducted in an experimental flow loop, using an endovascular prototype of the DWSG fabricated with plastic tubing and a sheet of bubble wrap.

Chapter 5: Shape Optimization of the Double-Walled Stent-Graft Gas Layer. A multiobjective optimization study was performed to find a tradeoff between maximizing capacitance of the DWSG and minimizing its adverse effects on hemodynamics. Two version of the optimization were conducted – one to identify the optimal longitudinal profile for the gas layer and another to find the optimal number of circumferential segments into which to divide the gas layer.

Chapter 2

Parameters that Impact Aortic Stiffness and Blood Pressure

Portions of the work in this chapter were previously published in proceedings for the *2018 Design of Medical Devices Conference* [97].

2.1 Introduction

In 2017, the American Heart Association reported that one third of deaths in the United States, and 31% of deaths worldwide, are attributed to cardiovascular disease (CVD) [98]. A risk factor pervasive across most types of CVD is chronic high blood pressure, or hypertension [53]. Hypertension affects 32% of Americans and is more prevalent in the elderly population [99]. Primary treatment consists of lifestyle changes (e.g. diet, exercise, smoking cessation) and antihypertensive medication, but only half of patients taking medication find that their condition is well controlled [98]. When treatment for hypertension is ineffective, patients are at risk for developing CVD. Treatment for CVD depends on disease severity and presentation but often includes risky and invasive procedures to reinforce vessels or reroute blood flow.

Endovascular procedures are favorable for CVD treatment because they are minimally invasive, but a substantial risk is often overlooked when it comes to thoracic endovascular aortic repair (TEVAR). The aorta is the largest artery in the human body, and it is the main conduit for delivering oxygenated blood to most organs and peripheral vessels. However, in addition to providing a low-resistance route for blood, the aorta is responsible for regulating downstream flow rate. Its elastic nature allows it to expand to absorb the bolus of blood leaving the heart's left ventricle during cardiac systole and then contract to push that blood along during diastole [100].

This capacitive function is inhibited when the aorta wall stiffens, either naturally with age or due to placement of a rigid stent-graft (SG) during TEVAR. Aortic stiffening on its own is a predictor of CVD risk [32–35] in addition to its contribution to increased blood pressure. It is troubling that TEVAR, while treating CVD, is also augmenting one of the most significant CVD risk factors.

Aortic dissection is one of the main aortic diseases for which TEVAR is employed. Dissection occurs when the aorta wall tears, often forming a false lumen within layers of the wall. This condition can cause poor perfusion to vital organs and risk of fatal rupture of the aorta. Dissections that occur in the descending thoracic aorta are commonly treated with TEVAR to reinforce the torn wall and maintain vessel patency. However, likely due to ongoing high blood pressure, about 30% of patients who undergo stent-graft repair of descending thoracic aortic dissection develop another tear within months or years after the procedure [68,90]. Growing evidence suggests that the high stiffness of the implanted stent-graft may contribute to persistent hypertension and poor long-term outcomes in these patients [101].

This contradiction in treatment – delivering a stiff stent-graft to a patient whose underlying disease was caused by a stiff aorta – illuminates the need for a stent-graft that preserves, or even reduces, blood pressure. The first steps in developing this stent-graft are to quantify the effect of stent-graft placement on blood pressure in the hypertensive patient and to investigate whether a stent-graft with particular properties has potential to therapeutically reduce hypertension. In this study, the properties of a simulated stent-graft in the descending thoracic aorta are tested for effect on blood pressure using a lumped parameter model of the arterial system.

2.2 Methods

2.2.1 Modified Windkessel Model

Researchers often use a circuit analog model to describe the relationship between pressure and flow in the arterial system [102]. The essence of this model is to consider the aorta as a capacitor C in parallel with the resistance of the peripheral vessels, R_P. The most common version of the

model also includes an impedance term Z_c, in series with the two parallel elements, to account for input impedance of the aorta. Though Z_c is a function of input flow frequency, it is often approximated as a constant resistance R_c for simplicity [103]. The four-element Windkessel model places an inductor in parallel with the impedance to represent the inertia of the flowing blood [102,104,105].

We developed a lumped parameter model, built upon the four-element Windkessel [105], to simulate the arterial system with a stent-graft placed in the descending thoracic aorta (**Fig. 2.1A**). In our model, three capacitor-resistor sets represent the ascending (1), descending (2), and abdominal (3) aortic segments (**Fig. 2.1B**). Parameters R_c and L_c represent the characteristic impedance of the heart outlet and entrance to the most proximal ascending aorta [105]. R_P is the lumped resistance of the peripheral vasculature.

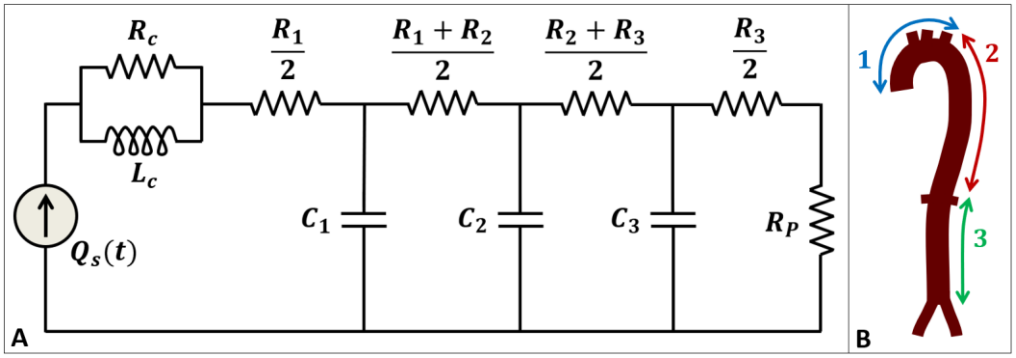


Figure 2.1: Modified Windkessel model. (**A**) Four-element Windkessel model with capacitance and resistance of the aorta divided into three segments as shown in B. Flow rate Q is imposed; resistance (R), capacitance (C), and inductance (L) elements represent the impedance of the arterial system. (**B**) Diagram of the aorta with labels for: 1 – ascending aorta/arch, 2 – descending aorta, and 3 – abdominal aorta.

2.2.2 Sweep of Model Parameters

The capacitance of each segment was computed using its fractional contribution to the total system capacitance taken from Saouti et al. [106], who recorded pulse wave velocity measurements at various locations along the aorta to approximate the regional stiffness of the aorta and its branches. The percentage of the overall capacitance attributed to each region is given in **Table 2.1**.

Note that the aorta itself accounts for only 65% of system capacitance [106], but the remaining capacitance from proximal and distal branches is lumped respectively into segments 1 and 3 in this model. A relationship for capacitance can be derived from the Law of Laplace (Eq. 2.1) depending on vessel stiffness E, wall thickness h, radius r, length L, and Poisson's ratio ν, however it was not practical to find suitable values for regional stiffness of the pressurized aorta; most measurements of tissue stiffness in literature are evaluated *ex vivo*, and the lack of prestretch in these samples causes the effective stiffness *in vivo* to be underestimated.

$$C = \frac{\left(1 - \frac{\nu}{2}\right)\pi r^3 L}{Eh} \tag{2.1}$$

For the three aortic segments, resistance R_i was calculated using the Poiseuille pressure-flow relationship (Eqn. 2.2). Resistance for a given segment is split evenly between upstream and downstream from the capacitance C_i, similar to the T element used in multicompartment lumped parameter arterial models [107].

$$R = \frac{8\eta L}{\pi r^4} \tag{2.2}$$

Blood dynamic viscosity η was held constant at 3.5 cP for all calculations, while nominal vessel length L and radius r for the respective aortic segments were set to measured values from literature [57]. Two sets of parameters were calculated to develop one model of a young, normotensive patient and one of an older, hypertensive patient.

Table 2.1: Breakdown of aortic capacitance. Contribution of each modified Windkessel model (**Fig. 2.1A**) to total system capacitance, calculated using data from Saouti et al. [106]

Segment number and description	Capacitance (%)
1 – ascending thoracic aorta, aortic arch, arch branches	31.6
2 – descending thoracic aorta	25.5
3 – abdominal aorta, abdominal branches, pelvic/leg arteries	44.9

2.2.3 Study Design

Two baseline cases – normotensive and hypertensive – were run with the nominal values for all parameters. Next, to simulate different stent-graft properties, a sweep was conducted for the values of R_2 and C_2. The resulting pressures for each set of parameters were measured and recorded. Systolic blood pressure (SBP) was taken as the peak value in the steady state pressure waveform and diastolic blood pressure (DBP) as the minimum value. Pulse pressure (PP) and mean arterial pressure (MAP) were calculated using the measured SBP and DBP, as shown in Equations 2.3 and 2.4.

$$PP = SBP - DBP \tag{2.3}$$

$$MAP = {}^{1}/_{3}\,SBP + {}^{2}/_{3}\,DBP \tag{2.4}$$

The imposed flow rates for the normotensive and hypertensive models both were derived from the profile reported by Kind et al. [108], but the pulse rate and stroke volume were modified to reflect values reported in literature for young and elderly patients [9,109]. The timeseries flow profiles were generated with a MATLAB script that scaled the period of the Kind et al. wave to match the desired pulse rate and then scaled the wave amplitude until the integrated area under each curve matched the specified stroke volume. The profiles were stored as paired time and flow rate vectors with a time increment of 0.001 seconds.

The modified Windkessel model was solved in the frequency domain using Fourier series expansion and complex impedance analysis. The flow profile was deconstructed into its first 200 harmonics, where each frequency is a multiple of the fundamental frequency ω_0. An expression for the complex impedance of the circuit shown in **Fig. 2.1A** was derived (Eq. 2.5) and evaluated for the n-th harmonic $\omega = n\omega_0$, where j is the imaginary unit. After the pressure response for each was calculated independently, all of the separate contributions were added together to give the final result.

$$Z(\omega) = \left(\frac{1}{R_c} + \frac{1}{j\omega L}\right)^{-1} + \frac{R_1}{2} + \left[j\omega C_1 + \frac{1}{\left(\frac{R_1 + R_2}{2} + Z_\beta\right)}\right]^{-1} \tag{2.5}$$

$$Z_\beta = \left\{j\omega C_2 + \left[\frac{R_2 + R_3}{2} + \left(j\omega C_3 + \frac{1}{\frac{R_3}{2} + R_P}\right)^{-1}\right]^{-1}\right\}^{-1} \tag{2.6}$$

Each model was evaluated for 90 simulated seconds to ensure that steady state was reached, and results were extracted from the final five cardiac cycles. Pressure measurements were obtained over parameter ranges of $0 \leq C_2 \leq 1$ mL/mmHg and $10^{-10} \leq R_2 \leq 0.1$ mmHg $\cdot$ s/mL in both the normotensive and hypertensive models.

2.3 Results & Discussion

2.3.1 Effects of Resistance and Capacitance on Blood Pressure

The results of the sweeps for the normotensive (**Fig. 2.2A-B**) and hypertensive (**Fig. 2.2C-D**) models followed the same trends but over different pressure ranges. The unstented normotensive model had a baseline blood pressure of 118/72 mmHg (systolic/diastolic), while baseline pressure in the hypertensive model was 150/99 mmHg. Increasing capacitance (C_2) led to decreases in both systolic and pulse pressures. Increasing descending thoracic aorta resistance (R_2) had minimal effect on pressure until its value was within two orders of magnitude of R_p; as R_2 increased past this threshold, pressure increased sharply. In this high resistance range, pressure became much less sensitive to changes in capacitance.

When a standard stent-graft (SG) is placed in the descending thoracic aorta, it has negligible effect on resistance due to its low profile, but it has a significant impact on capacitance in that region. The materials used for the graft portion of a SG are more than 20 times stiffer than the healthy aortic wall [110], causing capacitance in the stented region to drop to 4% of its unstented value. **Figure 2.3** shows the effect of SG placement on the pressure profile in both the normotensive (**Fig. 2.3A**) and hypertensive (**Fig. 2.3B**) models. For the normotensive patient, blood pressure

shifts from 118/72 to 125/66 mmHg, corresponding to a 6% increase in SBP, an 8% decrease in DBP, and a 29% increase in PP. For the hypertensive patient, pressure changes from 150/99 to 157/92, corresponding to a 5% increase in SBP, a 7% decrease in DBP, and a resulting 29% increase in PP. Although relative changes in pressure for both models were approximately the same, the absolute change in pressures was slightly higher for the hypertensive patient since its baseline values were higher than those of the normotensive patient.

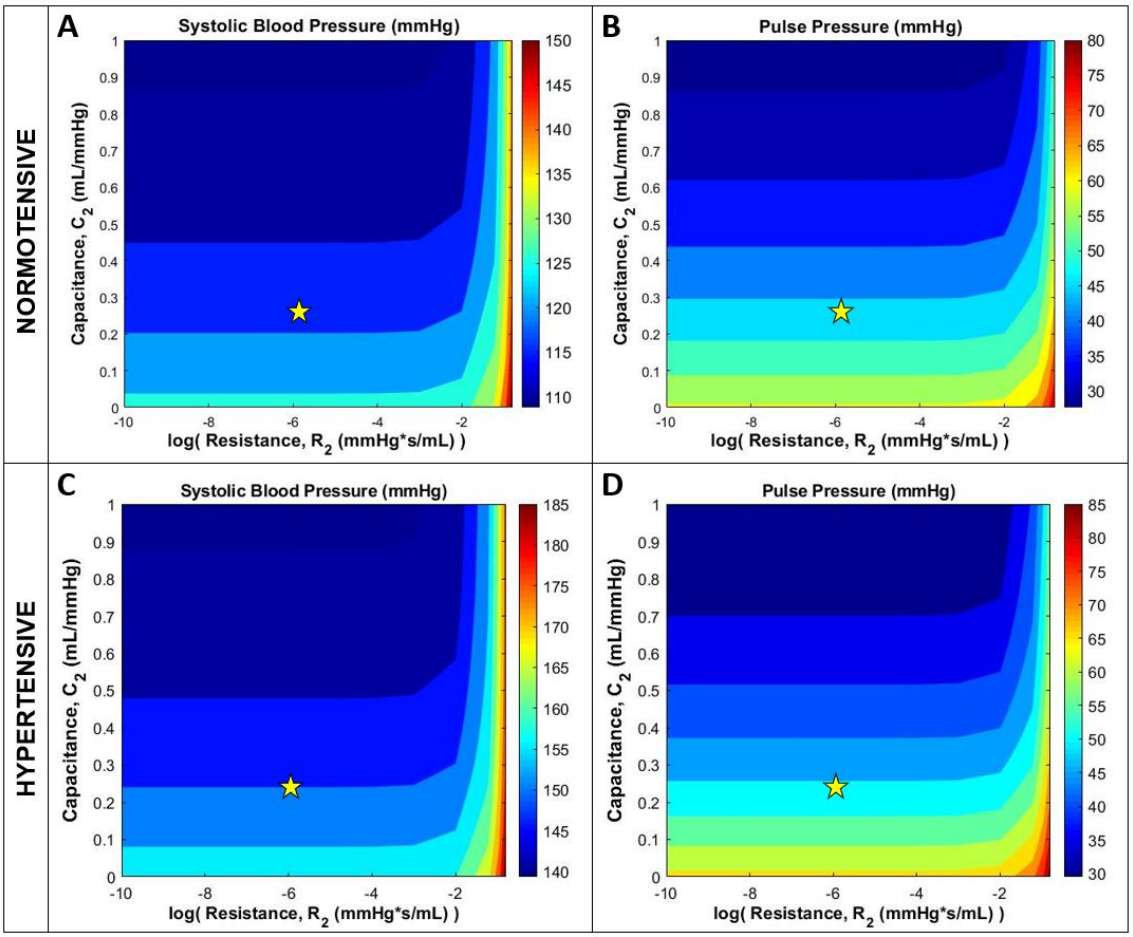


Figure 2.2: Results of Windkessel parameter sweep. (A) Systolic and (B) pulse pressure in the normotensive model over the range of R_2 and C_2 values. (C) Systolic and (D) pulse pressure in the hypertensive model. In all panels, the star signifies the original model parameters, representing an unstented condition. Note that the color bar range is different in each panel and resistance is on a logarithmic scale.

One important result from this study was the fact that no value of C_2 (within reason) in the hypertensive model was able to lower SBP to the baseline normotensive pressure. Even if the baseline hypertensive C_2 was quadrupled, SBP remained 18% higher than the baseline normotensive pressure. This result suggests that even a high-capacitance SG cannot be expected to completely reverse the hypertensive condition caused by low systemwide capacitance. Despite this limitation, there is still significant value in a SG that lowers blood pressure or at least minimizes the increase in pressure typically caused by existing devices. In a review paper that analyzed how reducing blood pressure affected risk of CVD across over 100 randomized trials, it was estimated that a linear relationship exists between reduction in SBP and reduction in major CVD events [111]. We have shown that placement of a rigid stent-graft increased SBP by 7 mmHg in both of our models. According to the findings of the review paper, a new stent-graft design that maintains capacitance at unstented values could reduce risk of CVD by about 10% compared to patients who receive a standard stent-graft.

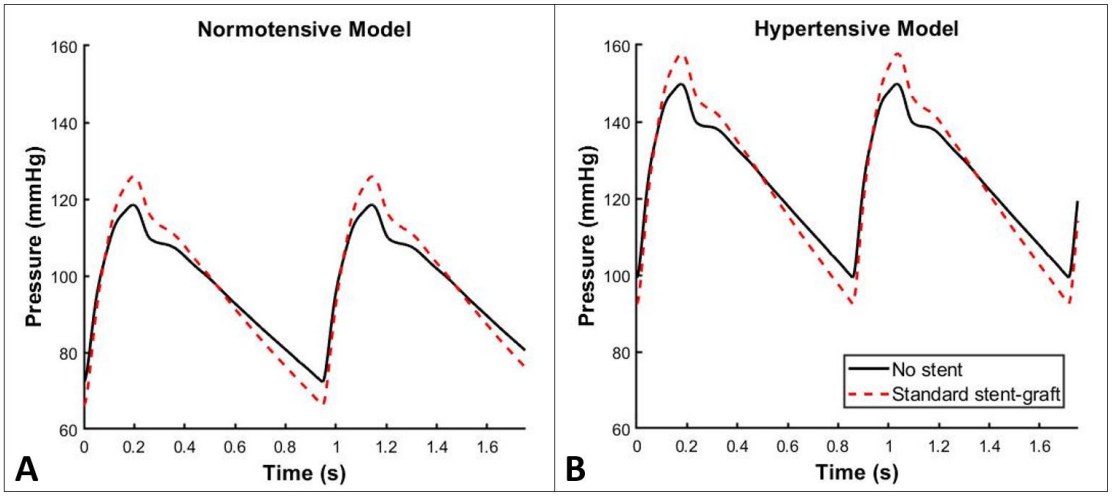


Figure 2.3: Effect of a standard stent-graft on blood pressure. Pressure profiles for the (A) normotensive and (B) hypertensive Windkessel models, with and without a stent-graft placed. Note that the axis ranges for both plots are the same, and the legend in panel B applies to the plots in both panels.

2.3.2 The Physical Tradeoffs between Resistance and Capacitance

Although resistance and capacitance can be independently selected in the context of this model, they are inherently linked by the physical parameters that define them. For example, if vessel radius is increased, capacitance increases due to the relationship $C \sim r^3$ (Eq. 2.1), and resistance decreases from the relationship $R \sim r^{-4}$ (Eq. 2.2). On the other hand, if vessel length is increased, capacitance again increases but resistance increases as well. In order to change capacitance without affecting resistance, only the vessel stiffness, Poisson's ratio, and thickness – all parameters that affect distensibility of the vessel – could be changed. To change resistance without affecting capacitance, blood viscosity would have to be changed.

If my objective is to design a new aortic stent-graft (SG) that has increased capacitance to lower blood pressure, then I must identify a set of parameters that improve device capacitance without negating the core protective function of the stent-graft. For a SG to be deployed endovascularly, it must be designed to sit within the lumen of the aorta; this requirement restricts the radius of the device from exceeding that of the native aorta. It can be slightly oversized to push radially outward on the aorta and increase the vessel radius, but excessive SG oversizing is known to increase risk of re-tears in patients treated for thoracic aortic dissection [90,112]. Another challenge is that the aorta is not cut during endovascular surgery, so there is minimal opportunity to add length beyond that of the segment to be stented. The length of aorta to cover with a SG can be adjusted to some degree, but increasing stented length also leads to increased occlusion of branching vessels and risk of paraplegia [113,114].

Stiffness of the SG is a viable parameter to decrease in order to increase capacitance, but it is not without limitations. At best, the effective stiffness of the endovascular SG could be as low as the stiffness of the native aorta. If the stiffness of the SG were decreased below that level, any potential dilation of the device would be prevented by the stiffer aortic wall surrounding it. Another issue with decreasing SG stiffness to increase capacitance is that the decreased stiffness would

diminish the protective function of the device. By having a significantly higher stiffness than the surrounding aortic wall, the SG is able to shield the vulnerable tissue from pressure-induced cyclic loading.

All of the previously presented options for lowering capacitance have assumed that the SG follows the same equations as an elastic vessel for resistance (Eq. 2.2) and capacitance (Eq. 2.1). It is possible, however, to create a different type of SG that is not simply an elastic tube and therefore follows a different set of equations. The more general definition for capacitance is given by Eq. 2.3, which states that capacitance describes how much volume change dV_{lumen} the vessel lumen undergoes for a given change in lumenal pressure dP_{lumen}.

$$C = \frac{dV_{lumen}}{dP_{lumen}} \tag{2.3}$$

Instead of relying on dilation of the SG wall to achieve change in volume, an external reservoir could be attached to the vessel wall, allowing blood to exit and return from the lumen over the cardiac cycle. This concept was implemented with the ROX coupler device, which utilized the venous system as an external reservoir by creating a pathway for blood to flow between the external iliac artery and vein [115]. This device often results in adverse effects on the iliac vein and suffers from failure due to occlusion after years of vascular remodeling [116–118].

Another way to change lumen volume is by incorporating a compressible material into the SG. When pressure is high during systole, the compressible material would reduce in volume, and then when pressure reduces during diastole it would expand again to full volume. Through this loading and unloading, the volume of the lumen would change to deliver capacitance without requiring the vessel wall to deform and without requiring connections to any external reservoirs. Although adding material within the vessel lumen would reduce the flow area and increase resistance, we saw in **Fig. 2.2** that resistance can increase by several orders of magnitude from the unstented value before it has any measurable impact on pressure. Incorporation of a compressible

material within the vessel lumen takes advantage of this insensitivity to resistance by trading flow area for capacitance. This concept is the basis of the double-walled stent-graft (DWSG), which is the primary topic of this thesis. The details of the idea will be discussed further in the following chapters.

Chapter 3

Double-Walled Stent-Graft: Proof of Concept

The content of this chapter was previously published as a research article in the *ASME Journal of Medical Devices* by Kizilski, Amili, Coletti, Faizer, and Barocas [119].

3.1 Introduction

Chronic high blood pressure, or hypertension, affects about one third of the adult US population [98]. Multiple studies have shown a strong link between hypertension and more serious cardiovascular diseases including stroke and ischemic heart disease [98,120–122]. Although a variety of factors may contribute to the development of hypertension, the present work focuses on the role of aortic stiffening.

The aorta, the largest artery in the human body, plays an essential role in conducting oxygenated blood from the heart to the visceral organs and major branching vessels. When an injury develops in the aorta, either due to trauma or a chronic condition, primary intervention focuses on preventing vessel rupture and maintaining adequate blood flow. The most common types of aortic implants are grafts and stent-grafts [123,124]. Aortic grafts are flexible fabric tubes that are sewn end-to-end with the native aorta to replace a damaged portion that has been excised. Stent-grafts, which are fabric tubes reinforced with metal wires, are delivered via an endovascular catheter and deployed to push against the internal wall of the damaged aortic segment. Rather than completely replacing a length of the aorta, a stent-graft resides within the native vessel and provides structural support to prevent occlusion or rupture. Stent-graft procedures have been gaining popularity over open surgery in recent years due to reduced morbidity and mortality [125].

Aside from its role as a conduit, the aorta plays a crucial role as a reservoir in the arterial system. The elasticity of a healthy aorta allows it to expand and contract with each heartbeat, storing and releasing blood during cardiac systole and diastole, respectively. By temporarily storing blood, the aorta promotes a steadier flow to the peripheral vessels, thereby reducing the swing between systolic and diastolic pressures, also known as the pulse pressure. Increased aortic stiffness, which occurs naturally with age, has been identified as an independent risk factor for cardiovascular events [126]. It has also been shown that increased arterial stiffness is associated with increased blood pressure, due to increased wave speed and pulsatility [127].

The capacitive function of the aorta has long been recognized and quantified by both the scientific and medical communities, yet it has been largely neglected in existing graft and stent-graft designs. Dacron (polyethylene terephthalate) and other materials commonly used for graft fabric are more than 20 times stiffer than the healthy aortic wall [110]. The radial stiffness of a stent-graft ensures that it protects the damaged aortic wall from pressure-induced injury or rupture, but it also inhibits storage and release of blood in that segment. With more studies emerging about the long-term health effects of stent-grafts, it is becoming apparent that matching aortic conductance alone is an insufficient standard [89].

Incorporating both protection of the aortic wall and significant fluid capacitance into a single stent-graft design is not a trivial task – protection requires that the aorta is not subjected to large oscillatory strains, but capacitance requires that the lumen volume changes with blood pressure. Another difficulty arises when we consider the fact that many patients receiving stent-grafts already have a significantly stiffened aorta, which cannot provide the capacitance seen in a healthy individual [24,128]. Approximately 40% of patients receiving stent-grafts to treat dissection in the descending thoracic aorta are over 65 years of age [129], at which point the aorta is more than twice as stiff as that of a young, healthy individual [130]. The optimal stent-graft would shield the aorta

from stresses due to blood pressure *and* still would permit changes in lumen volume in response to pressure changes, even if the aortic wall itself cannot adequately stretch and recoil.

Efforts to develop a more compliant stent-graft to better mimic the capacitive function of the healthy aorta are limited by the extrinsic constraints of the existing diseased aorta. First, if the device is in direct contact with the aortic wall along its entire length, as is usually the case in the treatment of aortic dissection, the overall compliance and capacitive characteristics of that aortic segment are *at best* defined by the diseased, native aortic wall, regardless of the graft material used. Simply put, the stent-graft cannot make the native aortic wall (with which it is in contact) *more* compliant, only less. In practice, all existing stent-grafts have been demonstrated to add significantly to aortic rigidity [131]. Furthermore, if the stent-graft is not in direct contact with the aortic wall except for fixation at its two ends, as may be the case with an aortic aneurysm, or where a stent-graft is theoretically designed to be narrower in its central section to prevent direct wall apposition with the native aorta, the intervening space will be filled with blood. If the stent-graft works as intended, this blood will not flow and will clot, forming a chronic thrombus, which is virtually incompressible [132], again removing any capacitive potential. The clinical scenario in which thrombus formation does not occur – so the space between the stent-graft and the aortic wall contains flowing blood – is considered a clinical failure termed endoleak, as it exposes the damaged aortic wall to ongoing pressurization and risk of rupture [133].

In this work, we present a novel, double-walled stent-graft (DWSG) design which aims to address the issue of aortic capacitance loss [134]. By introducing a permanent, compressible gas interface between the aortic wall and an inner compliant lumen, we intend to introduce a capacitive chamber that better resembles healthy aortic function. An early prototype of the design was evaluated through pressure measurements in static and pulsatile flow experiments. The results of these experiments were used to develop more accurate computational models of the design and to facilitate more thorough parameter optimization.

3.2 Device Design

Figure 3.1 outlines the inputs and outputs to the models and experiments that were used to characterize the DWSG and its predicted effect on cardiovascular health. Details of the DWSG design, experimental methods, and computational models are described in the following sections.

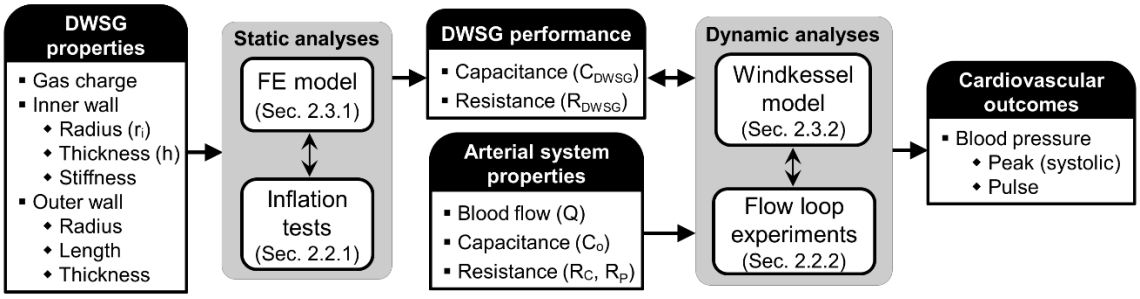


Figure 3.1: Proof-of-concept study flowchart. Flowchart depicting the procedure followed to characterize the DWSG and predict its performance. The sections of this paper that describe each method are denoted, when applicable.

3.2.1 Design Concept

The long-term objective of this investigation is to develop a new stent-graft design capable of maintaining or lowering blood pressure in patients requiring aortic repair. An implant designed to help control blood pressure could reduce patient dependence on antihypertensive medications and lower risk for subsequent cardiovascular events. The goal of the proposed design is to counteract high blood pressure by partially restoring fluid capacitance lost due to vascular stiffening and stent-graft rigidity. One key requirement for the design is that it be an endovascular device, which would reside within the lumen of the native aorta. Based on this constraint, it is necessary that the capacitive function operate within a completely rigid aortic wall. To this end, we needed to investigate whether the aorta could tolerate some reduction in lumenal area, if the reduced area facilitated increased capacitance. Compared to the rest of the arterial system, the aorta has negligible flow resistance; if the lumen were reduced in diameter by a small percentage, we hypothesize that this area could be used to incorporate capacitance without introducing significant flow resistance.

Fluid capacitance C is defined as the derivative of fluid volume stored in the lumen, V_{lumen}, with respect to lumen pressure, P_{lumen} (Eq. 3.1) [135].

$$C = \frac{dV_{lumen}}{dP_{lumen}} \tag{3.1}$$

If we assume the stent-graft will occupy a fixed length of the aorta, then the only way to vary the stored volume of fluid within that fixed length is to vary the lumen radius. Assuming a fixed outer wall, corresponding to the nearly rigid native aorta, or the rigid stent-graft that protects the injured aorta from cyclic loading, variable lumen radius can only be achieved by a compressible layer *within* the stent-graft.

We propose a double-walled stent-graft (DWSG) design, which incorporates a compressible layer of carbon dioxide (CO_2) gas between a stiff outer wall and a flexible, elastic inner wall (**Fig. 3.2A**). The outer wall, like existing stent-grafts, holds the device in place and protects the diseased aortic wall from pressure-induced injury. The inner wall passively transmits the lumenal pressure to the contained gas, which consequently compresses during systole and expands during diastole. According to the Ideal Gas Law, a gas subjected to normal blood pressure levels (120/80 mmHg) should experience a roughly 5% volume change between systole and diastole (40 mmHg change in pressure versus approximately 860 mmHg absolute pressure); because the DWSG is targeted at patients with high blood pressure, a 5% volume change is a conservative estimate.

The rationale for including a layer of CO_2 gas within the device is that there must be some compressible material separating the two walls in order for the device to have capacitive behavior. If a liquid were used instead, then the inner elastic wall would not be able to expand due to the incompressible nature of liquid. If all material were evacuated from that space, a vacuum would form, causing the elastic wall to get pressed directly against the stiff, outer wall. Filling the space with a compressible gas is the most practical way to achieve local capacitance. Specifically, CO_2

was chosen due to its ability to absorb safely into the bloodstream [136]. Any other biocompatible gas would be an adequate substitute.

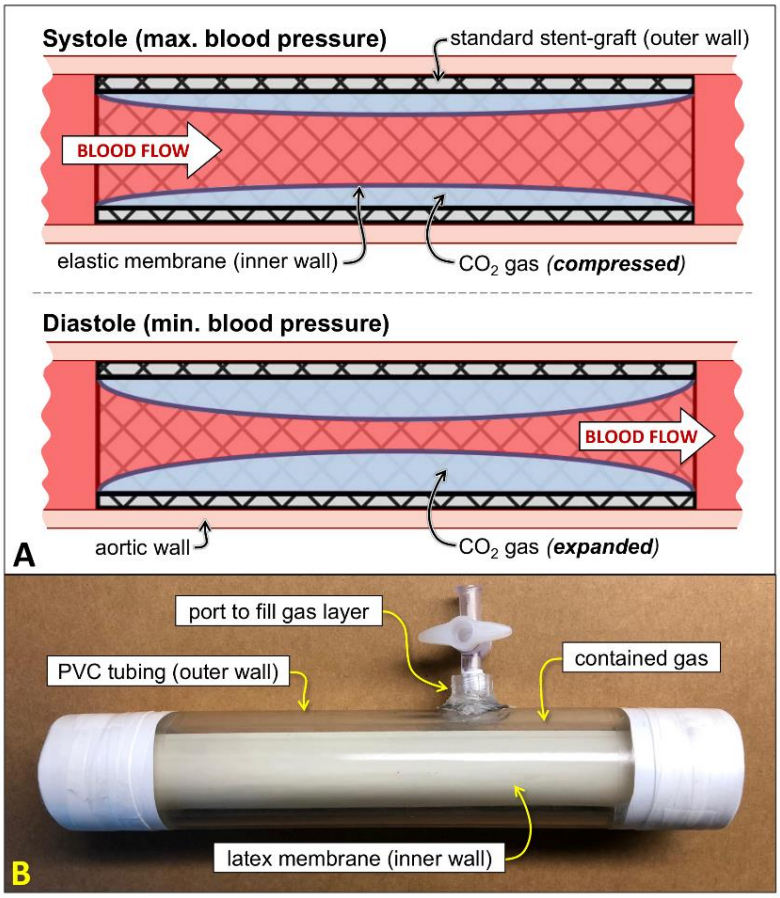


Figure 3.2: Double-walled stent-graft (DWSG) preliminary prototype. (A) Diagram of the DWSG design, with a stiff outer wall pushing radially outward against the aortic wall and a flexible inner wall containing a gas layer. (B) Photo of the DWSG prototype (15 cm length) used for the static and dynamic experiments. Latex tubes with different diameters and prestretches were used to achieve a range of inner wall properties.

The primary variables of interest in the DWSG design are the amount of gas contained, the overall length of the device, and properties of the inner wall, including stiffness, thickness, and unloaded diameter. The properties of the outer wall are not critical to device function because this wall only serves as an anchor for the device, holding it fixed against the stiff aortic wall. As explained earlier, any compliance in the outer wall of the DWSG is overridden by the stiffness of

the aorta. In this study, the outer wall properties and the overall length of the device were kept constant, and the effects of the amount of gas and inner wall properties were evaluated.

3.2.2 Initial Prototypes

Prototypes of the DWSG (**Fig. 3.2B**) were built using stiff 2.54 cm (1") diameter PVC tubing for the outer wall and a thin latex tube (Penrose drain) with a diameter of 1.9 cm (3/4"), 2.22 cm (7/8"), or 2.54 cm (1"), for the inner wall. In addition to being inexpensive and readily available, PVC is nearly rigid under the loading conditions considered; thus, it represents the worst-case scenario in which the surrounding vessel wall and/or stent-graft wall offer no compliance, and all flow capacitance must come from compression of the gas layer. Devices were assembled by threading the latex tube through the lumen of the PVC tube and stretching either end of the latex tube around the outside of the PVC, creating a sealed space between the two layers. Prototypes were built with the latex tube prestretched to 5% and 50% to artificially create inner walls with different stiffnesses. The ends of the latex tube were anchored using PTFE tape and a layer of Parafilm (Sigma-Aldrich, Merck KGaA, Darmstadt, Germany) to secure the tape. A port in the wall of the PVC tube was connected to an external luer lock valve, which was used to add or remove gas from the space between the two tubes. Although CO_2 would be the preferred gas in an *in vivo* device, tests were conducted using atmospheric air due to its similar mechanical behavior and ample availability.

3.3 Experimental Methods

Prototypes of the DWSG were tested in static inflation and in dynamic flow loop experiments. Through static inflation, the capacitance was measured and compared among different DWSG configurations, while changes in dynamic system pressure were observed for different prototypes in the flow loop experiments.

3.3.1 Static Inflation

The capacitance of each DWSG prototype was calculated as defined by Equation 3.1. Prototypes were fabricated with a total length of approximately 18cm, but all tests were conducted with a standard length of 15cm by mounting each prototype within the same fixture that had 2.54 cm (1") diameter barbed hose connections with inlets spaced 15 cm apart. The fixture had caps on either end to create a closed system once the prototype was inserted. Two ports in the fixture were used for connection of (1) a syringe for addition and removal of fluid and (2) a pressure transducer (P55, Validyne Engineering, Northridge, CA) to record lumen pressure at each volume. All tests were conducted at room temperature.

For a given test, the DWSG prototype was mounted in the fixture using hose clamps. A syringe was used to fill the prototype with a given gas charge, which was recorded as the gas volume at atmospheric pressure. The lumen of the closed system was evacuated of air and filled with water. The pressure sensor was used to ensure that the lumen pressure was ultimately returned to atmospheric level, which was set as a zero point. A syringe pump (KD Scientific, Holliston, MA) mounted with a 10mL syringe was used to add water to the lumen in 0.5 mL stepwise increments while the pressure was simultaneously recorded. Following 10 mL injection, or if lumen pressure approached the 300 mmHg limit of the pressure sensor, the pump was reversed to remove 0.5 mL increments of water until pressure returned to zero. This procedure was followed twice for each prototype for a total of four pressure measurements at each lumen volume. Measurements from the pressure sensor were collected with a Matlab script (Mathworks, Natick, MA) via a USB-connected DAQ (MicroDAQ, Contoocook, NH). A volume-pressure curve was constructed for each prototype, and capacitance was calculated as a function of lumen pressure by finding the slope between adjacent points.

To estimate the flow resistance of the different DWSG prototypes, photos were taken down the lumen of the DWSG at each gas charge. The cross-sectional area of the lumen for each case

was measured by tracing it in ImageJ [137]. These estimates were used to calculate flow resistance with Poiseuille's law, assuming constant cross section along the length of the prototype. We knew that the assumption of constant cross section would not be true in practice, but it provided a convenient and conservative (high) estimate of resistance.

3.3.2 Flow Loop

The goal of the flow loop experiments was to simulate implantation of the DWSG into the aorta to predict the effect of different configurations on blood pressure. The flow loop system (**Fig. 3.3**) consisted of a pulsatile flow pump, a compliant arch, a fixture for DWSG prototypes, flexible tubing, a needle valve, and a storage reservoir. The only component of the system that changed between experiments was the prototype placed in the fixture.

The pump (EnvivoPC, Maximum Fidelity Surgical Simulations) enabled control of the stroke volume and pulse rate. The compliant arch was constructed by painting layers of liquid latex onto a curved latex balloon base via a blotting technique (cf. [138]) to an approximate thickness of 3.8 mm. The arch was circumferentially reinforced at four locations with vinyl tape to restrict expansion and maintain relatively low compliance. The compliance of the arch was not experimentally quantified, but it remained constant throughout all experiments and was estimated through the Windkessel model optimization, as described later in Section 3.4.2. The prototype fixture enforced a DWSG length of 15 cm as in the static inflation tests, and it was mounted in the flow loop at a position representing the descending thoracic aorta. A 2.54 cm (1") diameter semi-compliant tube (Clearflex 60 PVC) downstream of the prototype fixture represented the abdominal aorta, followed by a needle valve that was set to emulate the peripheral vascular resistance and to maintain physiologic pressure ranges in the DWSG. The outlet of the needle valve was connected to the reservoir that fed the pump, thus forming a closed loop. To maintain constant outlet pressure, the outlet drained above the fill level of the reservoir to open air. This required the outlet to be

elevated above the inlet, but the resulting hydrostatic pressure was measured and subtracted off in all reports of pressure.

Flow rate was measured upstream of the arch with two flow-through meters (Gems Sensors, Plainville, CT) to capture the wide range of flow rates (0 to >100 mL/s) over each pump cycle. Pressure was measured at two locations in the system: directly upstream of the DWSG (Validyne) and upstream of the needle valve (Harvard Apparatus, Holliston, MA). Only measurements from the transducer upstream of the DWSG were used for the analyses in this paper.

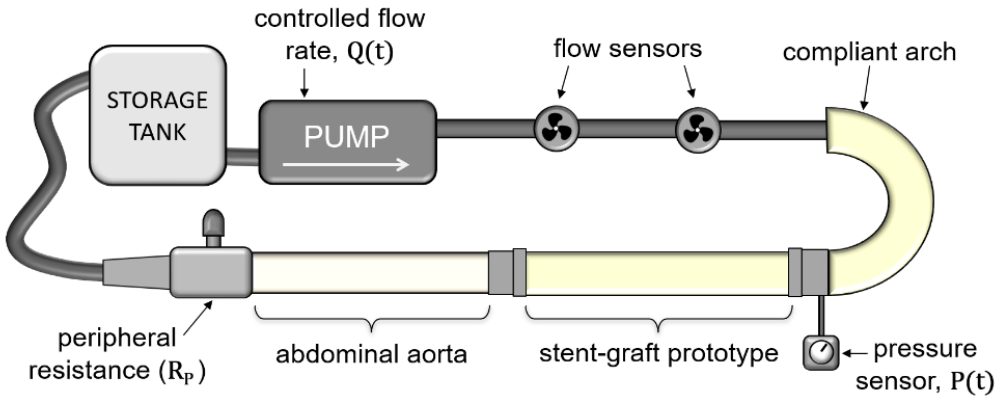


Figure 3.3: Experimental flow loop diagram. Diagram of the flow loop setup used for in vitro measurements of pressure change caused by the DWSG prototypes. The full model is designed to simulate the aorta and peripheral vasculature; the DWSG prototype is positioned in the descending thoracic aorta.

Water was used as the working fluid in all experiments because viscous effects were not expected to have a major influence on the general behaviors observed for different DWSG prototypes. This expectation was reasonable based on the moderately high (~1000) average Reynolds number in the system, but some flow loop cases were duplicated with a high viscosity glycerol-water solution to verify that trends were consistent. The same trend in pulse pressure was found between the water and glycerol tests, but no discernable trend in peak pressure was found in the glycerol trials due to large variation in the mean pressure.

Both pressure transducers were zeroed at atmospheric pressure before connection to the flow loop, and lumen pressure was recorded with respect to the atmosphere. Measurements from the flow and pressure sensors were collected with a DAQ and MATLAB script as in the inflation experiments. Data collection was initiated for each trial after the pump had run at least 10 cycles at the current setting and was terminated after 30 seconds.

Pressure upstream of the DWSG was analyzed to extract a maximum, minimum, and mean value for each cycle. Data from all cycles were averaged and combined with other trials of the same test condition. Pulse pressure, defined as the difference between maximum and minimum pressures, was also calculated.

To evaluate the effect of the independent variables (gas charge, inner wall diameter, and inner wall prestretch) on pressure changes, normalized peak and pulse pressure data were both fit with linear models. The average pressure from each test condition was normalized against the zero-gas-charge pressure for the same inner wall configuration; this process set all of the zero-gas-charge cases to zero and removed the effect of mean pressure variability caused by perturbations to the reservoir level. The linear models (Eq. 3.2) included non-interacting terms for gas charge V_g, ratio of inner wall to outer wall diameter d, and inner wall prestretch λ, with respective coefficients c_V, c_d, and c_λ. An additional coefficient c_0 specified the intercept for the equation.

$$\hat{P} = c_0 + c_V \cdot V_g + c_d \cdot d + c_\lambda \cdot \lambda \tag{3.2}$$

Equation 3.2 was used for both peak and pulse pressure models, so $\hat{P}$ is a placeholder variable that could refer to either normalized peak pressure or normalized pulse pressure. Coefficients for each pressure measure were found using the *lm()* function in RStudio [139]. Each data point was weighted by the inverse of its variance. The P value for each coefficient being nonzero was found using a two-sided t-test, with the significance criterion set as $p < 0.05$.

3.3.3 Experimental Design

A total of 28 DWSG configurations were tested by varying inner wall diameter, inner wall prestretch, and gas charge (**Table 3.1**). These cases were compared to a rigid stent-graft case, in which zero gas charge was added to any of the DWSG prototypes. A smaller range of gas charges was tested when the inner wall prestretch was lower because the lumen became almost completely occluded at 60 mL gas charge, causing pressures to exceed measurable range. Flow loop experiments were conducted with the pump set to a stroke volume of 30 mL, with pulse rates of 40 and 60 beats per minute. Two additional runs with the same pulse rates and a stroke volume of 15 mL were conducted with zero gas charge to ensure that enough data were available for model optimization. The flow loop was modeled using a three-element Windkessel model, described below in Section 3.4.2.

Table 3.1: DWSG configurations tested in static and flow loop experiments

Inner wall diameter (cm)	Prestretch (%)	Gas charges (mL at P = 1 atm)
1.91 (3/4”)	5	10, 20, 30, 40, 50
	50	10, 20, 30, 40, 50, 60
2.22 (7/8”)	5	10, 20, 30, 40, 50
	50	10, 20, 30, 40, 50, 60
2.54 (1”)	50	10, 20, 30, 40, 50, 60

3.4 Computational Methods

Two different computational models were developed to describe the DWSG and predict its effect on blood pressure. In both models, performance of the DWSG is expressed in terms of resistance and capacitance.

3.4.1 DWSG Finite Element Model

An axisymmetric, quasistatic finite element (FE) model was developed to reproduce behavior observed in the static inflation experiments and to predict behavior for untested configurations. An axisymmetric model of the DWSG inner wall was created in Abaqus (Dassault Systèmes, Vélizy-Villacoublay, France) using membrane-type elements to represent the thin latex tube. A mesh of the membrane with 200 elements was used for all computations. The outer wall was modeled as a fixed rigid boundary at a radius of 1.27 cm (½"). A prestretch condition was applied to the latex tube by holding one edge fixed and axially displacing the opposite edge by the appropriate distance. For tubes with a smaller radius than the outer wall, both edges were then displaced to a radius of 1.27 cm to simulate stretching the tube around the outer wall. The edges were held in this position for subsequent steps, in which a series of pressures was applied to the outer face of the tube, representing inflation of the DWSG with different gas charges. To minimize computational cost, behavior of the confined gas was not considered in the FE model itself. Rather, the output of the model was the volume of the gas layer at different pressure differentials ($P_{gas} - P_{lumen}$) based only on mechanical stresses in the inner wall (**Fig. 3.4A**). Since only the transmembrane pressure difference matters in constructing the curve in **Fig. 4A**, a family of $P_{gas} - P_{lumen}$ curves (solid lines in **Fig. 3.4B**) can be generated for different P_{lumen} values simply by shifting the original curve. Additional information is available from the Ideal Gas Law ($P_1V_1 = P_2V_2$ for an isothermal, closed system), allowing the generation of a second set of V_{gas} versus P_{gas} curves (dashed lines in **Fig. 3.4B**). Thus, for a given P_{lumen} and gas charge, the final configuration can be determined from the intersection of the two curves.

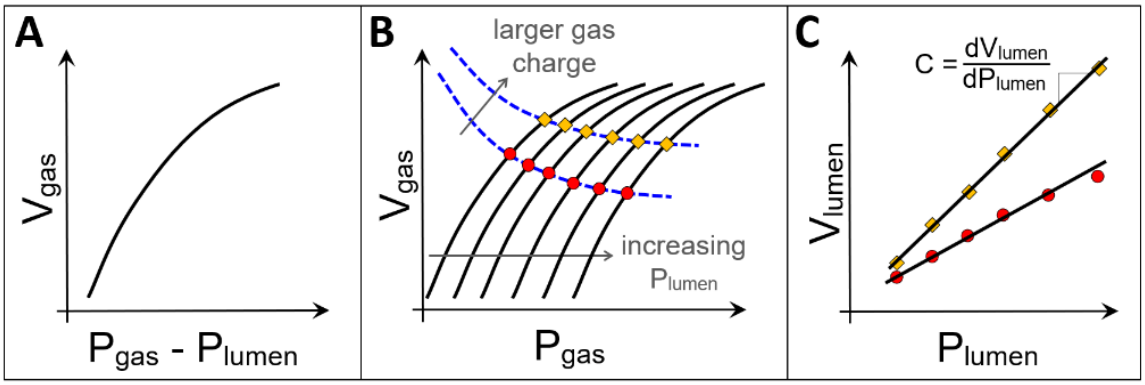


Figure 3.4: Calculation of DWSG capacitance. Workflow for calculating capacitance from the FE model, where (A) is an example curve due to inner wall deformation, and (B) shows that curve (solid lines) translated into gas volume versus pressure, with Ideal Gas Law curves (dashed) intersecting at points that give the true behavior of the DWSG system. In (C), those intersection points are plotted to show how the lumen volume changes with lumen pressure. The slope of this trend for a given gas charge is the DWSG capacitance.

Next, a curve of V_{lumen} versus P_{lumen} was generated from the intersections in **Fig. 3.4B** at a series of P_{lumen} values (**Fig. 3.4C**). The slope of this curve was calculated to specify the capacitance for that case. A different curve was generated for each gas charge, for each inner wall diameter, and for each prestretch level.

The flow resistance, R, of the DWSG was estimated for Poiseuille flow by integrating the inner wall radius, r, over the total axial length of the device, L (Eq. 3.3),

$$R = \int_0^L \frac{8\mu}{\pi r^4} dx \tag{3.3}$$

where r is a function of axial position x. The viscosity μ was set to $3.45 \times 10^{-3} Pa \cdot s$ for blood to calculate physiologically relevant resistance values, although water was used for the experiments.

3.4.2 Windkessel Model

The three-element Windkessel (**Fig. 3.5A**) [102] was first used to capture the behavior of the DWSG in the experimental flow loop system; then it was used with published parameter values for the arterial system to predict the effect of the DWSG on blood pressure in a patient.

3.4.2.1 Flow Loop Model

Because the flow loop system was built to mimic the human arterial system, it was reasonable to model it using the three-element Windkessel. We chose not to use the four-element Windkessel because it would provide only incremental improvement over the chosen model, and we wanted to minimize the number of parameters to estimate. One modification to the standard Windkessel was that the peripheral resistance R_P had contribution from two sources (Eq. 3.4).

$$R_P = R_{DWSG} + R'_P Q \tag{3.4}$$

The linear component R_{DWSG} accounted for the flow resistance introduced by the DWSG prototype, while R'_P represented the needle valve, for which the pressure drop followed orifice flow behavior and had a squared relationship with flow rate Q. Note that the units of R'_P must be different from a normal resistor, to cancel the units of volumetric flow rate Q. The experimentally measured flow rate from the flow loop, $Q(t)$, was the input to the model (**Fig. 3.5B**), and the pressure drop across the system, $P(t)$, was the measured output. The model was evaluated in the frequency domain for the first 200 harmonics obtained when the flow rate was decomposed using a Fourier series (dashed curve, **Fig. 3.5B**) [140].

Parameter optimization was first conducted for a "rigid stent-graft" case, where the DWSG prototype had zero gas charge ($R_{DWSG} = 0$ in Eq. 3.4), so the inner wall was flush against the stiff outer wall. This case was used to find values for R_C, C_0, and R'_P, where R_C was resistance of the system upstream of the DWSG prototype and C_0 represented capacitance of the elastic arch and other flexible tubing throughout the system. Parameters were determined using *fminsearch()* in Matlab by minimizing the error between pressure waveforms in the model and in the experiment

for a series of flow conditions. Half of the experiments were used to optimize the parameters, and the other half were used to assess the predictive capability of the model.

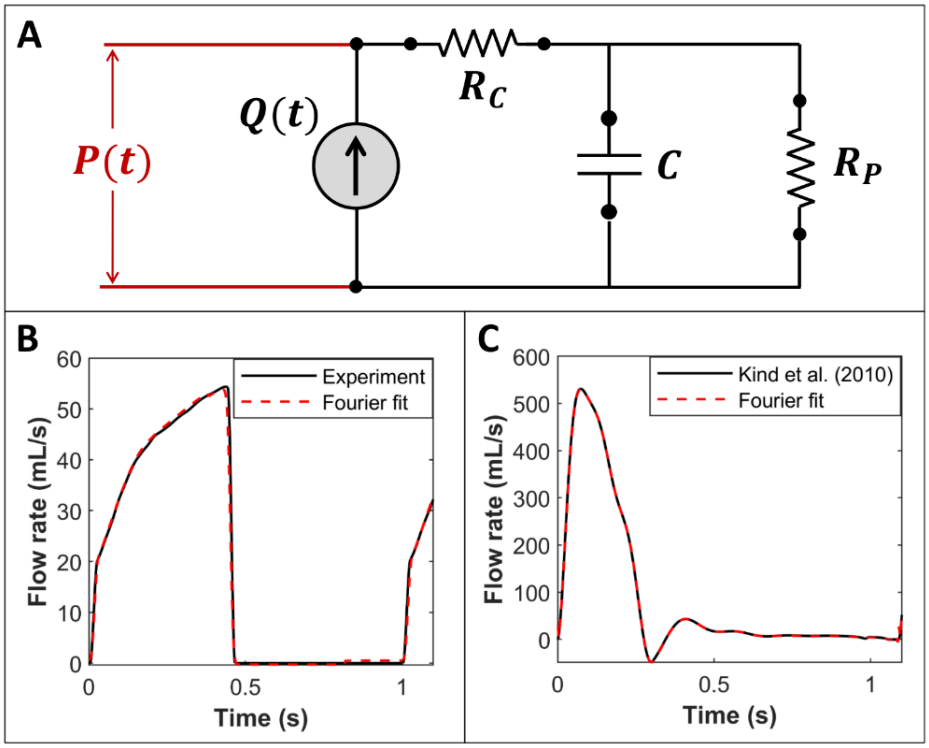


Figure 3.5: Windkessel model and input flow rates. (A) Diagram of the three-element Windkessel model used to replicate flow loop measurements and predict physiologic behavior. P(t) is the pressure measurement across the system, Q(t) is the flow rate input, R_C is the characteristic impedance, C is capacitance, and R_P is the peripheral resistance. (B) Input flow rate Q(t) used in the Windkessel model for the flow loop. Solid line is the measured flow from the flow experiments, and the dashed line is the Fourier series representation of that curve, which was used in Windkessel calculations. (C) Input flow rate Q(t) used in the Windkessel model of the human arterial system [27]. Solid line is the flow reported in literature, and the dashed line is the Fourier series representation of that curve, which was used in Windkessel calculations.

The optimization procedure was repeated for each nonzero gas charge, but now R_C, C_0, and R_P' were held fixed and values for C_{DWSG} and R_{DWSG} were estimated. The value of C_{DWSG}, which represented capacitance of the DWSG prototype, was calculated by subtracting C_0 from the total capacitance output by the optimization. These estimates were compared to the capacitance and resistance values from static measurements in Sections 3.3.1 and 3.3.2. We hypothesized that the

static capacitance calculation would overpredict the apparent dynamic capacitance because the DWSG gas layer would not have time to fully compress over the course of a single pump stroke before expanding again when the flow rate (and pressure) dropped.

3.4.2.2 Arterial Model

After we had completed the Windkessel parameter optimization for the flow loop experiment, the optimized DWSG parameters were used to make predictions about how the DWSG would affect blood pressure when implanted into a human aorta. These predictions were made for both a normotensive and a hypertensive patient, to assess whether the DWSG would have different impact depending on the condition of the patient's arterial system. Characteristic impedance R_C and peripheral resistance R_P were set to values reported by Kind et al. [108] for normotensive and hypertensive patients.

In order to divide capacitance C into the contributions of different aortic regions, a literature search was conducted to find average length L_i, radius r_i, wall thickness h_i, and stiffness E_i for the ascending aorta and arch ($i = 1$), the descending aorta ($i = 2$), and the abdominal aorta ($i = 3$) [6,7,30,57]. The resistance R_i of each segment was calculated using Eq. 3 and added to R_P. Resistance of the aorta is negligible compared to the peripheral resistance, but we included it in the total resistance in order to observe the effect of DWSG resistance at high gas charge. The capacitance C_i of each aortic segment was calculated using Eq. 5, which was derived from Law of Laplace for thin-walled pressure vessels. Poisson's ratio $\nu = 0.5$ was used under the assumption that the vessel wall is incompressible. **Table 3.2** summarizes the aortic properties and the calculated capacitance and resistance. The normotensive case was developed using the aortic properties reported for people under 30 years of age, and the hypertensive case used properties for people over 70 years.

$$C_i = \frac{\left(1 - \frac{\nu}{2}\right)\pi r_i^3 L_i}{E_i h_i} \tag{3.5}$$

Table 3.2: Properties of the aorta found in literature [6,7,30,57]. These values were used to calculate Windkessel parameters for aortic resistance R and capacitance C .

Regional Property				Age < 30 yrs.	Age > 70 yrs.
ASCENDING	L_1	(cm)	[57]	10.0 ± 0.7	13.1 ± 1.4
	r_1	(cm)	[57]	1.38 ± 0.14	1.66 ± 0.21
	E_1	(kPa)	[6]	13.5	100
	h_1	(cm)	[30]	0.180	0.290
	C_1	(mL/mmHg)		3.40	0.649
	R_1	(mmHg·s/mL)		1.82×10^{-4}	1.14×10^{-4}
DESCENDING	L_2	(cm)	[57]	13.9 ± 1.6	14.3 ± 1.3
	r_2	(cm)	[57]	1.03 ± 0.08	1.21 ± 0.13
	E_2	(kPa)	[6]	13.9	56.8
	h_2	(cm)	[30]	0.176	0.215
	C_2	(mL/mmHg)		1.95	0.652
	R_2	(mmHg·s/mL)		8.14×10^{-4}	4.40×10^{-4}
ABDOMINAL	L_3	(cm)	[57]	15	15
	r_3	(cm)	[57]	0.91 ± 0.07	1.07 ± 0.16
	E_3	(kPa)	[7]	51	337
	h_3	(cm)	[30]	0.114	0.192
	C_3	(mL/mmHg)		0.611	0.0892
	R_3	(mmHg·s/mL)		1.44×10^{-4}	7.54×10^{-4}

The capacitance values found via Eq. 3.5 were much larger than those typically reported for use in an arterial Windkessel model. To resolve this inconsistency, the values in **Table 3.2** were used only to find the relative contribution of each aortic segment to the total capacitance. After establishing these proportions, the actual capacitance attributed to each segment was given by the total capacitance reported in [108] multiplied by the appropriate proportion.

Baseline blood pressures for the unstented cases were found by running the Windkessel model with literature values only [108]. Because the target location for the DWSG is the descending aorta, capacitance and resistance in this region were changed to simulate placement of different stent-graft configurations. Placement of a rigid stent-graft was modeled by setting $C_2 = 0\, mL/mmHg$ and leaving R_2 unchanged. For each DWSG case, the capacitance values were taken from the average Windkessel fits from Section 3.4.2.1. Resistance measurements were taken from the FE

model (Section 3.4.1). A healthy aortic flow rate was used for $Q(t)$ with a pulse rate of 55 beats per minute (**Fig. 3.5C**) [108]. The systolic, diastolic, and mean pressures were calculated for each simulation and were compared to the unstented and rigid stent-graft pressures.

3.5 Summary of Results

Section 3.6 reviews the capacitance and resistance of the DWSG, as determined by the static model and experiments, as well as the Windkessel optimization. In Section 3.7, dynamic behavior of the DWSG is first evaluated within the experimental flow loop, and then predictions about physiologic pressure changes are made by using the capacitance and resistance values in the Windkessel model.

3.6 Characterizing the DWSG

An example mesh from the FE model is shown in **Figure 3.6A** for a series of gas charges, at two different lumen pressures. At a given lumen pressure, a higher gas charge led to smaller lumen volume. When lumen pressure was increased, the lumen volume also increased, for a given gas charge. For each inner wall configuration, there was a positive gas charge that led to zero pressure differential between the gas and the lumen. Adding more gas led to a positive gauge pressure in the gas layer, while adding less gas led to a negative gauge pressure. No notable discontinuities arose in DWSG behavior when transitioning between negative and positive gauge pressures.

3.6.1 DWSG Capacitance

Pressure-volume relationships for each DWSG case were obtained from both the FE model and the inflation experiment. The capacitance for each case was estimated by taking the slope of the pressure-volume relationship for lumen pressures between 40 and 250 mmHg. Linearity was a reasonable approximation within these bounds for both the model (**Fig. 3.6B**) and experiment (**Fig. 3.6C**), although both showed slightly sublinear behavior. Given that the FE model parameters were not adjusted to fit the experiments, the agreement between the model predictions (**Fig. 3.6B**) and

the experimental measurements (**Fig. 3.6C**) was quite good. The model could not be evaluated for all cases because buckling of the inner wall caused the model to fail; this behavior was observed most often with high gas charges.

Another estimate of capacitance was obtained by fitting the flow loop experiments to a Windkessel model. Parameters of the system were obtained through an optimization routine that minimized error between Windkessel-predicted and experimentally measured pressure profiles when the rigid stent-graft was placed. DWSG resistance and capacitance were found by repeating the optimization for each case and subtracting off the values from the rigid case. This procedure assumed that both resistance and capacitance of the rigid stent-graft prototype were negligible, which was consistent with zero-gas measurements obtained with the other methods.

Figure 3.7 compares capacitance measurements from the static FE model, the inflation experiments, and the Windkessel fit for each DWSG case. An increase in capacitance was observed with larger gas charge for all inner wall diameters at both prestretch levels. The three measurement techniques were in good agreement with each other. For all five cases (**Fig. 3.7A-E**), the FE model underpredicted the experimentally measured capacitance, possibly due to nonzero compliance of the outer wall in the prototypes used with the experiment. This discrepancy is clear when looking at the average capacitance over all inner wall configurations for each gas charge (**Fig. 3.7F**), where the FE model trends toward zero capacitance at zero gas charge, whereas a capacitance of 0.0081 ± 0.0085 mL/mmHg was measured for zero gas charge in the experiment. The method for calculating capacitance with the Windkessel model also led to zero capacitance at zero gas charge, so these values tend to align more with the FE model than the inflation experiment.

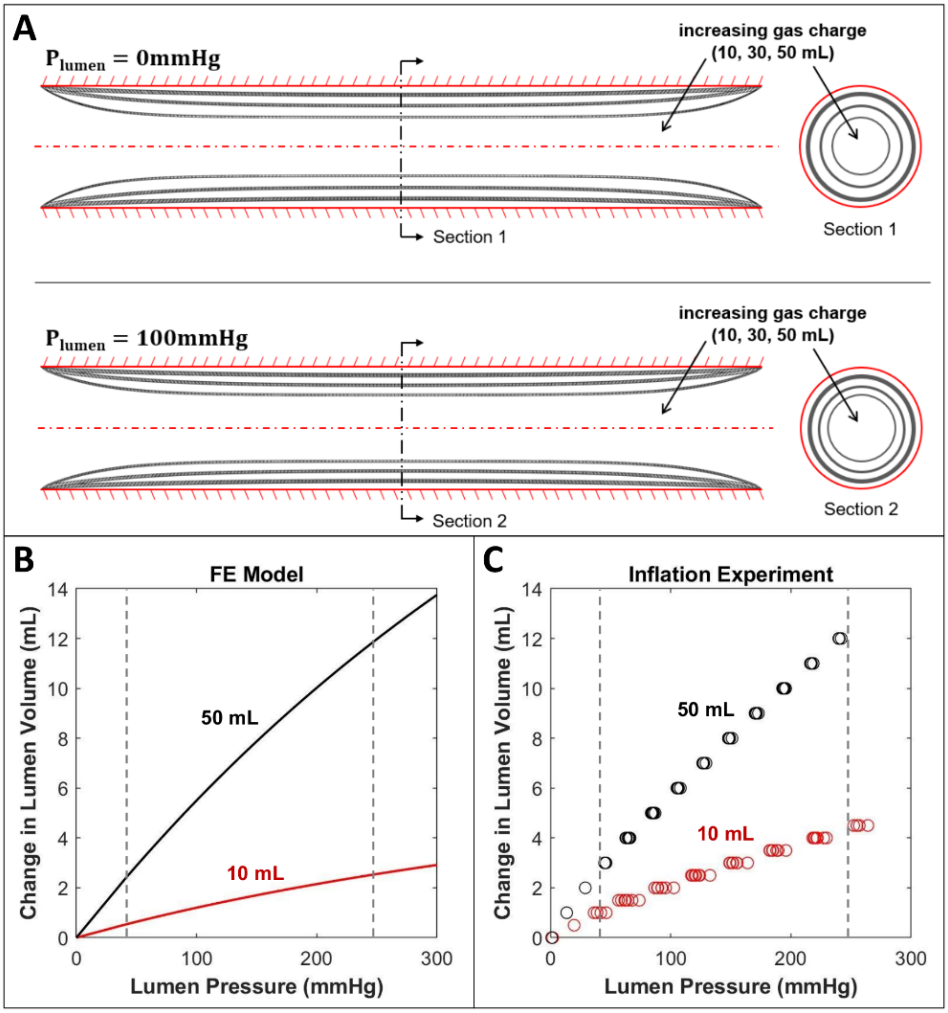


Figure 3.6: DWSG static finite element model. (A) Example FE model output for a range of gas charges at two lumenal pressures (0 and 100mmHg). The pressure-volume relationships for two gas charges are shown for the FE model (B) and the inflation experiment (C). Dashed lines show bounds on lumen pressure, between which the slope was measured. All panels show results for the 1.91cm (¾") diameter inner wall, 50% prestretch DWSG case.

For any given gas charge, there was very little difference in capacitance among the different inner wall configurations. The FE model showed some dependence on inner wall configuration at large gas charges, as seen by a wider confidence interval in the calculated average capacitance (**Fig. 3.7F**); this dependence was not evident from the inflation or Windkessel methods. Overall, a linear relationship between gas charge and capacitance was apparent, especially at lower gas charges.

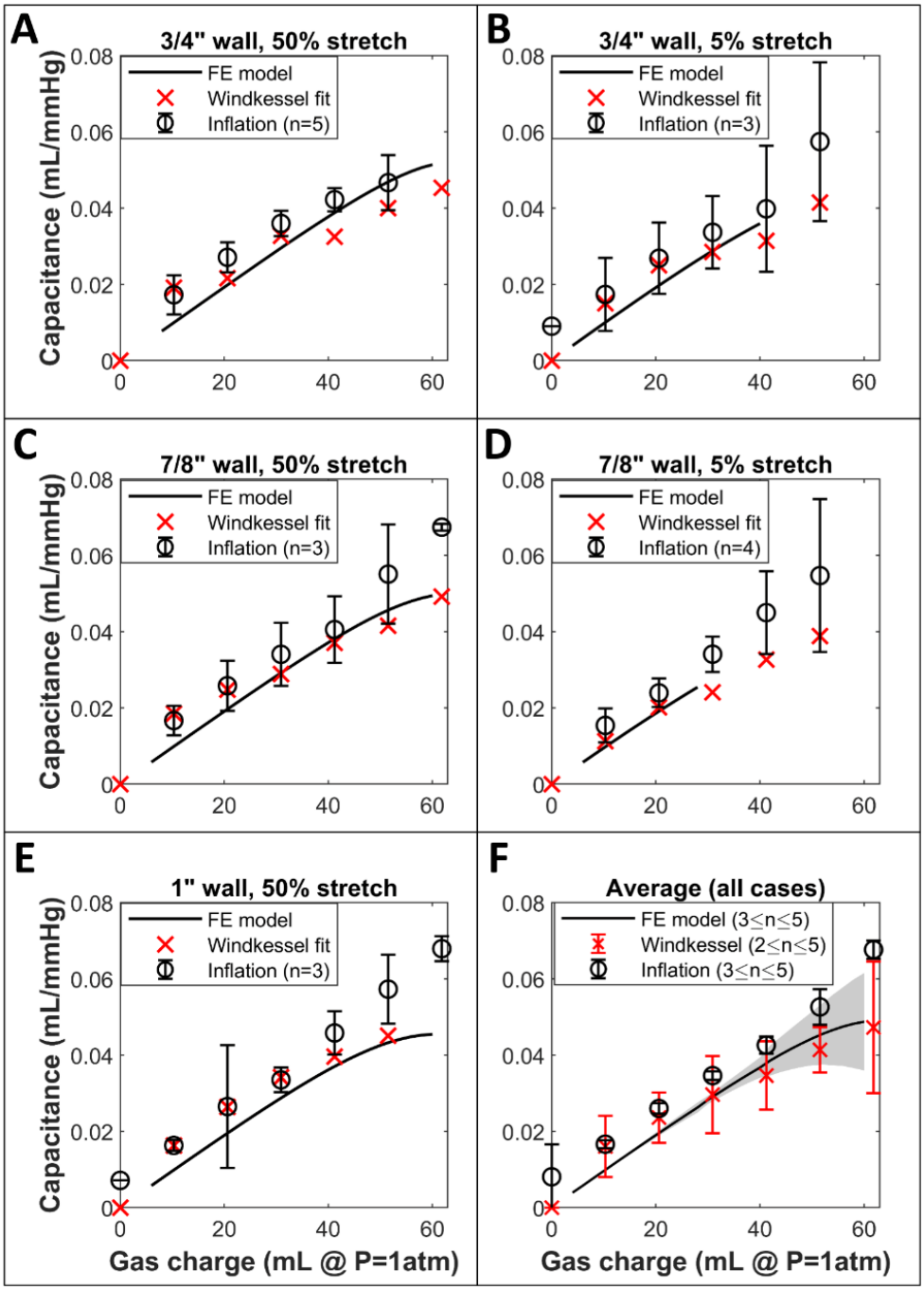


Figure 3.7: Capacitance measurements of the DWSG. (A-E) Capacitance of different DWSG cases, as measured by the FE model, the Windkessel model fit to flow experiments, and the inflation experiments. Rows separate inner wall diameters and columns separate inner wall prestretches. (F) Average capacitance over all cases for both model and experiment. All error bars show 95% CIs.

3.6.2 DWSG Resistance

The flow resistance of each DWSG configuration was calculated using Equation 3.2, with radius measurements from the FE model and the prototypes. In cases where the inner wall of the prototype had buckled, the hydraulic diameter at the narrowest cross section was used in the equation. **Figure 3.8A** shows resistance measurements for the 1.91 cm (¾") diameter, 50% prestretch inner wall case. There is good agreement between the model and prototype until the inner wall of the prototype has buckled at 50 mL gas charge, causing the resistance to spike. **Figure 3.8B** shows the profile of the DWSG inner wall for gas charges from 10 to 60 mL for the FE model and the inflation. The FE model did not predict that the inner wall would buckle until above 60 mL gas charge, but the premature buckling in the inflation could be explained by a natural crease present in the latex tubing that was used to construct the inner wall of the prototype. The crease is visible in **Fig. 3.8B** at 40 mL gas charge before full buckling has occurred at 50 mL charge.

Resistance from the Windkessel fit was not comparable to the static measurements because the low viscosity of water (used in the flow experiments) caused the values to be extremely small (~10^{-12} mmHg·s/mL). Minor variability in the mean pressure in the flow loop, due to changing reservoir level between experiments, caused significant variation in the fitted resistance.

3.7 Dynamic Behavior

3.7.1 Flow Loop Measurements

The effect of different DWSG configurations on dynamic pressure was measured in an *in vitro* flow loop. Although multiple flow rates were tested to conduct Windkessel optimization, only the 60 beats/minute, 30 mL stroke volume flow case was used when reporting pressure changes. **Figure 3.9A** shows an example pressure profile from the flow loop measurements (solid line) and the corresponding fit achieved with the Windkessel model (dashed line).

As gas charge was increased, peak pressure (**Fig. 3.9B**) and pulse pressure (**Fig. 3.9C**) both decreased. At 60 mL gas charge, an 8% reduction in peak pressure was observed with respect to

the rigid stent-graft case (**Fig. 3.9D**). Pulse pressure changed more significantly, with a 24% decrease compared to the rigid case (**Fig. 3.9E**). Different inner wall configurations for the DWSG appeared to have negligible effect on system pressure. This observation is consistent with the static results that showed the gas charge dominating the capacitance and resistance measurements.

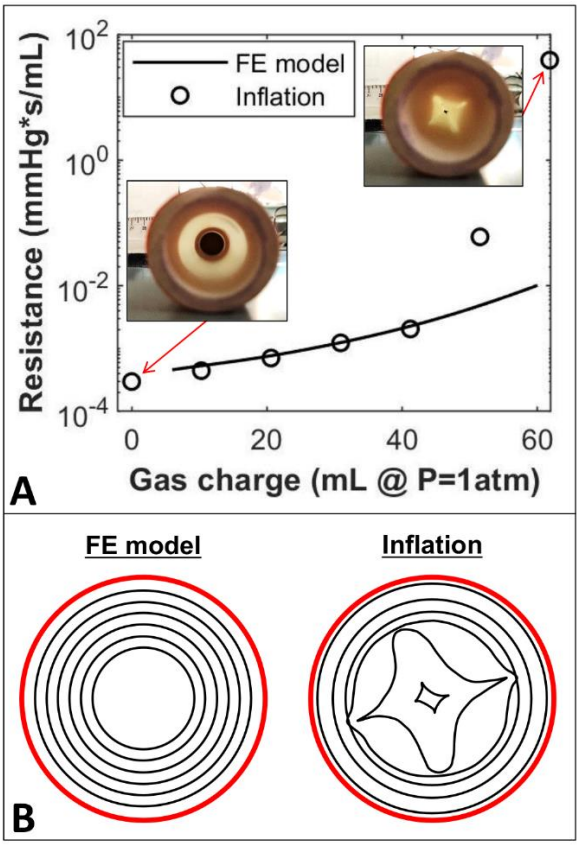


Figure 3.8: DWSG flow resistance. (A) Poiseuille resistance of the 1.91 cm (¾") diameter, 50% prestretch inner wall DWSG case, calculated from the FE model and the prototype inflation. Photos of the prototype show the lumen cross section for 0 and 60 mL gas charges. (B) Comparison of cross-sectional profiles for the model and prototype from 10 to 60 mL gas charge (outside to inside). Each ring shows the position of the inner wall at a given gas charge, when a cross section is taken at the midpoint along the axial length. The thick outer ring represents zero gas charge, when the inner wall is flat against the outer wall.

The normalized peak and pulse pressure data (**Fig. 3.9D-E**) were both fit to linear models of the form given in Equation 3.2. The coefficients and their corresponding P values are reported in **Table 3.3**. For both the peak and pulse pressure measures, the only variable with significant

contribution to the pressure change was gas charge. Normalized peak pressure exhibited a negative dependence on gas charge with $c_V = -0.134 \pm 0.005\ mL^{-1}$ (mean ± SE), while normalized pulse pressure showed a stronger correlation with $c_V = -0.372 \pm 0.013\ mL^{-1}$. The P value for both of these coefficients was well below the cutoff for significance. The coefficient for inner wall diameter c_d was significant in the pulse pressure model ($p = 0.048$), though the uncertainty in the coefficient value was quite large ($c_d = -6.67 \pm 3.22$).

Table 3.3: Coefficients for the linear models relating normalized peak and pulse pressures to design variables. Gas charge (c_V), inner wall diameter (c_d), and inner wall stretch (c_λ). Model intercept is given by c_0. SE refers to the standard error. P values reported from a two-sided t test.

	Coeff.	Value ± SE	P value
Peak Pressure	c_0	-0.322 ± 1.322	0.809
	$c_V\ \ (1/mL)$	-0.134 ± 0.005	<2e-16
	c_d	-1.115 ± 1.183	0.354
	c_λ	0.527 ± 0.559	0.354
Pulse Pressure	c_0	2.429 ± 3.448	0.487
	$c_V\ \ (1/mL)$	-0.372 ± 0.013	<2e-16
	c_d	-6.670 ± 3.219	0.048
	c_λ	1.038 ± 1.521	0.500

3.7.2 Physiologic Predictions with the Windkessel Model

The Windkessel model was evaluated to predict the effect of the DWSG versus a rigid stent-graft when placed in the descending thoracic aorta of normotensive and hypertensive patient models. DWSG capacitance and resistance were defined using values from the FE model (**Table 3.4**). Because inner wall properties were not found to be significant, the average values for each gas charge were used in this model. Flow rate $Q(t)$ was set to a physiologic signal, and the resulting pressure profiles from the rigid stent-graft case are shown in **Fig. 3.10A**. The hypertensive case had significantly higher pressures compared to the normotensive case for all gas charges.

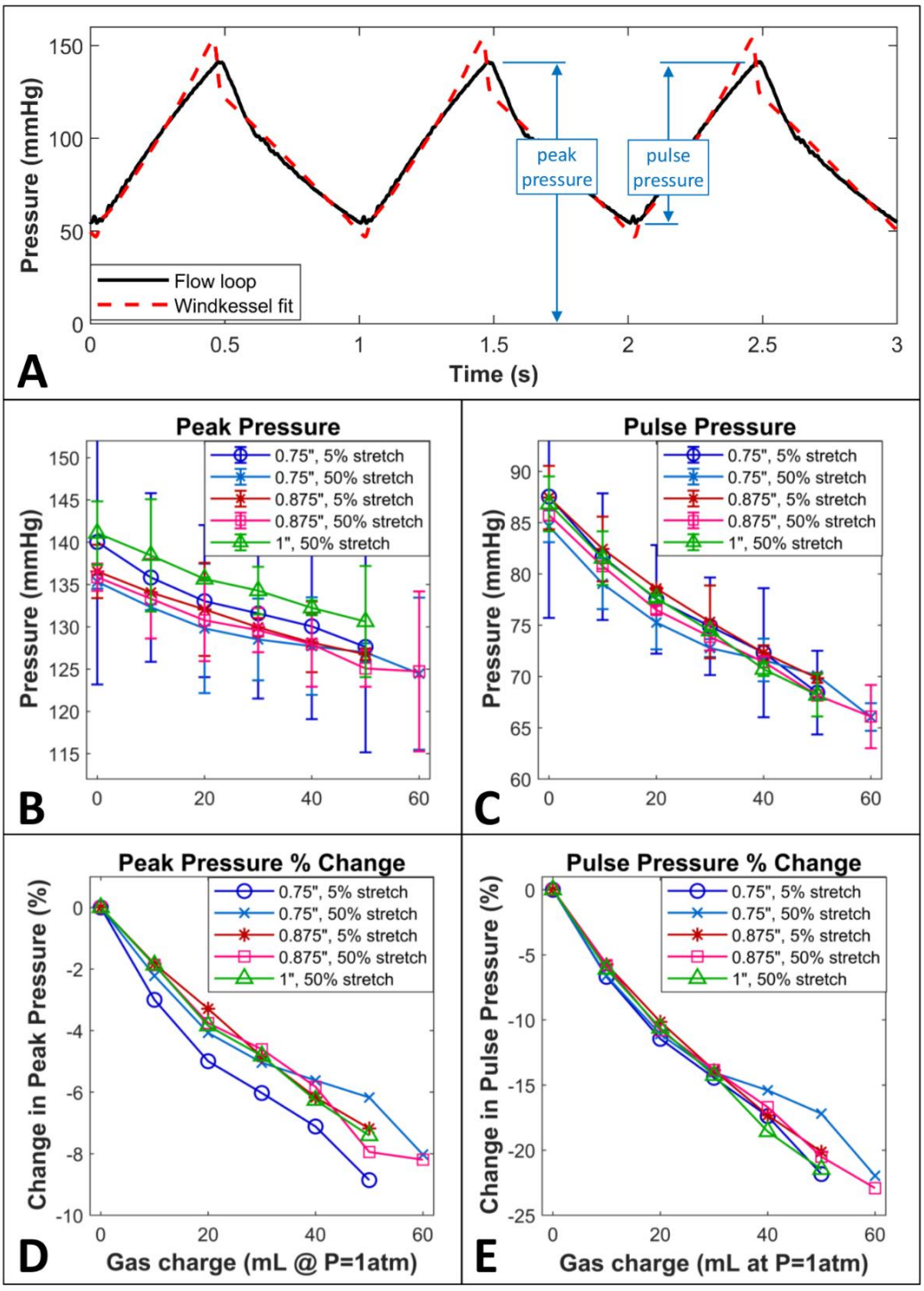


Figure 3.9: Flow loop pressure measurements. (A) Example pressure wave measured from the flow loop (solid line), with the Windkessel fit for that measurement shown with a dashed line. The definitions for peak and pulse pressures are identified with arrows on the plot. (B) Peak pressure and (C) pulse pressure for each DWSG case as a function of gas charge; 95% CI shown for n=2. (D) Percent change in peak pressure and (E) pulse pressure; CI omitted from (D) and (E) for clarity.

Table 3.4: Capacitance and resistance measurements of the DWSG used for physiologic predictions in the Windkessel model. Capacitance values are taken from the Windkessel fit to flow loop data, and resistance values are from FE model measurements. Reported as mean ± 95% confidence interval.

Gas Charge (mL)	Capacitance (mL/mmHg)	Resistance ($x10^{-4}$ mmHg·s/mL)
0	0	3.85
10	0.0160 ± 0.0081	5.19 ± 0.14
20	0.0236 ± 0.0066	7.34 ± 0.36
30	0.0296 ± 0.0101	11.0 ± 1.4
40	0.0346 ± 0.0089	19.0 ± 5.3
50	0.0414 ± 0.0060	39 ± 16
60	0.0472 ± 0.0172	86 ± 68

Increasing gas charge always decreased both the peak and pulse pressure (**Fig. 3.10B-C**), but neither measure returned to the unstented value for even the largest gas charge (60 mL). **Figure 3.10D** shows that a rigid stent-graft increased peak pressure by 25% in a hypertensive patient and 10% in a normotensive patient, compared to the pressure in the unstented aorta. At maximum gas charge, this pressure increase compared to the unstented case was only 19% in the hypertensive patient, while the 10% increase persisted for the normotensive patient. The rigid stent-graft had a greater effect on pulse pressure (**Fig. 3.10E**) with 72% and 40% increases for the hypertensive and normotensive patients, respectively. The increase in pulse pressure reduced to 66% at 60 mL gas charge for the hypertensive patient, while it decreased to 35% for the normotensive patient. In **Fig. 3.10D**, it appears that the normotensive patient would receive maximum benefit at 50 mL gas charge, with pressure increasing slightly for 60 mL. This result reminds us that a balance must be maintained between the benefit of increased capacitance and the cost of increased fluid resistance.

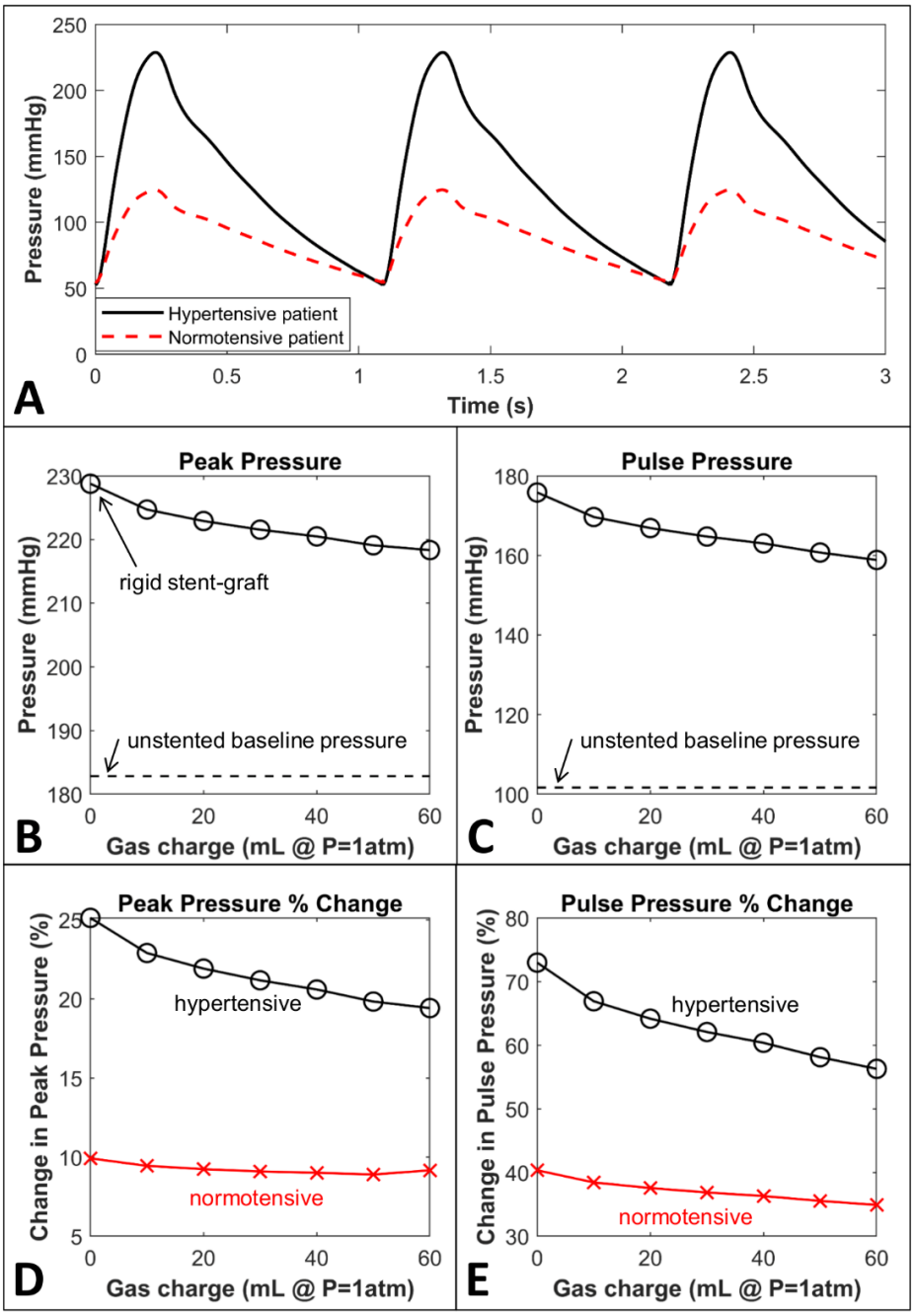


Figure 3.10: Windkessel pressure predictions. (A) Example pressure waves for hypertensive (solid line) and normotensive (dashed line) patients with a rigid stent-graft, as predicted by the Windkessel model with physiologic input parameters [27]. (B) Peak pressure and (C) pulse pressure for each DWSG gas charge, as predicted by the physiologic Windkessel model. The baseline pressure with no stent-graft is shown by the dashed line in both (B) and (C). Only the hypertensive case is shown for clarity, due to a large difference in pressure range compared to the normotensive case. Percent change in (D) peak pressure and (E) pulse pressure, compared to the unstented condition for both hypertensive ('o') and normotensive ('x') cases.

3.8 Discussion

3.8.1 Double-walled Stent-graft (DWSG) Design

We have created a double-walled aortic stent-graft design with the goal of addressing the issue of persistent high blood pressure in patients who receive standard, inextensible stent-grafts. The design leverages the compressibility of biocompatible gas to provide fluid capacitance to the arterial system without requiring the aorta itself to be distensible. Prototypes of the design were fabricated with PVC tubing for the stiff outer wall and latex tubing for the flexible inner wall. Different gas charges and inner wall diameters were compared. The impact of inner wall stiffness was also evaluated by prestretching the inner walls to different levels before mounting them in the prototype. These simplified prototype models were used to assess the pressure-reduction capability of the design and to identify which parameters had the greatest effect on this capability.

This preliminary study served as a means to demonstrate that a small volume of gas could cause meaningful pressure reduction in a system with conditions comparable to *in vivo*. The DWSG prototypes were built to allow the amount of gas and the inner wall properties to be changed easily, while the outer wall remained unchanged as an essentially rigid boundary. Although standard stent-grafts are not completely rigid, we used a rigid outer wall to isolate and quantify the effect of the gas compression in the DWSG prototypes. Any additional benefit from a more compliant outer wall would depend on compliance of the native aorta within which the device is placed.

Results from this preliminary study have encouraged us to proceed with designing a more realistic DWSG prototype that can be tested within *ex vivo* cadaveric models and in animal models. Moving forward with development of the DWSG, we will need to address a handful of design challenges. The material selected for the inner wall must be highly impermeable to CO_2, to prevent reduced performance of the DWSG due to gradual diffusion of the gas layer. The results of our preliminary work have shown that the mechanical properties of the inner wall have little effect on the behavior of the DWSG, as long as the wall is flexible enough to transmit lumenal pressure to

the gas. This finding means that the wall material can be optimized to minimize gas exchange. To further address the potential for gas leakage, the final design will incorporate several independent gas pockets, such that the gas layer resembles bubble wrap or closed-cell foam. Though this compartmentalization will reduce the amount of gas that can be contained for a given reduction in lumenal area, it will ensure that puncture or leakage from one region will not disable the entire system. Dynamic flow simulations will be conducted to find a configuration of gas pockets that causes the least flow disturbance.

Another uncertainty is how the DWSG will be deployed percutaneously through a catheter of similar diameter to those used with current stent-graft systems. To crimp the DWSG to a small enough size, the gas will need to be added after deployment in the aorta. Strategies for remote inflation will be drawn from existing products such as the Nellix EndoVascular Aneurysm Sealing System [141] and other devices that are filled with fluid percutaneously and then disconnected from the filling system.

3.8.2 DWSG Capacitance and Resistance

The only design parameter in this study that was found to affect the DWSG capacitance significantly was the amount of gas loaded into the space between the inner and outer walls. As expected, a larger gas charge led to larger capacitance values but also higher flow resistance. The DWSG resistance remained several orders of magnitude below the resistance of the peripheral vasculature up to a charge of about 60 mL, at which point the inner wall of some of the prototypes had completely collapsed and would not allow sufficient flow to pass through. This behavior was more severe in cases where the inner wall was stretched to only 5%, indicating that stiffness of the inner wall material will be an important parameter to investigate further. The FE model, which successfully captured the behavior of the DWSG prototypes at gas charges up to 40mL, will be an important tool that can be used to further investigate the design space as it relates to capacitance and resistance measurements.

3.8.3 Pressure Reduction with the DWSG

Flow loop testing and the Windkessel model both showed that the DWSG led to reduced pressure compared to a rigid stent-graft. Inner wall diameter and prestretch did not significantly affect this behavior, whereas both peak and pulse pressure decreased linearly with increased gas charge. This behavior was apparent in **Figure 3.9B-E** and was confirmed by analyzing the coefficients of a linear model. The increase in flow resistance caused by the narrowed lumen of the DWSG did not appear to affect pressure even at high gas charge in the flow loop, suggesting that the benefit of increased capacitance outweighs the adverse effect of decreased flow area. Although the flow loop was designed to mimic the arterial system, some limitations of this system were a simplified inflow waveform, nonlinear peripheral resistance, and use of water as a working fluid. Although these were limitations in the physical flow loop model, they did not apply to simulations done with the Windkessel model. One concern with using water for the dynamic experiments was that flow resistance from the narrowed DWSG lumen would be underpredicted in comparison to the physiologic case where higher viscosity blood would flow through the same area. In the Windkessel model, with the fluid given blood viscosity, we still observed a trend of decreasing peak and pulse pressures as gas charge increased. The magnitude of pressure reduction in the Windkessel model was attenuated compared to the experimental results; this attenuation could be explained if the pressure decrease from DWSG capacitance was being more strongly counteracted by the pressure increase due to DWSG resistance.

The physiologic Windkessel model, with DWSG parameters set from the flow loop experiments, predicted a less substantial pressure reduction than was seen in the flow loop. This diminished effect could be explained by the higher fluid viscosity in this model, as described above, or by the significant compliance that the native arterial system has outside of the stented region. Consistent with that explanation, a simulated hypertensive patient saw greater benefit from the DWSG because the descending aorta contributed more to the overall capacitance and constituted a

greater loss when made rigid via stenting. In both the hypertensive and normotensive simulated patients, a 15 cm DWSG was not able to restore pressure to unstented values, but this was in a model with a compliant proximal aortic arch and a stented descending aortic segment. We suspect that for a patient with pathology resulting in significantly diminished native aortic compliance, approaching the characteristics of the rigid outer graft, the DWSG may show actual improvement in hemodynamics. It is worth noting that even a 10 mmHg reduction in systolic pressure has been shown to decrease the risk of cardiovascular disease by 20% [111].

There is preliminary evidence that the DWSG could improve cardiovascular outcomes over standard stent-grafts, but our next step is to gain a deeper understanding of the hemodynamic effect that the DWSG has in patients with a range of aortic properties. We saw that the narrowed lumen of the DWSG introduced negligible flow resistance into the system, but local flow behavior (turbulence, stagnation zones, wall shear stress) at the DWSG-aorta interface could not be characterized through the methods in this study. Development of a fluid-structure interaction (FSI) model will give us the opportunity to evaluate different DWSG configurations in models with various physiologic flow conditions, vessel stiffnesses, and aortic geometries. A challenge with the FSI model is that the gas layer, contained by the flexible inner wall, introduces both another fluid phase and the need for membrane physics in the simulation. We are currently working to create a solid analog to capture the DWSG behavior to make the simulations less complex. With information from the present study and future hemodynamic analyses, we will be able to identify the patient parameters (including stent-graft location, vessel compliance, peripheral vascular resistance, etc.) that are best suited to benefit from the DWSG design.

Chapter 4

Effect of the Double-Walled Stent-Graft on Pulse Wave Velocity

Portions of the computational work in this chapter were previously presented at the *2020 Summer Biomechanics, Bioengineering, and Biotransport Conference*. Portions of the experimental work were published in the proceedings for the *2020 Design of Medical Devices Conference* [142].

4.1 Introduction

The aorta, which provides the bulk of the arterial compliance, increases in stiffness by about 40% in the thoracic region from age 40 to 60 years and continues to stiffen with aging [30]. Aortic stiffening contributes to major cardiovascular complications, including stroke, kidney failure, and heart failure [32,143]. In clinical practice, pulse wave velocity (PWV), measured by the time delay between pressure waveform measurements taken at two locations in the patient's vasculature, is a well-established surrogate for estimation of arterial compliance [86,126]. Lower PWV is associated with a more compliant arterial system based on the Moens-Korteweg equation for wave speed in a compliant tube. Despite its predictive power and potential for noninvasive measurement via PWV, arterial stiffness is not typically monitored or directly treated in the United States [143].

In addition to stiffening due to age-related changes in aortic properties, the effective stiffness of the aorta increases when a stent-graft (SG) is placed. Aortic SGs are used to treat injuries such as aneurysm or dissection, but a growing body of research shows that they also lead to faster pulse wave propagation and increased systolic blood pressure [86–88]. It is likely that these changes are linked to the high rate of re-tears seen in patients who receive SG repair for aortic dissection,

especially because 50-75% of these patients have pre-existing hypertension prior to intervention [90,144].

In this work, we measured PWV in computer-simulated and experimental models of the aorta with a novel double-walled stent-graft (DWSG) [119] placed in the descending thoracic segment; the effect of the DWSG was evaluated by making the same measurements with a standard SG and an unstented aorta. The concept of the DWSG is that it restores compliance to the aorta through volume change of a compressible gas layer. The gas layer, contained by a thin, flexible membrane, lines the inner wall of a standard, stiff SG. Over the cardiac cycle, fluctuation in blood pressure causes the gas to compress and expand, providing the same benefit as dilation and contraction of a healthy vessel wall. Compared to a standard SG, the DWSG is expected to increase effective arterial compliance and lead to lower PWV measurements. Although the highly compressible gas in the DWSG will act to reduce overall wave speed, this effect may be counteracted by reflections due to the narrowed lumen of the DWSG, causing the apparent PWV to be higher than in the unstented aorta. We hypothesized that the DWSG would lower PWV compared to a rigid stent-graft, but that the resulting PWV would not be as low as in the unstented model.

4.2 Computational Methods

4.2.1 Computational Model

A 2D axisymmetric finite-element model of the descending and abdominal aorta was developed in COMSOL Multiphysics (**Fig. 4.1**). For simplicity, the aorta was given a constant radius of 13.6mm and wall thickness of 2mm. A fully coupled fluid-structure interaction (FSI) problem was set up, wherein movement of the blood would cause deformations in the vessel wall, and those deformations would likewise influence blood flow. The blood was modeled as a Newtonian fluid with dynamic viscosity of 3.5 cP. The aortic wall was modeled as an isotropic Neo-Hookean material with Lamé parameter $\mu = 0.3\ MPa$ and bulk modulus $\kappa = 150\ MPa$. Although the aorta is known to have orthotropic, nonlinear mechanical properties [145], the isotropic Neo-Hookean

model was deemed acceptable for comparisons between the unstented and stented in this study. The interface between the fluid and solid was solved using a fully coupled approach.

4.2.2 Stent-graft Properties

The DWSG consists of a standard SG as the outer wall, a flexible membrane as the inner wall, and a confined gas between the two walls. Incorporation of this full design into the FSI model would have introduced interaction with another fluid phase, making the problem computationally intractable with currently available tools. Instead, a solid material analog was modeled to represent the DWSG gas layer, such that the blood was the only fluid phase. The standard SG was modeled as a 15 cm long cylindrical tube with 0.9 mm wall thickness and linear elastic properties given by Pasta et al. [146] This SG model was also used in the DWSG, where it represented the outer wall of the DWSG. The solid analog of the gas layer was attached to the inner wall of the SG so that nodes at the interface were merged.

To define the solid analog for the gas layer, the DWSG was first modeled separately in a static, axisymmetric domain with membrane elements to represent the flexible inner wall. The pressure-volume behavior of the DWSG with a 40 mL gas charge (volume at atmospheric pressure and 20˚C) was obtained from this model. Next, the shape of the deformed membrane was imported into a second axisymmetric simulation, and the membrane was converted into a solid domain representing the DWSG gas layer (**Fig. 4.3A**). This solid domain was assigned the Storakers material model, which was originally developed to describe highly porous rubbers and foams [147,148]. Equation 4.1 gives the strain energy density function W for the Storakers model,

$$W = \sum_{k=1}^{N} \frac{2\mu_k}{\alpha_k^2}\left[\lambda_1^{\alpha_k} + \lambda_2^{\alpha_k} + \lambda_3^{\alpha_k} - 3 + \frac{1}{\beta_k}\left(J^{-\alpha_k\beta_k - 1}\right)\right] \tag{4.1}$$

where λ_i is the stretch in dimension i ($i = 1,2,3$), $J = \lambda_1\lambda_2\lambda_3$ is the volume ratio, and β_k, α_k, and shear modulus μ_k are material parameters. The parameters of the Storakers material were tuned to most closely match the pressure-volume behavior of the true DWSG system. Finally, the solid

geometry of the gas layer was imported into the FSI model, where it was placed in the descending thoracic aorta within the standard SG.

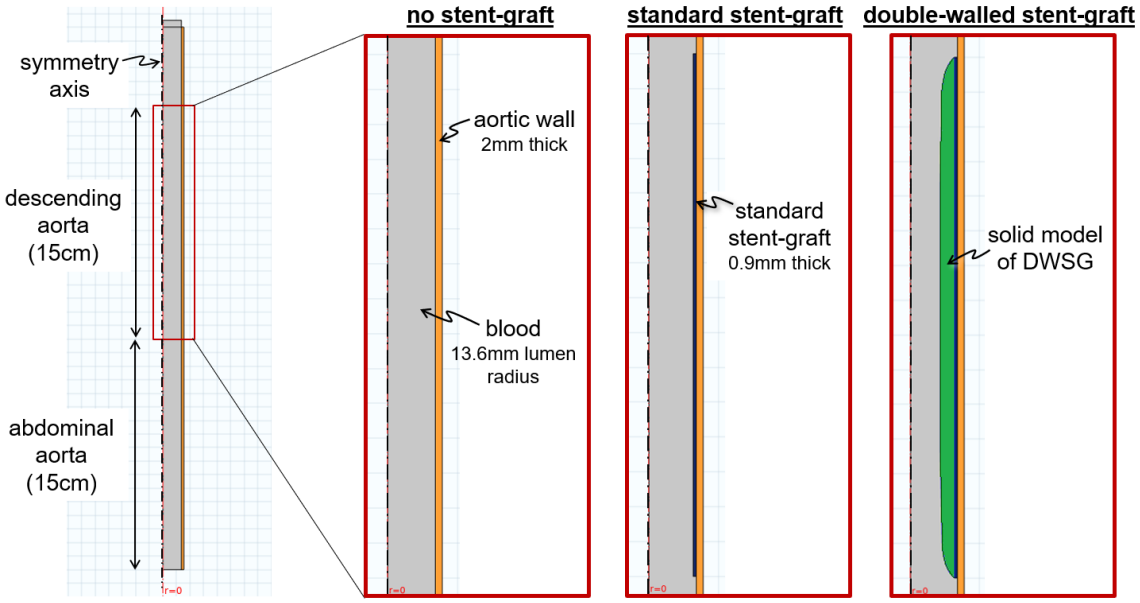


Figure 4.1: FSI model configuration. Full axisymmetric model domain shown on the left, with the three variants of the model shown in the panels on the right. Each subsequent model builds on the previous one.

4.2.3 Boundary Conditions

A prescribed volumetric flow rate, reported by Cuomo et al. [30] for the descending aorta, was applied at the inlet of the model. A linear resistance of $1.75\ \mathrm{mmHg \cdot s/mL}$ was applied at the outlet, consistent with typical Windkessel representation of the peripheral vascular resistance [109]. The pressure downstream of the resistance was set to venous pressure of 5 mmHg. A nonslip boundary condition was enforced for the fluid at the wall. Both the fluid and solid meshes were fixed at the inlet and outlet. A linear spring foundation was applied to the outer wall of the solid domain, with a spring constant of $k_A = 1.3\ MPa/m$ and a viscous dampening coefficient of $d_A = 10\ kPa \cdot s/m$ [30]. Inlet and outlet conditions were ramped up over a period of 0.5 seconds to improve stability of the simulation.

4.2.4 Study Design

The FSI model was run in three different configurations: (1) with the aorta only, (2) with a standard SG in the descending aorta, and (3) with the DWSG in the descending aorta. For each case, the simulation was run for 8 seconds of simulated time to allow the boundary conditions to ramp to full magnitude and then ensure that the system reached a steady periodic state. After the ramping interval, the system was evaluated at time increments of 0.005 seconds to facilitate precise measurement of the time delay between pressure waves at the inlet and outlet of the model. Measurements of PWV were taken by dividing the axial length of the model by the time delay in the foot of the pressure waves. Each 8 second simulation generated 5 steady state cycles, allowing the foot-to-foot time delay to be averaged over these five cycles. Similarly, the pulse pressure at the inlet of the system was calculated and averaged over the five cycles. Paired t-tests were conducted to compare PWV and pressure results between the standard SG and DWSG cases.

4.3 Experimental Methods

An experimental model of the arterial system was developed to facilitate measurement of PWV with (1) no SG, (2) a standard SG, and (3) the new DWSG prototype. PWV was measured for each case over a range of flow rates and system pressures to identify the relative performance of the DWSG across many conditions. To complete this study, the bulky PVC-based DWSG prototype used in Chapter 3 was refined for intralumenal placement in compliant tubing.

4.3.1 Stent-graft Prototypes

The DWSG fundamentally must consist of (1) a stiff outer tube that pushes against the vessel wall and (2) an inner pouch that houses several milliliters of gas and readily deforms with fluctuating arterial pressure. In the first DWSG prototype, the outer wall was constructed from a thick plastic tube, which readily supported the compressive load imposed by a prestretched elastic tube to form a sealed chamber for the gas layer. A more realistic outer wall, which must be very

thin and flexible to accommodate deployment in varied aortic anatomy, will have very low compressive stiffness and cannot be expected to support a stretched inner wall. Instead, the gas layer must be designed as an independent entity that applies minimal loading to the outer wall. For this study, a sheet of bubble wrap was employed as the gas layer (**Fig. 4.2B-E**). Although it did not provide optimal packing of gas over the given surface area, the bubble wrap offered reliable gas containment and enabled standardized production of duplicate prototypes. By measuring the dimensions of the individual bubbles, the total volume of gas at atmospheric pressure could be estimated. The 15 cm long devices with diameter of 2.54 cm (1") were found to have approximately 30 mL of contained gas.

For the outer wall of the DWSG, polypropylene tubing with 0.1 mm wall thickness and 2.54 cm inner diameter was used. The tubing was radially reinforced at both ends with crimped rings of steel wire (**Fig. 4.2 B**). The bubble wrap was placed along the inner wall of the polypropylene tubing and fixed in place with double-sided tape. The wire-reinforced polypropylene tubing without the bubble wrap represented the standard SG case.

4.3.2 Flow Loop System

The model was developed to resemble the aorta and its surrounding arterial vasculature, with the primary goal of having enough compliance to facilitate PWV calculations from foot-to-foot pressure time delay. To maximize the time delay between inlet and outlet pressures, the system consisted of a long segment of compliant tubing with pressure sensors mounted upstream and downstream (Validyne) (**Fig. 4.2A**). A pulsatile flow pump (EnvivoPC) delivered controlled flow profiles, which were measured with turbine flowmeters (Gems Sensors). A latex U-bend tube was mounted between the upstream pressure sensor and the long compliant tubing segment to minimize the footprint of the system while providing additional distance of compliant tubing between the pressure probes. A needle valve distal to the downstream pressure tap was tuned to represent the high-resistance peripheral vasculature.

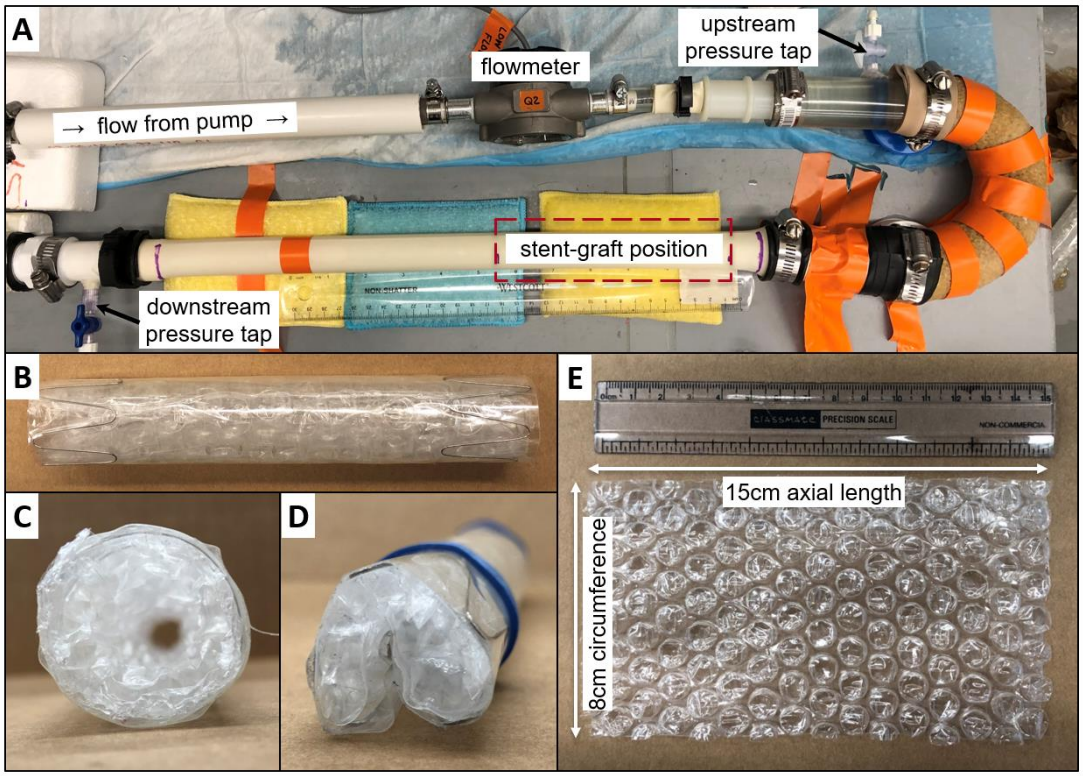


Figure 4.2: Flow loop and DWSG prototype for PWV measurement. (A) Photo of flow loop with latex tubing in descending and abdominal aortic positions. (B) DWSG prototype used for this experiment. (C) View along axis of DWSG prototype with bubble wrap lining the inner wall. (D) Prototype "crimped down" with rubber bands for deployment into the flow loop. (E) Bubble wrap sheet used as gas layer in this prototype model, with measurements taken to approximate the total amount of gas in the bubbles.

Two different materials were tested for the linear compliant tube representing the descending thoracic and abdominal aorta. A double layer of latex 2.54 cm (1") diameter penrose drains was first chosen to match the stiffness of the aorta (~100 kPa), and the tubing was prestretched by 20% in the flow loop to mimic axial aortic prestretch [149]. After axial stretch, the penrose tubing spanned 40.6 cm (16"). This setup was used for a limited series of tests due to difficulty deploying the SG prototypes along the fragile, high-friction latex tubing walls. Both stent-graft models were deployed into the proximal penrose tubing by disconnecting the tubing from the PVC connector, manually collapsing and then re-expanding when in position (**Fig. 4.2D**), and then reattaching the tubing to the flow path.

The latex tubing was replaced with butyl rubber tubing of the same diameter and length for a more extensive series of tests. This tubing was harder and less tacky, leading to easier prototype deployment. However, it was about twice as stiff as the latex tubing, leading to supra-physiologic PWV measurements and smaller time delay between the pressure sensors.

4.3.3 Study Design

Each case (no stent-graft, rigid stent-graft, and DWSG) was tested at several different flow rates in order to collect data at different mean pressures without changing the system setup. Mean pressure was expected to affect PWV due to the nonlinear behavior of the materials. Pulse rate of the pulsatile flow was swept from 40 to 60 beats per minute, and stroke volume was swept from 15 to 45 mL. The sequence of no SG, SG, and DWSG was randomized for each flow rate. After each system re-assembly, air was purged, and pressure was stabilized for at least 30 seconds before measurements were collected. Pressure and flow data were recorded via a DAQ with a sampling frequency of 25kHz for 20 seconds in each configuration. The time delay between pressure waves was found by manually marking the foot of each cycle and taking the average delay over all cycles. Photos of the system were taken to allow precise measurement of the path length between pressure sensors using the ImageJ software [137]. PWV was calculated as the path length divided by the time delay. The 95% confidence intervals for each PWV result were calculated by propagating the uncertainty of the time delay measurements.

4.4 FSI Results

4.4.1 Approximated DWSG Properties

The membrane-gas model had a linear pressure-volume relationship, as dictated by the ideal gas law for an isothermal system. In order to match the pressure-volume behavior of the DWSG in a physiologic pressure range, the solid model needed to have a different zero-pressure geometry than the membrane-gas model. Specifically, to match the behavior of the 40 mL gas layer, the solid

model had a zero-pressure volume of 38.6 mL. Between 50-175 mmHg lumen pressure, a Storakers solid model (Eq. 4.1) matched the behavior of the gas layer very closely (**Fig. 4.3B**). This fit was achieved with $N = 2$ and the parameters listed in Table 4.1.

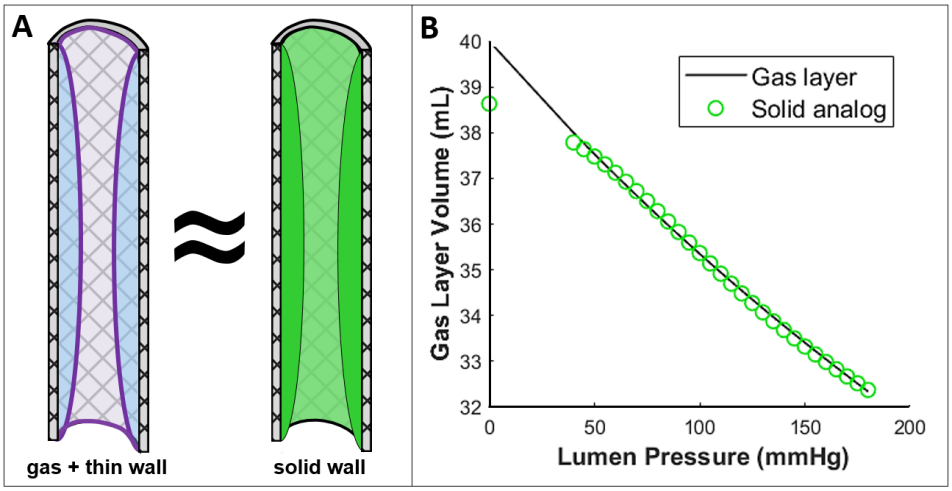


Figure 4.3: Approximating the DWSG gas layer as a solid. (A) Pictorial representation of the solid approximation. The combination of the gas volume and the thin wall containing the gas is instead modeled as a single solid volume to simplify the computational problem. (B) Comparison of pressure-volume behavior of the actual gas layer and the solid-analog model that uses a Storakers hyperelastic material model.

Table 4.1: Storakers model parameters for the gas layer solid analog

k	Shear modulus, μ_k (kPa)	Alpha parameter, α_k	Beta parameter, β_k
1	72	40	0.12
2	30	11	0.05

4.4.2 Pulse Wave Velocity and Blood Pressure

The PWV results for the three cases are shown in **Fig. 4.4A**. The horizontal dashed line at $10\ \mathrm{m/s}$ denotes a threshold set by the European Society of Cardiology, above which a patient is said to have "altered aortic function" [150]. The unstented aorta exhibited PWV of $10.3 \pm 0.3\ \mathrm{m/s}$ (mean ± 95% CI), which is slightly above the healthy threshold but well within the reported physiologic range for carotid-femoral PWV measurements ($3.8 - 16.3\ \mathrm{m/s}$) [26]. As predicted, PWV was higher with the standard SG, measuring $2.8\ \mathrm{m/s}$ faster than the unstented case, but still

within the normally reported range. The DWSG resulted in a PWV value between the unstented and standard SG, at $11.2 \pm 0.2\ \mathrm{m/s}$. A similar trend was seen in both the systolic and pulse pressure measurements (**Fig. 4.4B**) The unstented model had the lowest measurements for both pressure metrics, the standard SG had the highest, and the DWSG caused significant pressure reduction but maintained values above the unstented case. Uncertainty in the PWV measurements was the result of the simulation time step not consistently capturing the exact moment that the foot of each pressure wave occurs. The average time delay measured in the SG case was 0.033 seconds, which is less than an order of magnitude larger than the 0.005 second timestep.

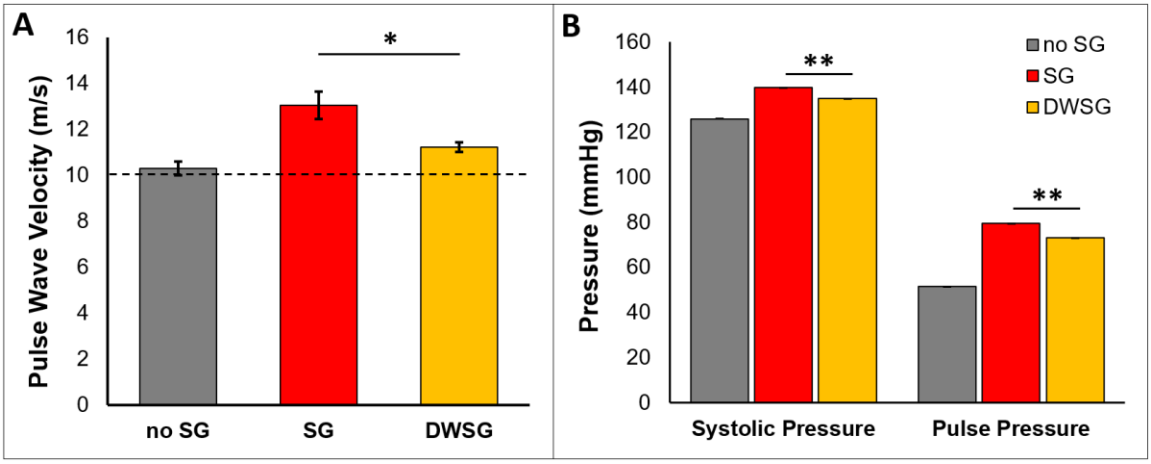


Figure 4.4: PWV and pressure FSI results. (A) Pulse wave velocity (PWV) measured across the aorta for the three different stent cases: no stent (no SG), standard stent-graft (SG), and the double-walled stent-graft (DWSG). (B) Systolic and pulse pressure measurements for each of the cases. ***** denotes $p = 0.0009$; ****** denotes $p < 10^{-5}$ in paired two-tail t-test. Error bars in both panels show 95% confidence interval for values measured over 5 simulated cycles.

Representative images of the DWSG model results are shown in **Figure 4.5**. Between systole and diastole, the aortic wall upstream of the SG deformed visibly, whereas the stented region exhibited minimal motion. The blood velocity increased in the stented region due to the reduced diameter, and this constriction also caused large eddies to form at the device inlet after systole. Compression of the gas layer solid analog varied over the cardiac cycle, with a maximum volume reduction of 18% during systole in the elements closest to the vessel lumen. The heterogeneous

compression across the gas layer indicates that, although the Storakers model matches bulk gas layer behavior well, the solid analog does not achieve the complete pressure transmission that would be seen in an actual gas model.

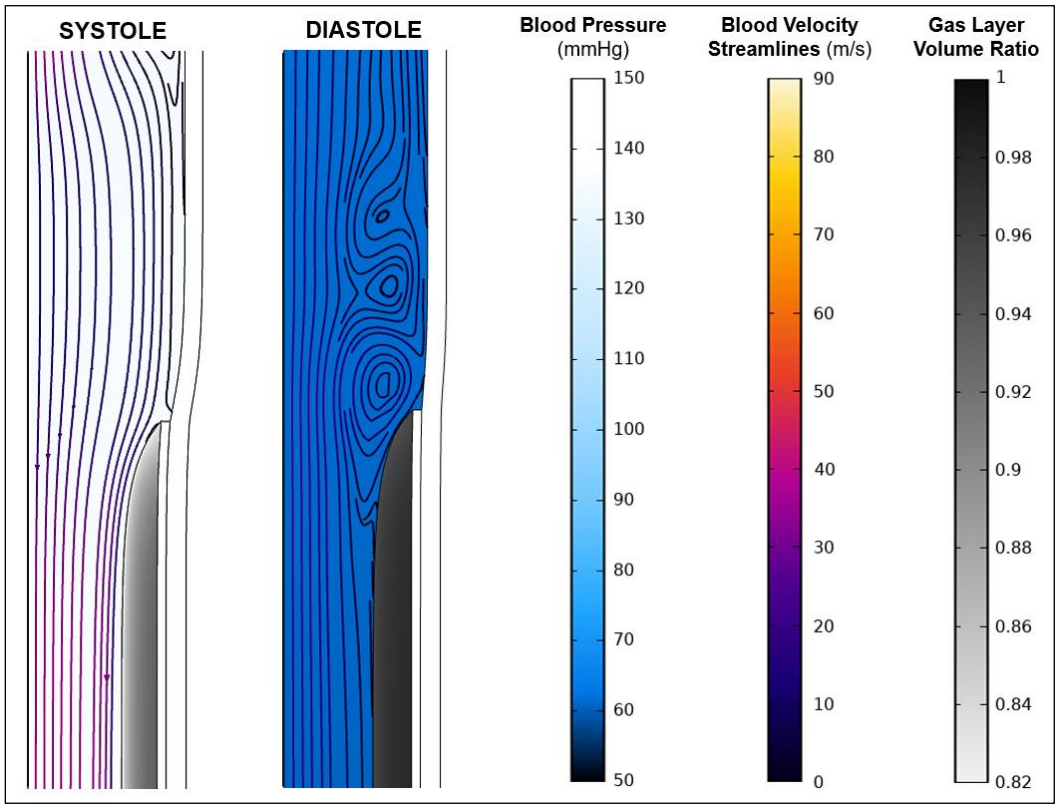


Figure 4.5: FSI flow field at DWSG inlet. Zoomed view of the axisymmetric model at the inlet of the DWSG. Blood pressure is shown through shading of the vessel lumen. Flow direction is shown with streamlines, which are colored to show velocity magnitude. Magnitude of gas layer compression is shown through shading of the solid analog. The same section of the model is shown during peak systole and diastole for comparison. Each measure – pressure, velocity, and compression – has a corresponding colorbar at the right of the figure.

4.5 Flow Loop Results

4.5.1 Pulse Wave Velocity

Average PWV measured in the latex tubing system ranged between $9.5 - 13.4$ m/s (**Fig. 4.6A,C**), whereas in the butyl tubing the values were much higher, ranging between $15.4 - 25.8$ m/s (**Fig. 4.6B,D**). In both experimental models, the standard SG exhibited the highest

average PWV compared to the other two cases, with a value of 13.4 ± 3.4 m/s (mean ± 95% CI) in the latex tubing and 25.8 ± 7.7 m/s in the butyl tubing. In the latex system, PWV for the DWSG was not statistically different from the no-stent case. In contrast, the DWSG significantly reduced PWV compared to the no-stent case when placed in the butyl tubing, changing from 22.8 ± 12.8 m/s with no stent to 15.4 ± 6.2 m/s with the DWSG ($p = 0.044$). In both systems, the DWSG had significantly lower PWV than the standard SG.

PWV in the no-stent and DWSG cases followed nearly identical trends with mean pressure in the latex tubing system, though the mean pressure in the DWSG was always 2-5 mmHg higher for the five flow rates tested. This slight increase in pressure can be explained by the higher flow resistance posed by the narrowed DWSG lumen compared to the unstented tube. With increasing mean pressure, PWV in the latex system showed a slight downward trend for each of the cases. Although the standard SG exhibited a sharp decrease in PWV between mean pressures of 40 and 50 mmHg, the uncertainty in these measurements was very high, making it unclear whether the trend may have any meaning. No such trends were apparent in the butyl system, which instead showed a slight increase in PWV for increasing mean pressure from 15 to 40 mmHg, at which point PWV appeared to be unaffected by mean pressure. These behaviors are representative of the tubing material characteristics – the latex tubing became slightly more compliant at higher pressures, while the butyl tubing maintained constant stiffness.

4.5.2 Systolic Pressure

In the latex system, systolic pressure rose linearly with mean pressure. The no-stent case exhibited the lowest systolic (**Fig. 4.7A**) until mean pressure exceeded 90 mmHg, at which point the DWSG line crossed below the no-stent line by about 1 mmHg. Because mean pressure was not precisely controlled, the points for the three different stent cases are not all taken at the same mean pressure, so it cannot be clearly concluded that the DWSG led to lower systolic pressure at these

higher mean pressures. The maximum difference in systolic pressure among the cases was observed at the lowest mean pressures; at the lowest pump setting, the no-stent case exhibited a systolic pressure of 52.9 mmHg, the standard SG showed 57.7 mmHg, and the DWSG showed 59.7 mmHg. The curves for the standard SG and the DWSG remained within 1 mmHg distance of each other across all mean pressures.

In the butyl system, systolic pressure rose more steeply with mean pressure than in the latex system (**Fig. 4.7B**). There was no clear increase or decrease in systolic pressure with either the standard SG or the DWSG compared to the no-stent case. For each pump setting, systolic pressure across the three cases never differed by more than 1-2 mmHg, suggesting that the implanted devices did not have significant impact on the systolic pressure in this system. Pulse rate of the pump did not independently cause any measurable differences in the systolic pressure.

4.5.3 Pulse Pressure

Pulse pressure trends with mean pressure diverged in the two experimental systems; with increasing mean pressure, pulse pressure decreased in the latex system (**Fig. 4.7C**) while it increased in the butyl system (**Fig. 4.7D**). In the latex system, a steep decrease in pulse pressure was observed with increasing mean pressure from 40 to 65 mmHg. From 80 to 90 mmHg mean pressure, all three stent cases exhibited an uptick in pulse pressure. The no-stent curve remained 1 to 6 mmHg below the other two curves across all mean pressures. Below 80 mmHg mean pressure, the DWSG maintained a pulse pressure slightly higher than the standard SG. At the highest pump setting, the DWSG reached a lower pulse pressure, less than 1 mmHg above the no-stent case and nearly 3 mmHg below the standard SG. Because Fig. 4.7A showed that systolic pressure in the latex system increased with mean pressure, the decrease in pulse pressure observed must be attributed to a substantial increase in diastolic pressure, especially for the lower mean pressure range where the pulse pressure drops significantly. This result is consistent with the conclusion

from Section 4.5.1 that the latex tubing decreases in stiffness, or becomes more compliant, at higher pressures.

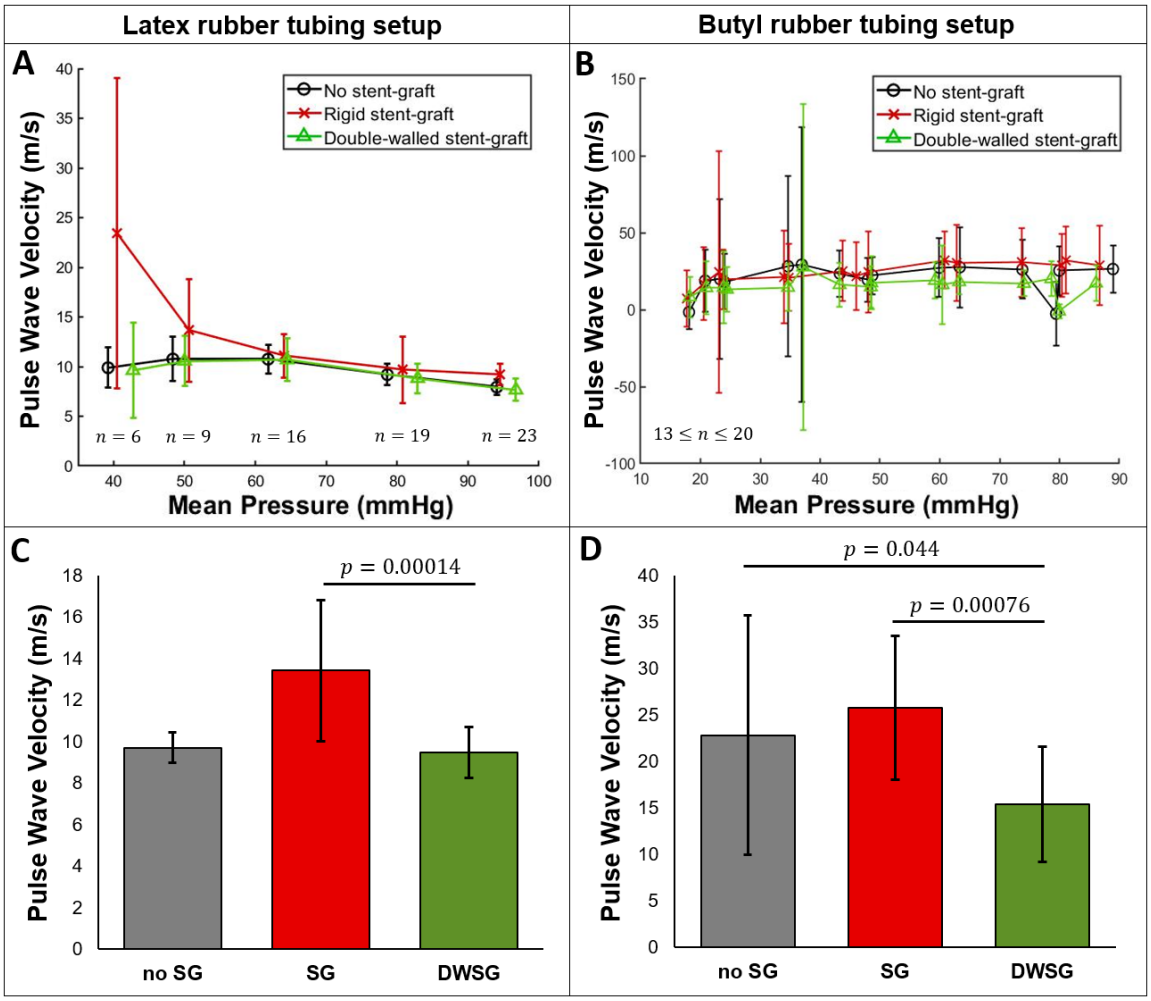


Figure 4.6: Flow loop PWV measurements. (A) Plot of pulse wave velocity as a function of mean lumenal pressure measured in the flow loop with no stent, a model stent-graft (SG), and the double-walled stent-graft (DWSG) prototype placed into latex tubing. (B) PWV for the three SG cases in the flow loop with a butyl rubber tube. (C) Data summarized from panel A, comparing mean PWV for each SG case. (D) Data summarized from panel B, comparing mean PWV for each SG case. P values for paired two-tail t-tests between the DWSG and the other two cases are shown above the corresponding bars. Error bars represent 95% confidence intervals. Values for n denote the number of cycles recorded in a given run, from which mean PWV and uncertainty were calculated.

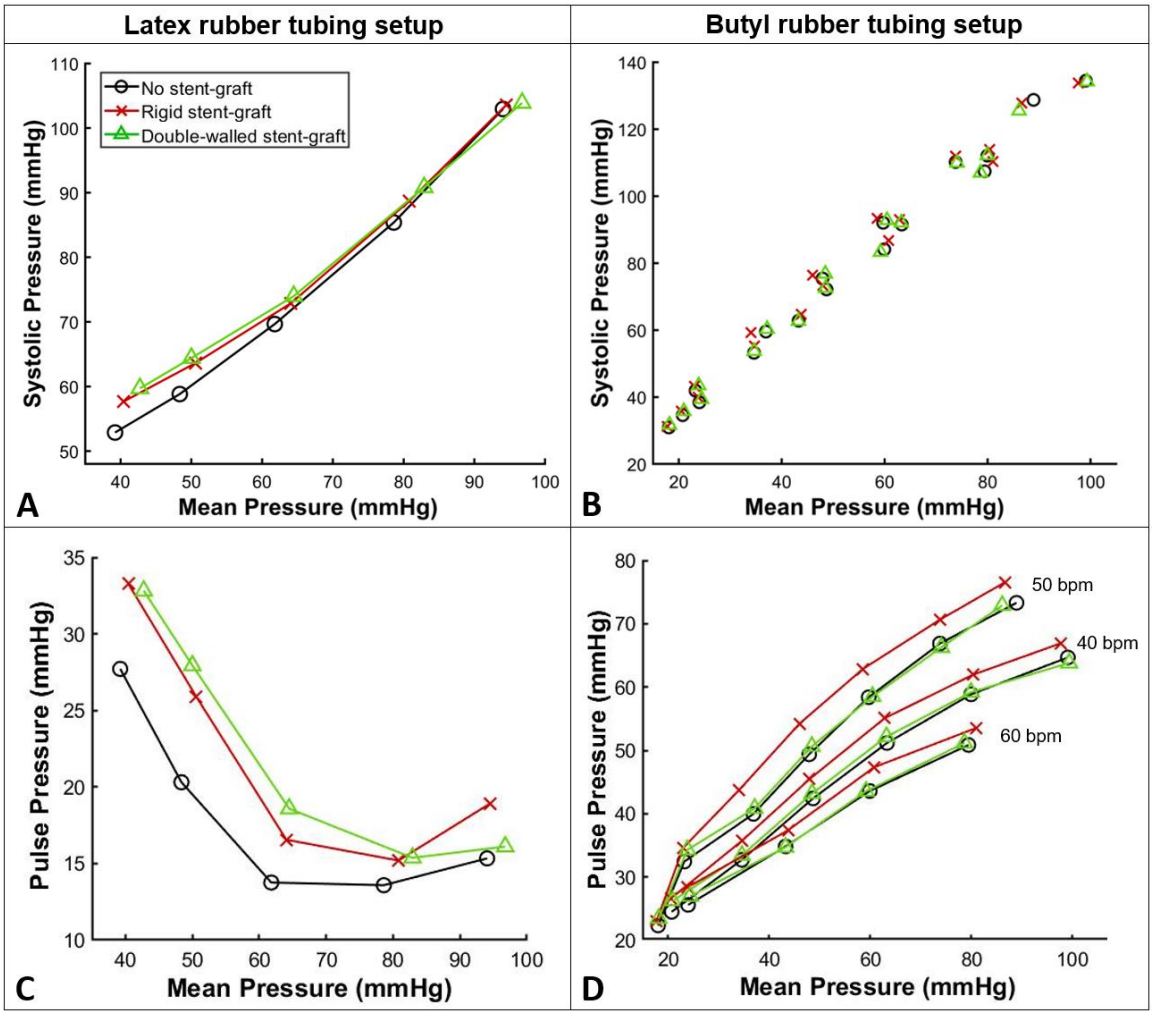


Figure 4.7: Flow loop pressure measurements. Systolic pressure measurements in the latex system (A) and the butyl system (B) for the unstented, standard SG, and DWSG cases as a function of mean pressure. Connecting lines are excluded from (B) to improve visibility of overlapping points. Pulse pressure measurements in the latex (C) and butyl (D) systems also plotted for the three cases as function of mean pressure. Pump pulse rate is noted next to groups of lines in (D) due to the noticeable impact of this parameter on the pulse pressure values. The legend in panel (A) applies to all panels.

Much like the systolic pressure results, the butyl system exhibited much steeper change in pulse pressure than the latex system across the sweep of mean pressures. Unlike the butyl systolic results, there was a clear difference in pulse pressure among the stent cases. For all pump settings, the standard SG maintained the highest pulse pressure compared to the DWSG and no-stent cases. The DWSG maintained pulse pressure measurements within 1 mmHg of the unstented case for all

runs above 30 mmHg mean pressure. The three pump settings below this threshold led to consistently higher pulse pressure in the DWSG compared to no-stent, though values still remained lower than in the standard SG. The pulse pressure measurements in the butyl system demonstrated dependence on the pump pulse rate, but no such dependence was observed for the systolic measurements or in the latex system.

4.6 Discussion

This work evaluated the effect of a novel double-walled stent-graft (DWSG) on the apparent stiffness of the aorta. PWV was measured in an FSI computational model of the descending and abdominal aorta and in two experimental flow loop models of the aorta. Comparisons were made among cases with no stent, a standard SG, and the DWSG. The standard SG resulted in the highest PWV across all models, supporting previous literature about the adverse effect SGs have on aortic stiffness [86–88]. The effective stiffness of the DWSG compared to no stent was inconsistent across the three model systems, indicating that this comparison is highly dependent on the stiffness of the native aorta. The DWSG lowered PWV beyond unstented values only in the butyl tubing system, which was about twice as stiff as a healthy aorta. In that same system, the DWSG also showed the least impact on pulse pressure, maintaining values in the same range as the unstented condition. This result supports our prediction that elderly patients, and others with a stiff aorta, will benefit most from placement of the DWSG.

The FSI model of the DWSG contained 40 mL of gas, while the experimental prototypes could only be constructed with 30 mL. The smaller amount of gas in the experimental prototypes may have contributed to the higher pressure measurements, since we established in the previous chapter that systolic and pulse pressure reduction both increase with higher gas charge. Another limitation of the experimental prototypes was the irregular inner wall surface given by the individual bubbles of the bubble wrap protruding into the lumen. The inefficient storage of gas in the bubble wrap meant that it restricted the vessel lumen even more than the FSI-simulated DWSG that contained

10 mL more of gas. The next prototype iteration will require custom-fabricated gas layers to better control the amount, distribution, and pressurization of the contained gas.

In this study, the DWSG was shown to reduce PWV, a surrogate measure for aortic stiffness, compared to a standard SG in both computational and experimental models. The observed change in PWV between the DWSG and SG cases ranged from 1.9 to 3.9 m/s in the physiologically accurate models. Studies on the effect of PWV on morbidity and mortality have shown that an increase in PWV by just 1 m/s can increase risk of cardiovascular events by 14% and all-cause mortality by 15% [35]. These statistics suggest that any improvement in PWV that the DWSG can provide over a standard device has the potential to greatly improve patient health and long-term survival.

Chapter 5

Shape Optimization of the Double-Walled Stent-Graft Gas Layer

5.1 Introduction

Diseases of the aorta are responsible for over 10,000 deaths each year in the US [151]. These diseases are typically characterized by a local defect in the aortic wall that causes propagation of a partial-thickness tear (dissection) or abnormal radial dilation of the vessel (aneurysm), either of which puts the aorta at serious risk of rupture. A common treatment for these diseases is the endovascular placement of a stent-graft (SG) to reinforce the weakened aortic wall. The SG provides passive mechanical support to prevent the pulsatile pressure wave from further damaging the native tissue. Compared to open surgical repair, endovascular treatment offers a less invasive procedure with shorter recovery time [73,74].

Although current SGs offer good short-term outcomes, there is growing evidence that the compliance mismatch between SG and native vessel may contribute to complications including new aortic tears, persistent hypertension, and pseudoaneurysm [87,152,153]. All of these complications relate back to the fact that standard SGs increase the effective stiffness of the aorta [101,131,154–156]. When a normally compliant section of the aorta is covered by a high stiffness SG, that section of the vessel loses the ability to react to the dynamic pressure load driven by the heart. Loss in aortic compliance has been shown to have serious consequences, including increased systolic hypertension and increased risk of all-cause mortality [32,143].

Most prior work on reducing compliance loss due to stent-grafting has aimed to increase SG compliance by using a more compliant material or geometry for the graft wall [157–159]. The risk with this approach is that the lower stiffness graft will undergo greater deformation and increase

transmission of the blood pressure to the dissected aortic wall or aneurysm sac. If the SG is not shielding the damaged tissue from these forces, it is not fulfilling its intended purpose. We previously proposed a double-walled SG (DWSG) (**Fig.5.1**) that aims to restore compliance in the stented area without compromising the pressure-shielding behavior of current SGs [119]. The DWSG incorporates a thin layer of biocompatible gas along the inner wall of a standard, rigid stent-graft. The gas layer changes volume in response to changing blood pressure in the aorta, mimicking the dilation and contraction of the healthy, unstented aortic wall. Increasing the amount of gas in the DWSG increases its distensibility but also reduces the available flow area in the aortic lumen, in turn potentially increasing the pressure required to push the blood through it.

Numerous optimization studies have attempted to identify the ideal design for vascular stents with objectives focusing on mechanical quantities such as stent flexibility, stiffness, recoil, radial force, and maximum strain [160–165]. Less commonly, the objectives also include hemodynamic factors such as wall shear stress, flow velocity, velocity gradient, and vorticity [162,166,167]. Prioritization of mechanical factors over hemodynamics makes sense for optimization of low-profile vascular implants, which are less likely to cause significant flow disruption than they are prone to mechanical failure or vessel damage. In contrast, shape optimization of the DWSG gas layer in the present study is focused on the tradeoff between hemodynamic disruption and device performance. Unlike standard low-profile devices, the DWSG derives its novel function from the "high-profile" gas layer. This distinct feature makes the hemodynamics a more relevant design factor than mechanical factors of the stent, which will be designed to uphold current best practices. Further complicating the design, the effect of the DWSG on hemodynamics depends on both the volume of the gas layer and the spatial distribution of that volume. In light of these challenges, advanced optimization strategies must be incorporated into the design process.

Multiobjective optimization (MOO) is a powerful tool that enables agile exploration of a given design space to identify a set of solutions that best satisfies two or more competing objectives.

Evolutionary algorithms approach MOO by generating a population of individual solutions and allowing the fittest individuals to mutate and cross over to form subsequent generations [168]. The individuals that perform as well as, or better than, all other individuals with respect to the objectives are kept as "nondominated solutions". After the specified number of evolutionary generations, the remaining nondominated solutions are said to belong to the set of Pareto-optimal solutions [169]. To efficiently investigate a diverse set of designs, objectives are typically evaluated through mathematical or computational models that simulate real-world loading and interactions. In the biomedical field, optimization studies with integrated computational models have been employed to balance thrust force versus temperature in surgical drill bits [170], to improve hemocompatibility of ventricular assist devices [171], and to tune strength, stiffness, cost, and biocompatibility of alloys for orthopedic implants [172].

We approached optimization of the gas layer shape through two independent MOO studies, which assessed changes to the 2D gas layer profile in planes aligned with and orthogonal to the direction of flow. Each profile was evaluated based on the amount of gas it stored versus its effect on simulated hemodynamic factors obtained through mathematical and computational fluid dynamics (CFD) models.

5.2 Device Design

The operating principle underlying the double-walled stent-graft (DWSG) design is that a compressible layer of biocompatible gas acts as a substitute for the compliance of the aortic wall in that region, which has been lost either due to age-related stiffening or due to intentional immobilization to protect the damaged wall from rupture (aneurysm, dissection, intramural hematoma). The outer wall of the device is a wire-reinforced stiff fabric, like a standard stent-graft, which ensures protection of the aortic wall. Lining the inner surface of the outer wall is a tubular pouch that holds the gas, forming a kind of cushion between the flowing blood and the stiff outer

stent-graft wall. The details of this gas layer – the shape, size, and modularity – are the primary topics of the present study.

In a previous study, we demonstrated in an *in vitro* flow loop that peak and pulse pressures decreased linearly with increased quantity of gas added to DWSG prototypes [119]. This effect was inhibited only at high gas volumes (79% of the total lumen volume), when the restriction in blood flow area began to contribute significant resistance to the arterial circulation. Although there was no measurable effect on pressure until high gas volumes, it is likely that abnormal flow patterns had developed around the DWSG at lower gas volumes. A successful DWSG design will be one that balances the increase in compliance with the increase in flow disruption. Assuming that the design is restricted to a cylindrical outer shape, the profile of the gas layer can be adjusted in two planes (**Fig. 5.1**) to optimize performance.

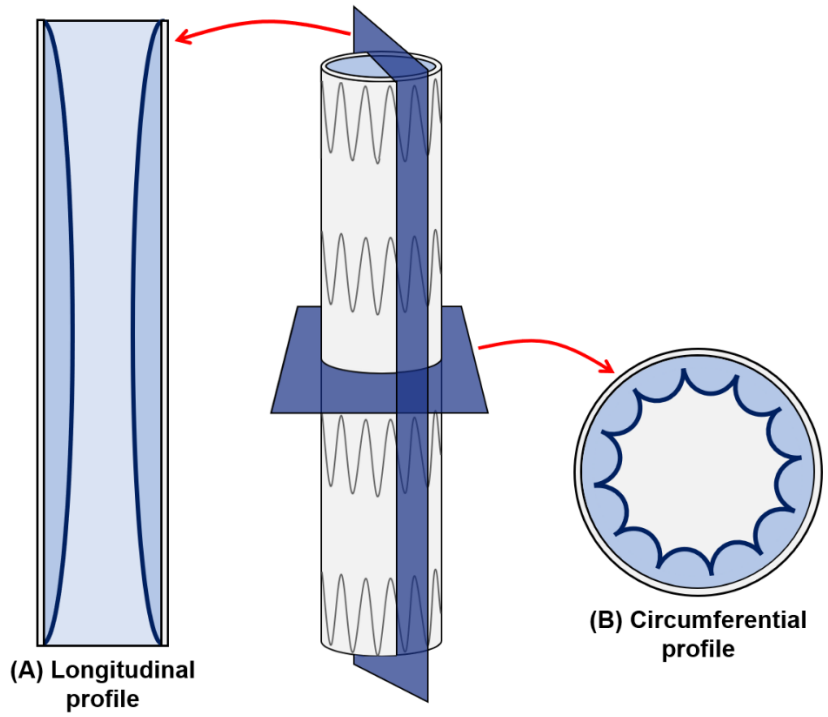


Figure 5.1: Diagram of DWSG profiles. Cross sectional cuts are taken in two different planes to show the longitudinal (A) and circumferential (B) profiles of the gas layer. The bold line in each profile represents the flexible membrane that forms the gas layer profile, and the gas itself is represented by the shaded region.

Initial prototypes of the DWSG utilized an elastic membrane to form the gas layer, meaning that pressure applied to the lumen of the device caused the membrane to deform and transfer the force to the gas. For the sake of biocompatibility and durability, the material containing the gas layer in the final DWSG product is more likely to be a stiff polymer membrane such as polyethylene terephthalate (PET) or nylon, which are used in products such as balloon catheters and intra-aortic balloon pumps. While this material should afford the DWSG a longer lifespan than a device made with highly compliant materials, the stiffness of the membrane necessitates a change in the geometry of the gas layer. In the initial design, most of the membrane wall exposed to blood flow was formed into a concave shape. If that concave wall is inextensible, it will not permit the contained gas any change in volume. This concept is best demonstrated through the example of a mylar balloon, which is much less compliant than its latex counterpart. If you apply pressure to the inflated (convex) balloon from the outside, the material buckles and the force works directly to compress the gas. If you pressurize the inside, however, where the walls inside are completely concave, all of the force puts the walls into tension and leads to very little expansion overall.

A simple way to overcome the issue of concavity is to break the single, continuous gas layer into several discrete strips that run axially and repeat around the full circumference of the device (**Fig. 5.1B**). Not only does this discretization create a series of convex segments that can be easily compressed, but it also introduces redundancy into the system, such that failure of one single segment will not lead to complete loss in device compliance. The discretization could be applied axially as well, but with the primary blood flow direction being axial, it is more important to keep the wall in that direction smooth to minimize disruption to hemodynamics. Circumferential divisions alone accomplish the goal of creating convex surfaces, so only these designs will be explored.

5.3 Design Optimization Metrics

To quantify the performance of various DWSG designs, it is necessary to identify specific parameters that characterize device compliance and flow disturbance. In the following sections, these parameters are introduced, and their acceptable ranges for this study are drawn from literature.

5.3.1 Gas Volume

The purpose of the DWSG is to increase fluid capacitance of the aorta through passive compression and expansion of the gas layer. We previously showed that capacitance of the DWSG increased linearly with increased gas volume, where the volume is defined when the gas is at atmospheric pressure [119]. This behavior was trivial to predict for static inflation of the device based on the ideal gas law, but it was found that the relationship held even in a pulsatile flow system. In the present study, we modeled the gas layer as a rigid wall and used the findings from our previous study to define capacitance of the gas layer as proportional to its volume. In other words, we aimed to maximize gas volume, which was assumed to be equivalent to maximizing DWSG capacitance.

5.3.2 Flow Resistance

While DWSG capacitance can easily be maximized by increasing the volume of the gas layer, this maximization is directly antagonized by increasing flow resistance, which eventually overwhelms any benefit gained from the capacitance. The unstented aorta contributes negligible flow resistance to the arterial system due to its large radius. Using Poiseuille's law and published values for peripheral resistance in a Windkessel model [173], it can be estimated that the resistance of the aorta can be increased by 3 orders of magnitude before it would be expected to increase the arterial resistance by 1%. Though this seems like a generous buffer, resistance goes with the negative fourth power of radius, so it is important to constrain DWSG resistance to stay within a

reasonable range. For this study, designs were considered to be valid only if they maintained Poiseuille resistance below $22.2\ \mathrm{g/cm^4/s}$, or 1% of arterial resistance distal to the descending aorta.

5.3.3 Time-Averaged Wall Shear Stress

Wall shear stress (WSS) is widely recognized as a dominant factor driving the remodeling and signaling behaviors of endothelial cells lining the inner surface of the aorta and other vessels [174]. In addition to this impact, a few studies have suggested that non-physiological WSS values, high or low, along the wall of a stent-graft are predictive of thrombogenic risk, leading to stent-graft thrombosis or micro-embolism [175–178]. Time-averaged wall shear stress (TAWSS) is a convenient metric that summarizes the WSS felt by the lumen wall over the entire cardiac cycle. Low TAWSS ($< 4\ \mathrm{dyn/cm^2}$ [175]) is associated with flow stagnation and increased atherosclerosis, while high TAWSS ($> 50\ \mathrm{dyn/cm^2}$ [179,180]) risks increased platelet activation. Both low and high TAWSS, measured along both the unstented and stented walls of the model, were considered in the optimization of the longitudinal profile.

5.3.4 Oscillatory Shear Index

TAWSS is a useful hemodynamic measure, but it only tells part of the story. Regions of the aorta or DWSG may exhibit physiologic TAWSS, but if the local direction of shear stress changes significantly over each cardiac cycle, those areas may still be predisposed to plaque formation and thrombosis [181,182]. Oscillatory shear index (OSI) is a quantitative measure of how much WSS varies from the average direction [183]. Ranging from 0 to 0.5, higher values of OSI indicate more cyclic deviation from the average WSS direction, or more oscillatory flow. Following Gallo et al. [16], we used $\mathrm{OSI_{high}} > 0.25$ as a threshold for high oscillatory flow at any point along the vessel or DWSG wall. Areas with a combination of high OSI and low TAWSS have been shown to correlate more strongly with atherosclerosis formation than those with only low TAWSS, making both parameters important to consider [184].

5.3.5 Relative Residence Time

A final flow metric considered in this study was the relative residence time (RRT). Originally proposed as a way to relate blood flow and endothelial cell permeability, RRT is positively correlated with the formation of atherosclerotic lesions [185]. Defined by Equation 5.1, RRT captures the risk of low and oscillatory flow in one measure by combining TAWSS and OSI. Given the thresholds for low TAWSS and high OSI defined in the previous two sections, a threshold for high RRT along the vessel or DWSG wall was set as $\mathrm{RRT_{high}} > 0.5\mathrm{cm}^2/\mathrm{dyn}$ [175].

$$RRT = \frac{1}{(1 - 2 \cdot OSI) \cdot TAWSS} \tag{5.1}$$

5.4 Device Models

Optimization of the DWSG gas layer design was approached with two independent models – one to address the circumferential discretization of the gas layer and another to investigate different longitudinal profiles. Details of the models are given in the following sections. Because both optimization problems require similar variables, all variables associated with the longitudinal optimization are given the superscript "ℓ" and those for the circumferential discretization optimization are given superscript "c".

*5.4.1 Longitudinal Profile (**Figure 5.2**)*

5.4.1.1 Computational Domain

A 3D axisymmetric model of the descending and abdominal aorta (**Fig. 5.2A**) was chosen to capture the effect of the DWSG on proximal and distal regions of the aorta without overburdening the computation with anatomical details that would add little information to the design comparison. The descending thoracic and abdominal aorta were modeled as a straight, tapered cylinder with the 15 cm long DWSG positioned 10cm from the inlet (**Fig. 5.2B**). The aortic arch was omitted to reduce the size of the computational domain. To further facilitate rapid iteration of the CFD

simulation within the optimization, the vessel walls were treated as rigid. As explained in Section 5.3.1, the known relationship between gas volume and capacitance in the DWSG allows us to predict the benefit of each design by measuring its volume. Volume of the gas was calculated as the difference between the volume of the unstented (cylindrical) lumen and the volume of the actual lumen in that region.

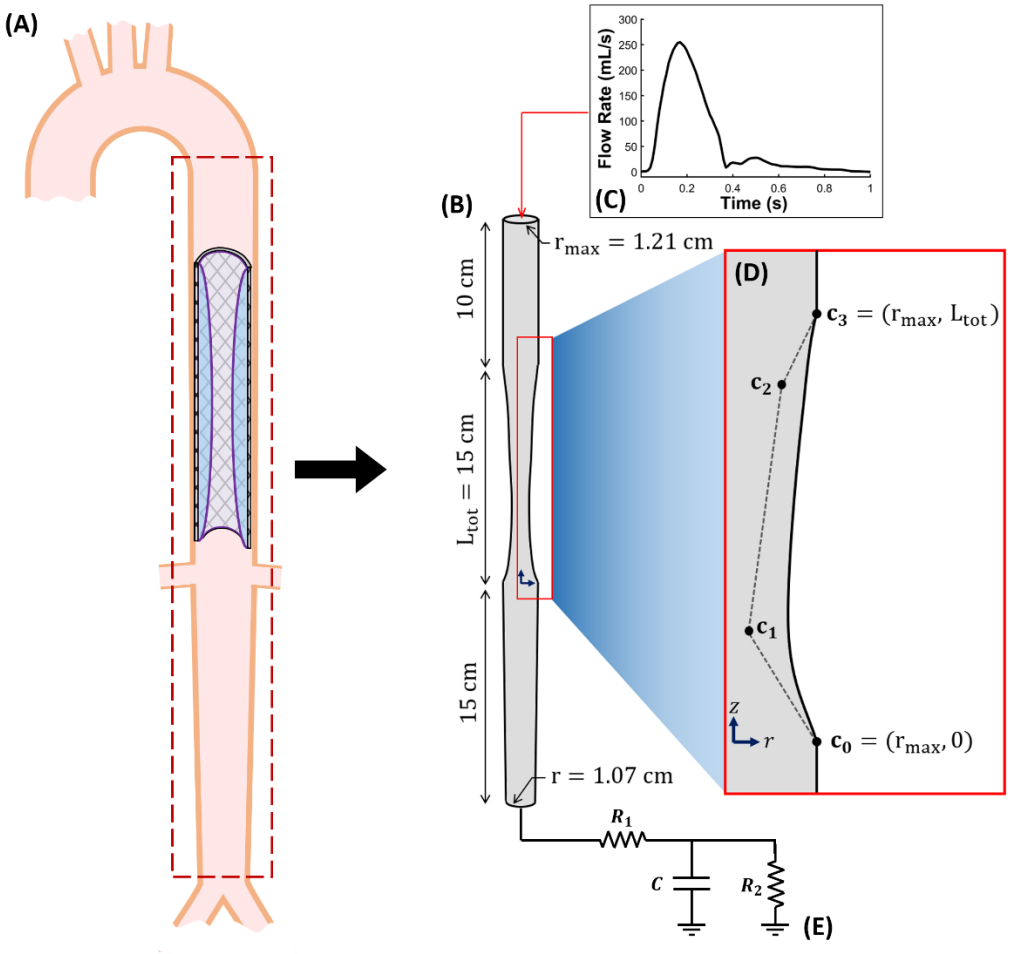


Figure 5.2: CFD model for longitudinal profile optimization. (A) Diagram of the stented aorta, with a dashed box around the region included in the CFD model. (B) Annotated example of the CFD model domain, wherein the positions of Bezier control points c_1 and c_2 (D) are the only variables modified across different simulations. This model represents the lumen of the descending and abdominal aortic segments with the DWSG placed 10cm from the inlet. A prescribed periodic flow rate (C) is applied to the inlet, and a Windkessel model (E) is applied at the outlet.

5.4.1.2 Profile Parameterization

The profile of the DWSG was defined by a third-degree Bézier curve. A third-degree Bézier curve is defined by four control points, two of which are coincident with the endpoints, which are fixed at $(0, \mathrm{r_{max}})$ and $(\mathrm{L}, \mathrm{r_{max}})$ (**Fig. 5.2D**). The remaining two control points, $c_1 = (x_1, x_2)$ and $c_2 = (x_3, x_4)$ supplied the design with four degrees of freedom, which were set as the four design variables $\vec{x}^{\ell} = \{x_1, x_2, x_3, x_4\}$ for the optimization problem. This parameterization was chosen because it always produced a smooth profile with correct endpoint locations, while allowing the shape of the profile to vary significantly. The use of a higher degree Bézier curve was considered, but the majority of the shapes permitted by the extra degrees of freedom had undesirable inflections and concavity.

5.4.1.3 Geometric Constraints

Designs were primarily evaluated based on flow characteristics calculated through CFD simulations, but a few geometric constraints also were enforced to prevent bad designs from needlessly consuming computational time. Flow resistance for each design was calculated through trapezoid rule integration of the Poiseuille equation at 150 points along the axial direction. Profiles with resistance exceeding $22.2\ \mathrm{g/cm^4/s}$ were thrown out as causing at least a 1% increase in total resistance. Volume of the DWSG lumen was calculated also using the trapezoid rule, and subsequently the gas volume was calculated. The gas volume was constrained to be a positive quantity not exceeding the volume of the bounding cylinder. The profile curve itself was constrained to lie within the bounding cylinder that represents the DWSG outer wall, so the gas layer could not have a radius larger than the vessel wall or extend axially above or below the outer wall. Self-intersection and concavity were prevented by constraining the z-values in the curve to increase monotonically.

5.4.1.4 Model Parameters and Boundary Conditions

A periodic flow rate previously measured for the descending thoracic aorta was scaled to a rate of 60 beats per minute and applied to the inlet of the domain with a plug velocity profile (**Fig. 5.2C**) [30]. At the outlet, a 1D Windkessel circuit condition was applied to represent the downstream peripheral vasculature (**Fig. 5.2E**), with pressure set to zero at the outlet of the circuit. Resistance and capacitance values were taken from Brown et al. [173]. The fluid was assigned density $1.06\ \mathrm{g/cm^3}$ and viscosity 4 cP to represent blood. Initial lumen pressure was set to $119{,}990\ \mathrm{dyn/cm^2}$ (90mmHg), a value that facilitated pressure convergence after 2 cycles.

*5.4.2 Circumferential Discretization (**Figure 5.3**)*

5.4.2.1 Domain

The model for this study represents a cross-sectional cut taken perpendicular to the axis of the DWSG at its narrowest radius. In previous prototypes, the narrowest radius was always in the middle of the length, but this may not be true for new designs developed through optimization of the longitudinal profile. The outer wall of the domain was kept constant as a circle with unit radius, after it was found that results only changed with the ratio r_{min}/r_{max}. The purpose of this model was to compare the performance of designs with different number and size of gas bubbles.

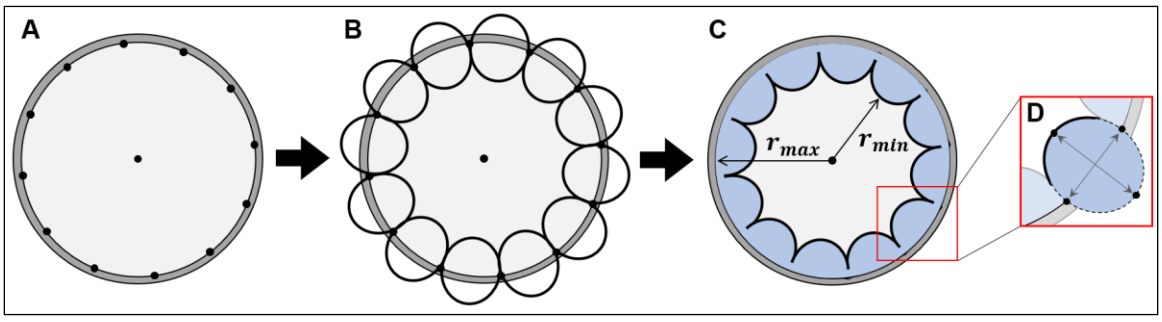


Figure 5.3: Sequence for generation of 2D axial cross section models. The cross section is formed from a series of ellipses and used for the optimization of the circumferential gas layer discretization. This example depicts a model with $n = 12$ divisions and ellipses with the long axis oriented radially. (A) Equally spaced points are generated along the lumen wall, (B) ellipses are generated with the short axis connecting adjacent points, (C) intersecting areas of the ellipses are

removed, forming a gas layer with minimum radius r_{min} and maximum radius r_{max}. (D) Diagram of a single ellipse with the removed overlapping regions shown with dashed lines.

5.4.2.2 Profile Parameterization

Each gas bubble was defined as an ellipse with its axes oriented along the radial and circumferential directions of the circular outer wall (**Fig. 5.3D**). The two design parameters selected for this model were the inner radius r_{min} and the number of gas layer segments n, such that the vector of design variables was $\vec{x}^c = \{n, r_{min}\}$. The selection of n determined the spacing of the ellipses around the outer circle (**Fig. 5.3A**). A total of n equally spaced points were identified on the circle, such that adjacent points defined one axis of an ellipse (**Fig. 5.3B**). If the distance between the adjacent points was greater than $r_{max} - r_{min}$, then the circumferential direction was the major axis, otherwise the major axis was radially oriented. After all of the ellipses were generated, represented by (x, y) coordinates with the origin of the coordinate system located at the center of the bounding circle, points outside of the circle were removed so that only semi-ellipses remained. For sets of r_{min} and n that caused adjacent ellipses to intersect each other, points in these intersecting regions were removed (**Fig. 5.3C**).

5.4.2.3 Geometric Constraints

Creation of valid geometries using this method required $n \geq 3$ and $0 < r_{min} \leq r_{max}$. Additional constraints on the design variables were established to produce more data points within the desired design space. These constraints are discussed in Section 5.5.2.2.

5.4.2.4 2D Performance Metrics

The two-dimensional construction of this model necessitated the creation of surrogate 2D measurements for the flow resistance and gas volume, which were the two objectives for this study. The main geometric quantity used to calculate resistance with Poiseuille's law is the radius. For

pipes with non-circular cross sections, like the present DWSG model, the hydraulic diameter D_{hyd} is calculated as a ratio of the lumen area A_{lumen} and perimeter P_{lumen} (Eq. 5.2).

$$D_{hyd} = \frac{4 \cdot A_{lumen}}{P_{lumen}} \tag{5.2}$$

Because resistance scales with radius to the negative fourth power, the quantity D_{hyd}^{-4} was used as the surrogate measure for flow resistance of the DWSG cross section. For gas volume, the area of the 2D gas-containing region was calculated.

5.5 Optimization Setup

5.5.1 Longitudinal Profile

A multiobjective genetic algorithm formulation was used to evaluate longitudinal profiles of the DWSG gas layer. The optimizer iteratively guessed a set of design variables, the new geometry was modeled and meshed, and a CFD simulation was run with the new mesh to evaluate the design (**Fig. 5.4**). The output from this process was the pareto front identifying nondominated solutions to the design problem.

5.5.1.1 Objectives

Optimization of the longitudinal DWSG profile was posed as a multiobjective optimization (MOO) problem to allow for *a posteriori* decisions about the tradeoffs between the objectives. Two objectives were selected to reflect the two competing goals of (1) maximizing device capacitance and (2) minimizing flow disturbance. Both objectives, $f_1^{\ell}(\vec{x}^{\ell})$ and $f_2^{\ell}(\vec{x}^{\ell})$, were formulated as quantities to minimize with $\vec{x}$ representing the vector of design variables (Eqs. 5.3-5.4).

$$f_1^{\ell}(\vec{x}^{\ell}) = V_{max} - V_{gas} \tag{5.3}$$

$$f_2^{\ell}(\vec{x}^{\ell}) = \hat{A}_{high\ RRT} = \frac{A_{RRT \geq RRT_{high}}}{A_{tot}} \tag{5.4}$$

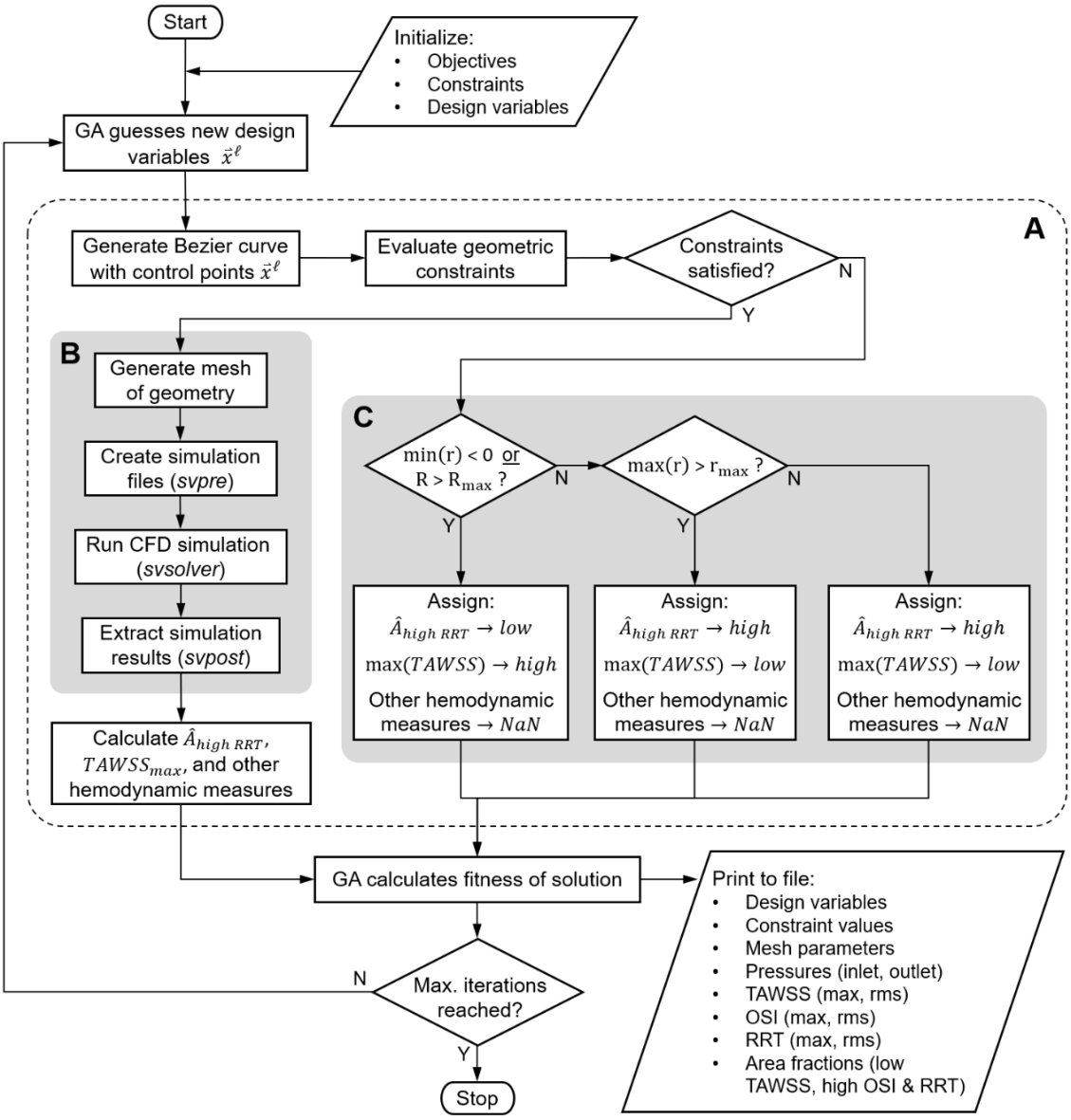


Figure 5.4: Flowchart of optimization procedure for the longitudinal profile. Problem is initialized by defining objectives, constraints, and limits for design variables $\vec{x}^{\ell}$. With each new $\vec{x}^{\ell}$, the geometric constraints are assessed first. If the constraints are satisfied, subroutine B is conducted with the SimVascular API to generate the model and execute the CFD simulation. If geometric constraints are not satisfied, subroutine C decides how to assign artificial values to feed back to the optimizer. The real (B) or artificial (C) results are fed back into the genetic algorithm (GA) to inform the next $\vec{x}^{\ell}$ until the program is complete. The dashed box (A) denotes the single function that is given to the GA to return evaluated objectives and constraints.

In $f_1^\ell(\vec{x}^\ell)$, gas volume V_{gas} is maximized by setting a target to minimize lumen volume, which is defined as the total unstented volume V_{max} minus the gas layer volume. In $f_2^\ell(\vec{x}^\ell)$, RRT was selected as the hemodynamic parameter since it combines the effects of TAWSS and OSI. Following the previously defined threshold of $\mathrm{RRT_{high}} = 0.5\ \mathrm{cm^2/dyn}$, this objective seeks to minimize fraction of the domain surface area $\hat{A}_{highRRT}$ that experiences an RRT at or above the threshold. While f_1^ℓ naturally considers only the DWSG, f_2^ℓ considers both the DWSG and the surrounding aortic wall.

5.5.1.2 Constraints

Several inequality and equality constraints were employed to improve the quality of designs obtained through the optimization. The majority of the constraints pertained to geometric limitations described in Section 2.3.1.2. One additional constraint disqualified designs that exhibited any areas with $\mathrm{TAWSS_{max}} > 50\ \mathrm{dyn/cm^2}$, based on the risk of high shear thrombosis when instantaneous shear exceeds $5000s^{-1}$ [179,180,186]. Constraints on the maximum and minimum values for $\vec{x}^\ell$ were imposed as bounds on the values that the optimizer could guess. All inequality constraints were arranged such that the target is less than or equal to zero, to satisfy the format required by the optimization algorithm. A summary of the constraints is given in **Table 5.1**. Constraints pertaining to the Bézier curve are defined in terms of the (r, z) coordinates of the curve, where r_{max} is the vessel radius that defines the cylindrical outer wall of the DWSG, L_{tot} is the length of the DWSG, R_{max} is the upper limit for flow resistance, and i is an index that ranges from 1 to N to cycle over the elements in the r and z lists.

5.5.1.3 Algorithm

The NSGA-II elitist, non-dominated sorting algorithm was employed for this optimization problem due to its ability to handle non-convex pareto fronts and preserve diversity in the population [187]. The real-coded version of the algorithm was used, meaning that the optimization

was conducted with real, non-binary values. Relatively small population sizes were chosen for this study to promote diversity and faster convergence [188,189]. Another benefit to using a small population is that more generations of the algorithm could be completed in less computational time, which was an important consideration given the high cost of the CFD simulations. Three separate runs of the optimization were conducted –with populations of 5, 8, and 12 individuals, and the results from the three runs were combined to provide as many data as possible for design analysis.

Table 5.1: List of constraints enforced for the 3D axisymmetric optimization. x_1 through x_4 are the design variables $\vec{x}^{\ell}$ that define the Bézier curve, r_{max} – inner radius of the aorta in the stented region, L_{tot} – total length of the DWSG, (r_i, z_i) – coordinates along the Bézier curve, R_{max} – maximum allowable flow resistance, $TAWSS_{max}$ – maximum allowable TAWSS.

Constraint	Description
$-0.5 \leq x_1, x_2 \leq r_{max}$	x_1 and x_2 both must lie between – 0.5 cm and r_{max}
$0 \leq x_3, x_4 \leq L_{tot}$	Values for both x_3 and x_4 must lie between 0 cm and L_{tot}
$-\min(r) \leq 0$	Smallest radius must be positive
$\max(r) - r_{max} \leq 0$	Largest radius must not exceed r_{max}
$-\min(z) \leq 0$	Smallest z position must be positive
$\max(z) - L_{tot} \leq 0$	Largest z position must not exceed L_{tot}
$-\min(z_{i+1} - z_i) \leq 0$	z coordinates must increase monotonically
$R - R_{max} \leq 0$	Resistance must not exceed R_{max}
$\max(TAWSS) - TAWSS_{max} \leq 0$	The largest value of TAWSS must not exceed $TAWSS_{max}$
$r(1) - r_{max} = 0$	First radius must be coincident with vessel wall
$r(N) - r_{max} = 0$	Final radius must be coincident with vessel wall
$z(1) = 0$	First z position must be coincident with vessel wall
$z(N) - L_{tot} = 0$	Final z position must be coincident with vessel wall

5.5.2 Circumferential Discretization

Much like the longitudinal profile, the DWSG lateral profile was assessed via MOO (**Fig. 5.5**). Each set of design variables was used to generate a 2D profile, from which the objective functions

were directly evaluated without the use of any CFD simulations. The pareto front of optimal solutions was generated from this process.

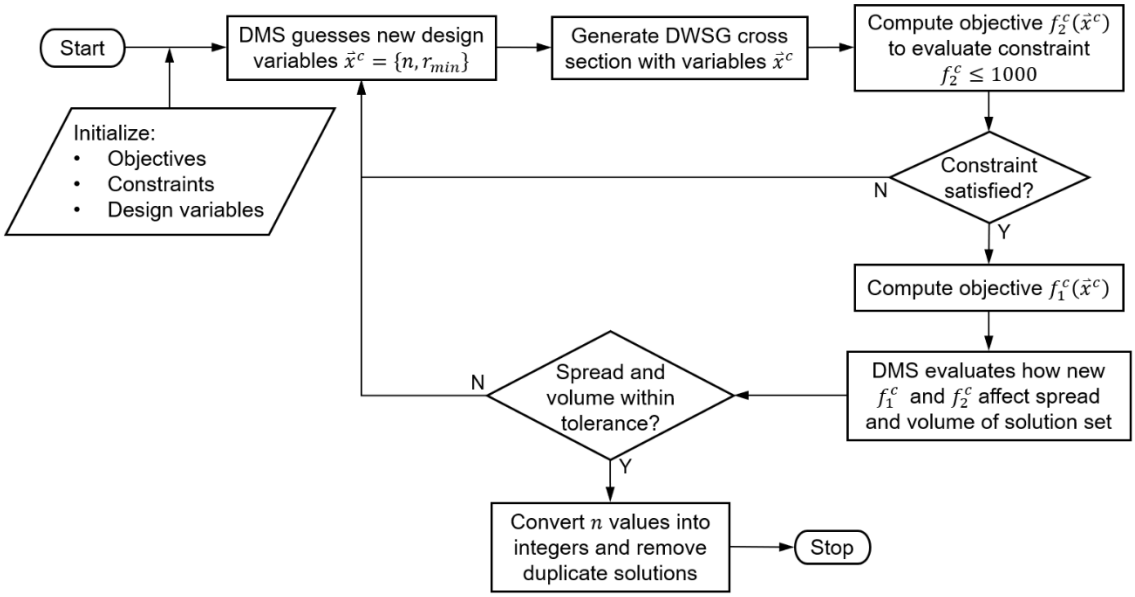


Figure 5.5: Flowchart of optimization procedure for the circumferential gas layer discretization. After initialization, the direct multisearch (DMS) algorithm guesses a new set of design variables $\vec{x}^c$. Objectives and constraints are evaluated, and the results inform the next guess. The loop is exited when the points on the pareto front are spread evenly and maximize the dominated hypervolume.

5.5.2.1 Objectives

The two objectives selected for this optimization problem represented the competing capacitance versus flow disturbance goals, both of which were computed using strictly geometric information (Eqs. 5.5 and 5.6). In Equation 5.5, gas volume is maximized through minimization of the 2D lumen cross section A_{lumen} normalized by the total possible area A_{tot}, given by the area of the circular outer wall. In Equation 6, normalized flow resistance is minimized through control of the hydraulic diameter D_{hyd} (Eq. 5.2), which relates to resistance with $R \sim 1/D_{hyd}^4$.

$$f_1^c(\vec{x}^c) = \frac{A_{lumen}}{A_{tot}} \tag{5.5}$$

$$f_2^c(\vec{x}^c) = \frac{R - R_{min}}{R_{min}} = \left(\frac{D_{max}^4}{D_{hyd}^4}\right) - 1 \tag{5.6}$$

5.5.2.2 Constraints

The geometric constraints discussed in Section 5.4.2.3 were imposed as upper and lower bounds on the design variables n and r_{min}. Trial rounds of the optimization showed that the objective function values plateaued for values of $n > 30$ (**Fig. 5.6**), so an upper bound of 30 gas layer segments was imposed to gather more data points within a meaningful range. An additional constraint was imposed, preventing $f_2^c(\vec{x}^c)$ from exceeding a value of 1000, which corresponds to the 1% change in total arterial resistance constraint imposed in the 3D optimization problem. It was also necessary to restrict n to integer values, though this constraint had to be manually enforced after the optimization completed due to limitations of the chosen algorithm, as detailed in Section 5.6.2. All constraints for this problem are summarized in **Table 5.2**.

5.5.2.3 Algorithm

A direct multisearch (DMS) approach was used for this optimization problem, which is the default MOO algorithm available in MATLAB (MathWorks) [190]. The constraints in **Table 5.2** were enforced as upper and lower bounds on the design variables, when applicable. The upper bound for f_2^c was coded as a nonlinear constraint since it couldn't be represented as a linear function of the design variables.

Table 5.2: Constraints enforced for the 2D axial cross section optimization. n – number of circumferential divisions in the gas layer, r_{min} – smallest radius for a given gas layer profile, r_{max} – inner radius of the aorta in the stented region, f_2^c – objective function defined in Equation 5.6.

Constraint	Description
$3 \leq n \leq 30$	The number of gas segments must be between 3 and 30
$0.25 \leq r_{min} \leq r_{max}$	The inner radius of the gas layer must be between 0.25 and r_{max}
$f_2^c(\vec{x}^c) - 1000 \leq 0$	Flow resistance must not increase more than 1000% from no stent
$n \in \mathbb{Z}$	The number of gas segments can only take on integer values

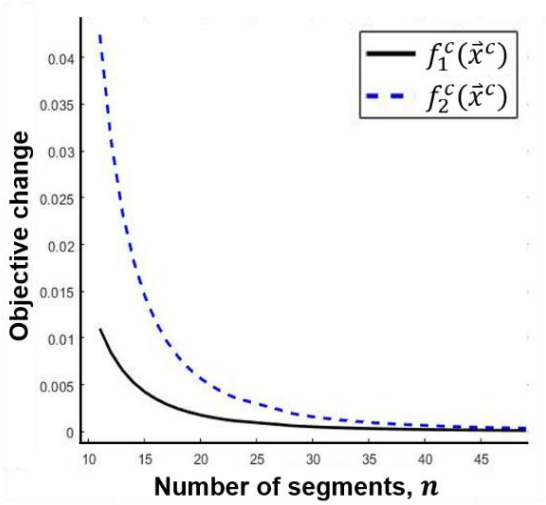


Figure 5.6: Plot of decaying change in objectives for circumferential gas layer discretization. Objectives $f_1^c(\vec{x}^c)$ and $f_2^c(\vec{x}^c)$ both converge upon a steady value as the number of segments (n) increases in the model.

5.6 Implementation

5.6.1 Longitudinal Profile

The optimization routine was implemented through the Platypus package (Version 1.0.4) [191] in Python, with the objective functions evaluated through CFD simulations set up and run using the Simvascular Python application programming interface (API) [192]. The workflow is depicted in **Figure 5.4**. The problem was initialized with Platypus as having 4 design variables, 2 objectives, and 11 constraints. Bounds for the design variables were assigned, and the program was pointed to a single function (**Fig. 5.4A**) that returned the objectives and constraints for a given input vector $\vec{x}^\ell$. Finally, the NSGA-II algorithm was specified, and the desired population size and number of iterations were assigned. For each of the population sizes, 500 iterations were run.

During each iteration of the optimization, a value for $\vec{x}^\ell$ was passed to the function that computes objectives and constraints (**Fig. 5.4A**). Within that function, a Bézier curve is first computed using the *bezier* library [193], followed by calculation of geometric constraints. If any of the constraints are not satisfied, the function immediately returns artificial objective and constraint values without running the CFD simulation. The purpose of this short circuit is twofold:

(1) running CFD only for valid geometries saves valuable computational time, and (2) running CFD on invalid geometries could cause the code to crash or return erroneous results that appear to satisfy the objectives, biasing the optimizer toward those bad variables. One downside of this approach is that the function must return false values for the objectives and constraints that were not calculated. Values used for one objective ($\hat{A}_{high\ RRT}$) and one constraint ($\max(TAWSS)$) are normally obtained from the CFD result. Depending on which geometric constraints were violated, it could be determined whether the attempted shape was too narrow (high flow resistance), too wide (exceeding r_{max}), or too irregular (nonmonotonic z values). Each of these cases was assigned artificial outputs to match the expected outcome (**Fig. 5.4C**, **Table 5.3**). This method provided the optimizer more accurate information than if a single set of values were returned for any case with unsatisfied constraints.

Table 5.3: Artificial optimization results for unmet constraints. Matrix used to generate artificial results for the 3D axisymmetric optimization problem when the given design variables did not satisfy all geometric constraints. Depending on which constraints were not met, either high or low values for area with high relative residence time, A_{RRT}, and maximum time-averaged wall shear stress, $\max(TAWSS)$, were returned to the optimizer. The $random(\text{low}, \text{high})$ function returns a random value within the specified range.

Unsatisfied Constraint(s)	Artificial A_{RRT}	Artificial $max(TAWSS)$
$\min(r) < 0$ or $R > R_{max}$	$random(0.2, 0.25)$	$TAWSS_{max} + random(10,20)$
$\max(r) > r_{max}$	$random(0.6, 0.7)$	$TAWSS_{max} - random(10,20)$
$\min(z) < 0$, $\max(z) > L_{tot}$, or $\min(z_{i+1} - z_i) < 0$	$random(0.6, 0.7)$	$TAWSS_{max} - random(10,20)$

For $\vec{x}^{\ell}$ values that satisfied the geometric constraints, commands from the Python API were executed to create contour groups for the new simulation domain and subsequently generate a tetrahedral mesh [194] (**Fig. 5.4B**). To handle failure of mesh generation, the program would attempt to create a mesh from a series of three different parameters sets loaded from text files

(**Table 5.4**). If all three attempts fail, the function returns high artificial values for the uncalculated objective and constraint to enable the next $\vec{x}^{\ell}$ guess.

Table 5.4: Mesh parameters used for each 3D axisymmetric model. If parameters from Attempt #1 failed to generate a valid mesh, meshing would be re-attempted with the next set.

Mesh Parameter	Attempt #1	Attempt #2	Attempt #3
Edge Size (cm)	0.3	0.3	0.25
Number of boundary layers	5	4	5
Boundary layer size (fraction of edge size)	0.25	0.25	0.324
Ratio of boundary layer size decrease	0.8	0.8	0.8

Following successful mesh generation, simulation files were created, and the CFD problem was solved using SimVascular's svSolver [195]. Simulations were run for 300 time steps of 0.01 seconds each to collect data for three cardiac cycles. Only values from the final cycle were used to calculate results. Default solver parameters were used, aside from the tolerance and maximum number of iterations for the solver, momentum, and continuity loops, which were adjusted according to the SimVascular documentation to improve convergence given the unsteady flow (**Table 5.5**) [196].

After each iteration, all simulation results were saved to a file along with the design variables, mesh parameters, and evaluated constraints. The optimizer continued to test design variables and create new generations of individuals until the maximum number of iterations was reached. Upon completion, the design variables and evaluated objectives comprising the pareto front were saved in a separate file.

Evaluated objectives from both optimization runs were combined into a single dataset, and the resulting pareto front was extracted using the *paretoFront()* function in MATLAB [197]. For most analyses, all objective values and other performance metrics were normalized by values obtained for the unstented domain, for which the geometry was defined by $c_1 = c_0$ and $c_2 = c_3$ (**Fig. 5.2D**).

Five designs were sampled from across the pareto front, and the CFD simulations were re-run so the flow fields could be visualized. These designs were compared using the metrics of max($TAWSS$), area fraction with high OSI ($\hat{A}_{high\ OSI}$), resistance R, and area fraction with low TAWSS ($\hat{A}_{low\ TAWSS}$). These metrics, and the objectives, were evaluated both over the full domain (denoted with no subscript) and separately in each region, denoted as proximal to the DWSG $\langle\cdot\rangle_{prox}$, within the DWSG $\langle\cdot\rangle_{DWSG}$, and distal to the DWSG $\langle\cdot\rangle_{dist}$.

Table 5.5: Parameters used to run CFD simulations with SimVascular's svSolver. Description of parameters can be found at [196]. NS stands for Navier-Stokes.

svSolver Parameter	Value
Step Construction	8
Backflow Stabilization Coefficient	0.2
Residual Criteria	0.0001
Minimum Required Iterations	3
Tolerance on Momentum Equations	0.0001
Tolerance on Continuity Equations	0.0001
Tolerance on NS Solver	0.0001
Maximum Number of Iterations for NS Solver	8
Maximum Number of Iterations for Momentum Loop	15
Maximum Number of Iterations for Continuity Loop	400

5.6.2 Circumferential Discretization

This optimization study was run using the *paretosearch()* function in MATLAB. Objective functions and constraints were evaluated with two separate MATLAB functions, which were both given as inputs to the *paretosearch()* function. The upper and lower bounds for the two design variables were given to the function as separate arrays. The "ParetoSetSize" option was set to 800, meaning that the program began with 800 random sets of design variables within the prescribed bounds and ultimately terminated with 800 points on the pareto front. During each iteration, the

design variables $\vec{x}^c$ were used to generate a 2D profile of the DWSG gas layer via the procedure described in Section 5.4.2.2. The $f_2^c \leq 1000$ constraint was evaluated to determine validity of the design variables. If the constraint was satisfied, both objective functions were evaluated and returned to the optimizer. If the constraint was not satisfied, the optimizer assigned an infinite penalty to those variables and moved on to a new set of design variables. This process repeated until the stopping criteria – adequate spacing of solutions (spread) and maximum possible distribution range (volume) – were satisfied [190,198].

Because the design variable n must be an integer whereas the design variable r_{min} is continuous, this problem is classified as mixed-integer optimization. The *paretosearch()* function cannot directly handle mixed-integer optimization, so postprocessing was done to reduce the results into valid solutions. During the optimization, the optimizer's non-integer guesses for n were rounded down to the nearest integer value before being passed to the function that generates the 2D profiles. When the optimization finished, the same rounding procedure was applied to the n that formed the pareto front solutions, and then duplicate solutions were removed. By solving for 800 points on the pareto front, this reduction process ultimately yielded 315 valid points.

5.7 Results

5.7.1 Longitudinal Profile

5.7.1.1 Evaluated Objective Space

The set of all objective evaluations that satisfied the constraints for optimization of the longitudinal gas layer profile is shown in **Fig. 5.7A**. Each point on the plot represents a CFD simulation run with a different profile. The optimization case with a starting population of 5 individuals performed the best, generating points that minimized both objectives far better than the other two population sizes. The nondominated pareto front of solutions is marked in **Fig. 5.7B**. Although only three points strictly met the criteria for the pareto front, resolution of the meshes

used to solve the CFD is not fine enough to distinguish between variability of less than 1 mL lumen volume, making all points near the pareto front worth considering.

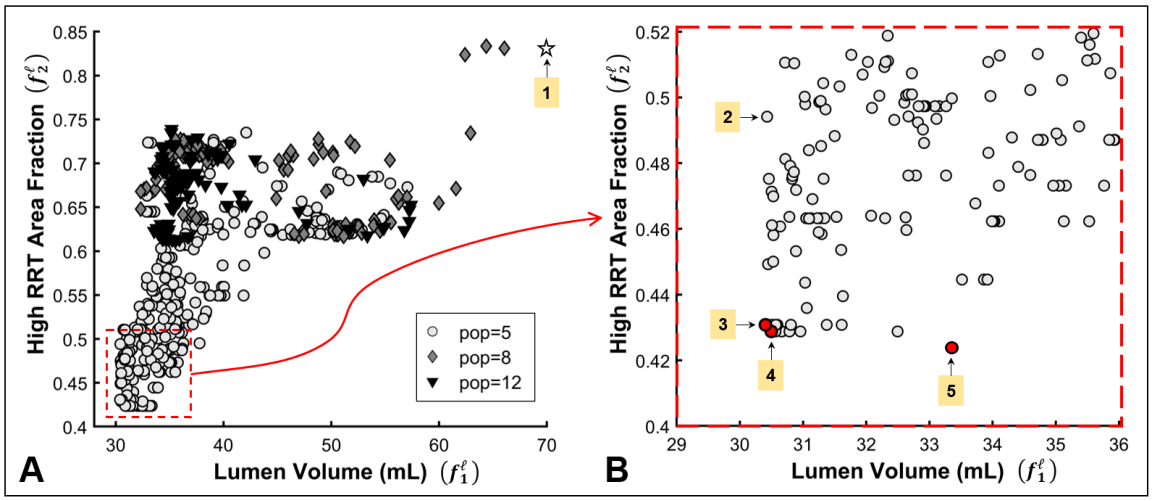


Figure 5.7: Optimization results for the longitudinal profile. (A) All valid simulation results are plotted against the two optimization objectives. The points are marked based on the population size for the genetic algorithm through which they were generated. The star (point 1) marks the results from the unstented model, which was run separately from the optimization. The dashed box identifies the area of greatest interest, where both of the objectives are best minimized. (B) Zoomed in view of the boxed area from (A), with the nondominated solutions (points 3-5) shaded darker. The numbered points correspond to simulations analyzed in greater detail in **Fig. 5.10**.

To confirm that minimization of $\hat{A}_{high\ RRT}$ was an effective way to minimize both $\hat{A}_{low\ TAWSS}$ and $\hat{A}_{high\ OSI}$ with a single objective, the trends of the latter two variables were overlaid onto the evaluated objective space. For this analysis, all variables were normalized against the values for the unstented simulation, which may be considered as the ideal hemodynamic conditions. In **Fig. 5.8A**, $\hat{A}_{low\ TAWSS}$ is shown to decrease with decreased $\hat{A}_{high\ RRT}$. The top right corner of the plot (where normalized objectives are both unity) represents the unstented case, which had overall the worst objective evaluations and also the highest area with low TAWSS. This result is consistent with the fact that any stent design will cause some lumen restriction, leading to higher velocities in the stented region and overall fewer areas with low WSS. Fig. 5.8B shows a similar behavior for $\hat{A}_{high\ OSI}$, though the magnitude of variation in this value is much smaller. Low TAWSS area had

a 60% reduction from worst to best objective values, whereas high OSI area achieved only about a 35% reduction. Neither $\hat{A}_{low\ TAWSS}$ nor $\hat{A}_{high\ OSI}$ demonstrated strong dependence on lumen volume, supporting the independence of the two chosen objectives.

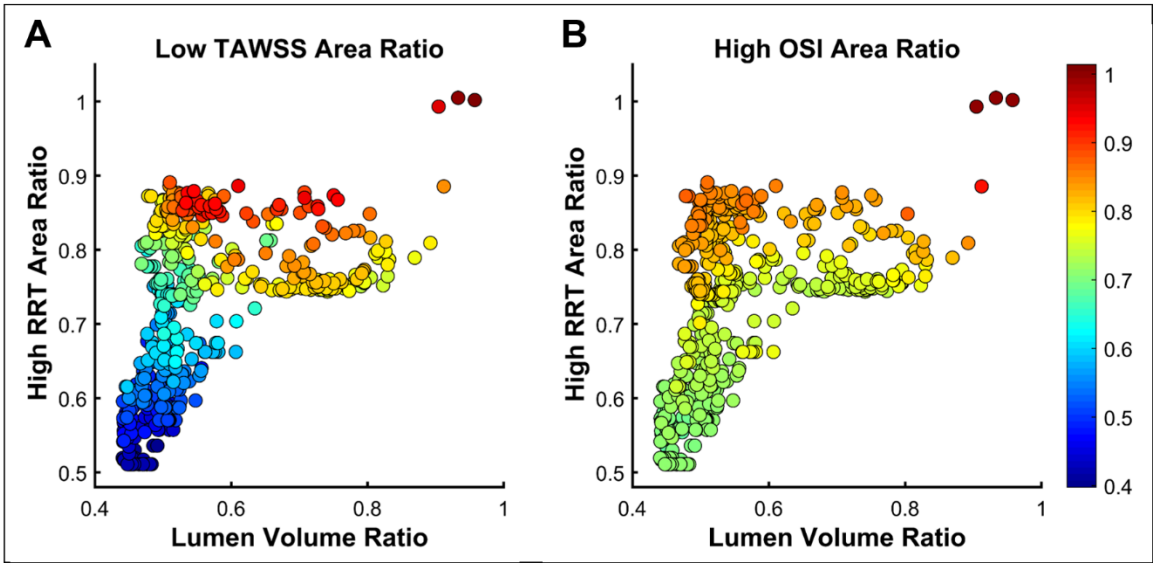


Figure 5.8: Map of RRT constituent parameters onto the normalized objective space. (A) All valid simulation results are plotted against the two objective functions normalized by values from the unstented aorta. Shading of the points shows the normalized area ratio with low TAWSS. (B) Simulation results on the same normalized axes as (A), but with shading showing the normalized area ratio with high OSI. Both panels refer to the colorbar on the right of the figure.

Whereas areas with low TAWSS, high OSI, and high RRT were all reduced compared to the unstented case, both max($TAWSS$) (**Fig. 5.9A**) and flow resistance (**Fig. 5.9B**) increased as lumenal area decreased. The solutions that best minimized the objectives exhibited a maximum TAWSS 1.7 times higher than the unstented value of $29.2\ \mathrm{dyn/cm^2}$, which led to values just below the upper bound constraint of $50\ \mathrm{dyn/cm^2}$. The most optimal designs also exhibited the highest resistance with values nearly 7 times higher than the unstented case, but even the highest resistance values reached only $5\ \mathrm{g/cm^4/s}$, well below the upper bound constraint of $22.2\ \mathrm{g/cm^4/s}$. These findings indicate that if the upper TAWSS threshold were relaxed, additional designs that further minimized both objectives would be found.

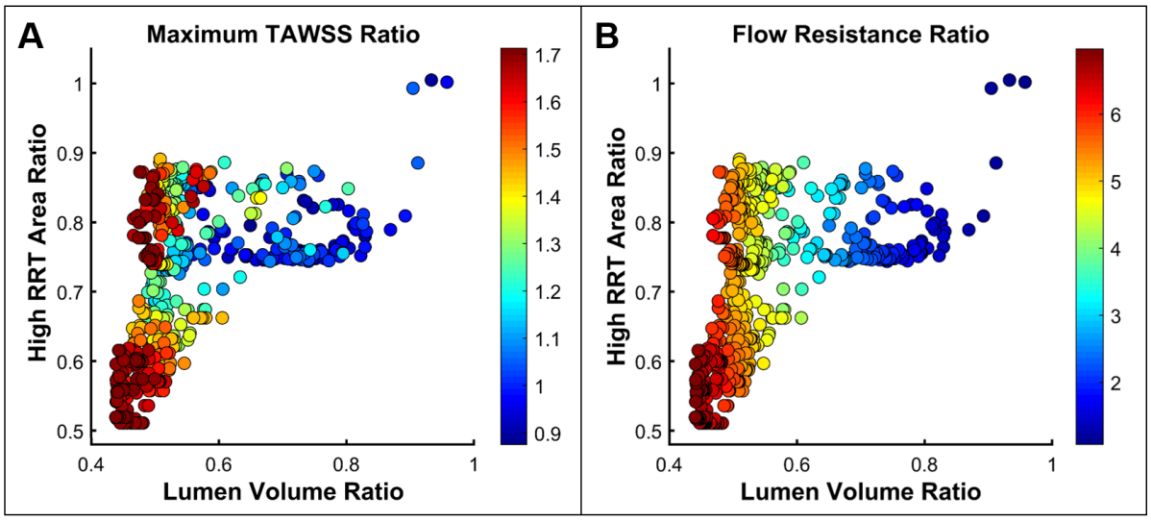


Figure 5.9: Map of additional hemodynamic parameters onto the normalized objective space. (A) All valid simulation results are plotted against the two objective functions normalized by values from the unstented aorta. Shading of the points shows the normalized maximum TAWSS. (B) Simulation results on the same normalized axes as (A), but with shading showing the normalized flow resistance. Note that the two panels have different colorbar scales.

5.7.1.2 Pareto Front – Flow Field

To compare differences among the different designs found on or near the pareto front, four designs (Designs 2-5, marked in **Fig. 5.7B**) were analyzed in greater detail. Each of the designs were similar in appearance, with the defining characteristic being a gradual radius change at the inlet of the stent followed by a slightly steeper gradient toward the outlet. The velocity and pressure profiles for the different designs, and for the unstented model (labeled Design 1), are compared in **Figure 5.10** during both peak systole and end-diastole. There weren't any visible differences in flow during systole among the different stent designs; each of them exhibited accelerated flow within the stented region with velocity reaching up to 230 cm/s. In comparison, the unstented model had a steady maximum velocity of 87 cm/s throughout the domain. Pressure drop across the different designs was consistent with the flow resistance – Designs 2 and 3 had slightly higher flow resistances than Designs 4 and 5, so their peak upstream pressures were about 0.1-0.2 mmHg higher at 132.45 (Design 1) and 132.49 (Design 2) mmHg compared to 132.33 mmHg (Designs 3 and 4).

Pressure drop across each of the stented models was more than twice the 5-mmHg pressure drop across the unstented model.

During diastole, all models exhibit flow reversal, though the unstented model has the lowest reverse flow velocity at 3.7 cm/s. Flow in the stented models broke axisymmetry during the diastolic period to develop vortices distal to the stent. Some minor differences in flow behavior among the stented models become apparent; Design 5, which has the smallest gas volume, had moderate forward velocity but exhibited the highest reverse flow velocity with a peak at 17.9 cm/s. Designs 3 and 4 had much lower reverse velocities at 14.3 and 14.8 cm/s, respectively, but both reached peak forward velocities of over 21 cm/s. overall lower velocities than the other three designs as a result of its wider lumen. Design 2 fell in between the other cases – its forward velocity reached 16 cm/s and its reverse flow peaked at 15.1 cm/s.

One notable difference between the unstented and stented models was in the axial pressure gradient during diastole. During systole, proximal pressure was higher than distal pressure in all models. During diastole, however, a lack of forward-driving flow allowed the stented models to develop slightly higher pressure (<1 mmHg differential) downstream of the stent than upstream. Though small, this effect reflects a fundamental change that the DWSG might induce in patients and warrants further study.

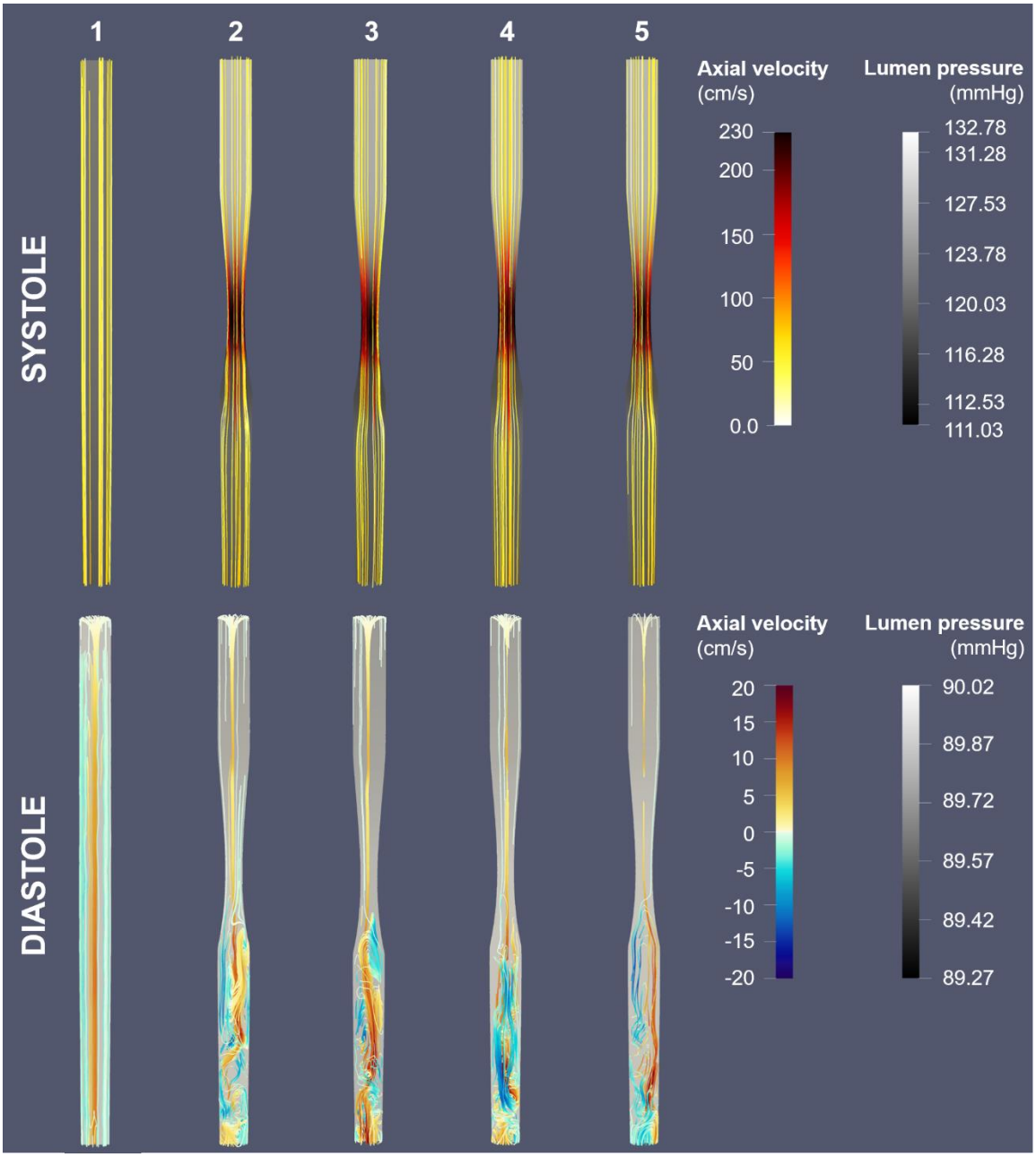


Figure 5.10: Velocity streamlines and pressure for selected CFD simulations. CFD results are shown for the five designs marked in **Fig. 5.7**. Design 1 is the unstented model, while Designs 2-5 all lie on or near the pareto front. Streamlines show blood velocity, and their coloring shows the magnitude of velocity, with negative values corresponding to reverse flow. The shading behind the streamlines shows the blood pressure. The top row of images are taken during peak systole, and the bottom row are from end-diastole. All models on a given row follow the same velocity and pressure colormaps, shown at the end the row.

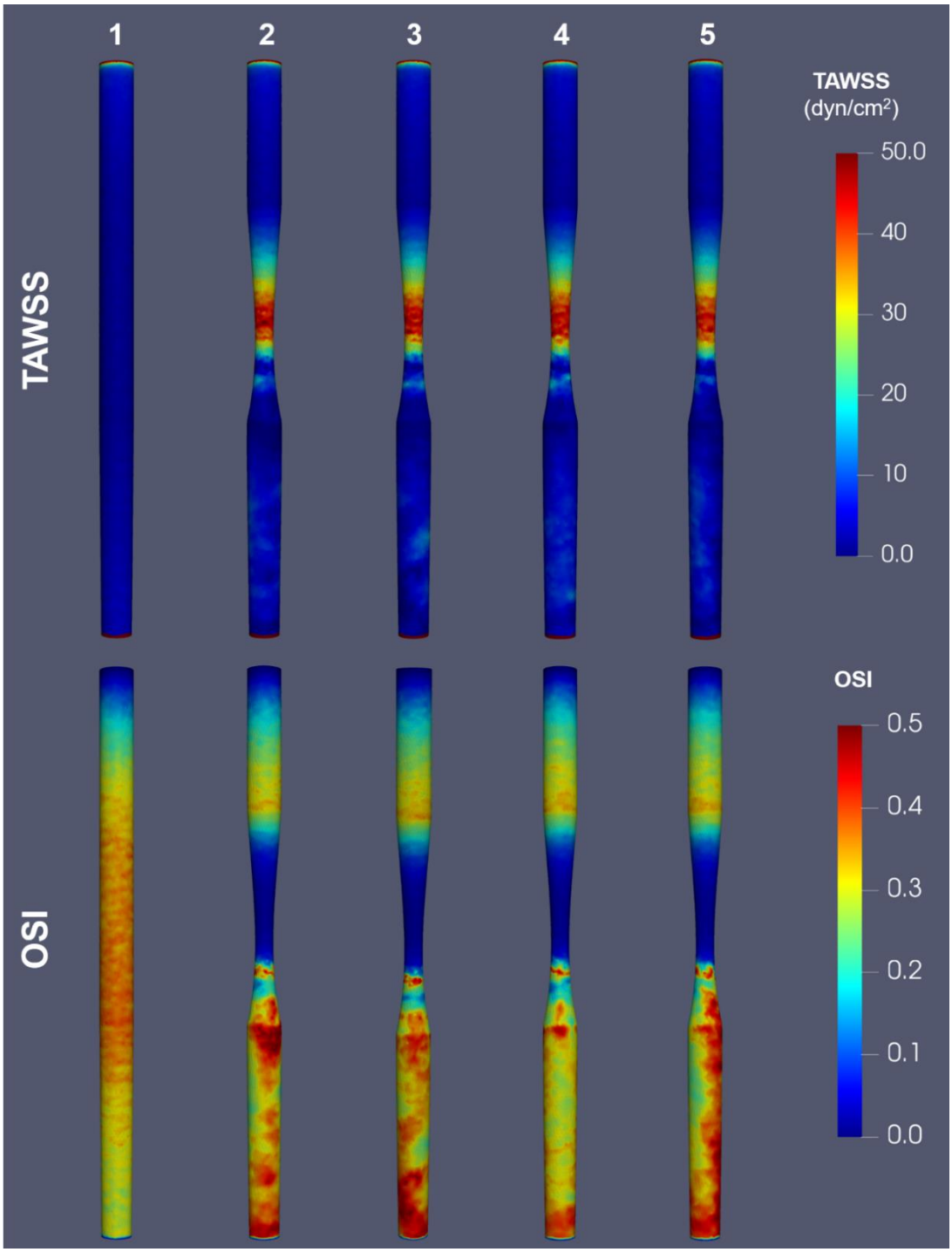


Figure 5.11: TAWSS and OSI maps for selected CFD simulations. CFD results are shown for the five designs marked in **Fig. 5.7**. Design 1 is the unstented model, while Designs 2-5 all lie on or near the pareto front. The top row of images shows TAWSS for the five models. The bottom row shows OSI. Coloration at the inlet and outlet caps is an artifact due to TAWSS and OSI not being calculated for those regions. All models on a given row refer to the single colorbar on the right side of the figure in the same row.

In addition to assessing summary variables such as $\hat{A}_{low\ TAWSS}$ and $\hat{A}_{high\ OSI}$, it was important to look at the spatial distribution of hemodynamic parameters to make comparisons among the longitudinal profile designs. **Figure 5.11** presents maps of TAWSS (top row) and OSI (bottom row) for the five selected models. The unstented model, which acts as a baseline case, exhibited root-mean-square $TAWSS_{rms} = 3.9$ dyn/cm^2 and $OSI_{rms} = 0.32$. Compared to the unstented model, each of the stented models had significantly increased TAWSS, with rms values between 12.6 to 13.0 dyn/cm^2. In addition to the predictable increase in TAWSS in the narrowed stented region of the models, they also had patches of elevated stress distal to the stent. No notable differences in the shear stresses were observed among the different stent designs.

The selected designs showed greater heterogeneity in OSI results (**Fig. 5.11**), especially distal to the stented region. All of the stented models had rms OSI values between 0.27 and 0.29, significantly lower than the unstented model. Distal to the stented region, all models had OSI above 0.32, but Design 2 had the highest value at 0.37. OSI in the unstented model was much higher than expected, with 85% of the model surface exhibiting values above the threshold $OSI_{high} = 0.25$. This result is related to the high proportion of reverse flow seen in the models during diastole. Regardless of the absolute values, the relative decrease in OSI with the various stent designs can be used to inform design decisions.

5.7.2 Circumferential Discretization

A smooth, convex pareto front was found (**Fig. 5.12A**) to define the optimal tradeoff between flow resistance and gas volume in the 2D models of a circumferentially segmented DWSG gas layer. The result was found to be valid for any value of outer radius r_{max}, meaning that the values for inner radius r_{min} in this section (which were generated for $r_{max} = 1$) can be interpreted as the ratio $r_{min}/\ r_{max}$. In other words, the range of r_{min} values from 0.25 to 1 can be generalized as inner radii between 25 to 100% of the outer radius magnitude.

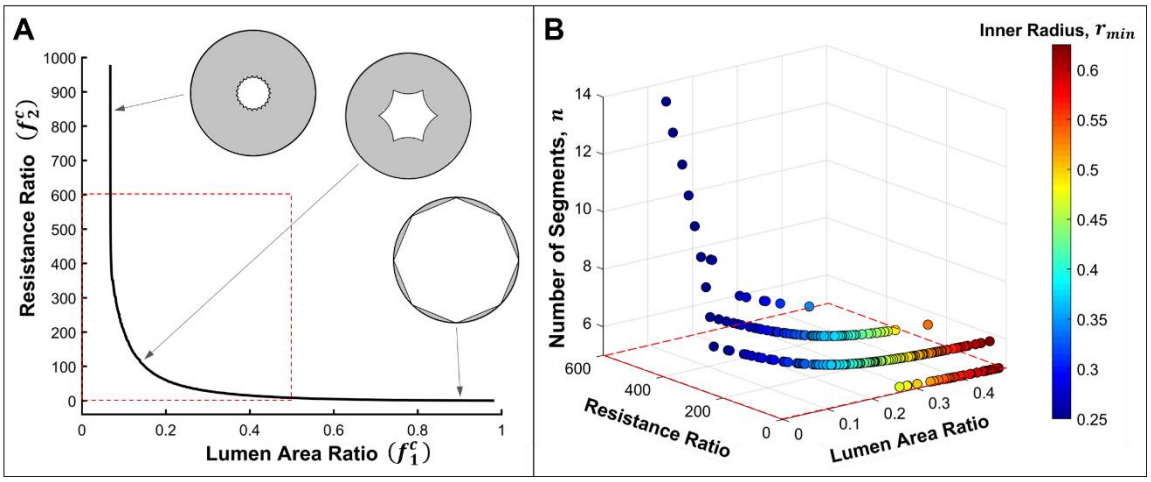


Figure 5.12: Pareto front for circumferential gas layer optimization. (A) The full pareto front showing the tradeoff between DWSG resistance and gas volume with normalized values from a 2D model. Example profiles are shown for points across the front, where the shaded area represents the gas layer. The dashed box identifies the region that is shown in (B). (B) A 3D representation of an excerpt of the pareto front, with the vertical axis showing the number of segments for each design and the shading shows the inner radius of the profile.

Although number of segments n was able to sweep from 3 to 30, the pareto front only represented designs with n between 5 to 30. Furthermore, values of n greater than 15 only generated points at the tail ends of the pareto front, with a lumen area ratio above 0.9 or a resistance ratio above 500. The full allowed range of r_{min} was represented on the pareto front. The design variables that constructed the most optimal region of the pareto front, where both objectives are minimized, fell within a more limited range (**Fig. 5.12B**). When lumen area was below 50% of the unstented area, and resistance of the stent was less than 500 times higher than the unstented value, the number of segments ranged from 5 to 14 and r_{min} fell between 0.25 and 0.625. For a given number of circumferential segments, increasing the inner radius led to decreased resistance but also lower gas volume. For a given radius, decreasing the number of segments led to a small decrease in the gas volume.

A histogram of the number of segments across the entire pareto front (**Fig. 5.13A**) shows that the majority of designs (83%) had between 5 and 7 segments, with 70% of designs having either 6

or 7 segments. Values for inner radius of the gas layer profile (**Fig. 5.13B**) were more evenly distributed, though frequency decreased with increased radius. A small spike occurred for radii between 0.9 to 1, but all of the designs with these values were positioned at the far edge of the pareto front where gas volume is close to zero. As seen in **Fig. 5.12B**, the most optimal designs have values for inner radius between 0.3 to 0.5, though the exact value that minimizes the objectives changes depending on the chosen number of segments.

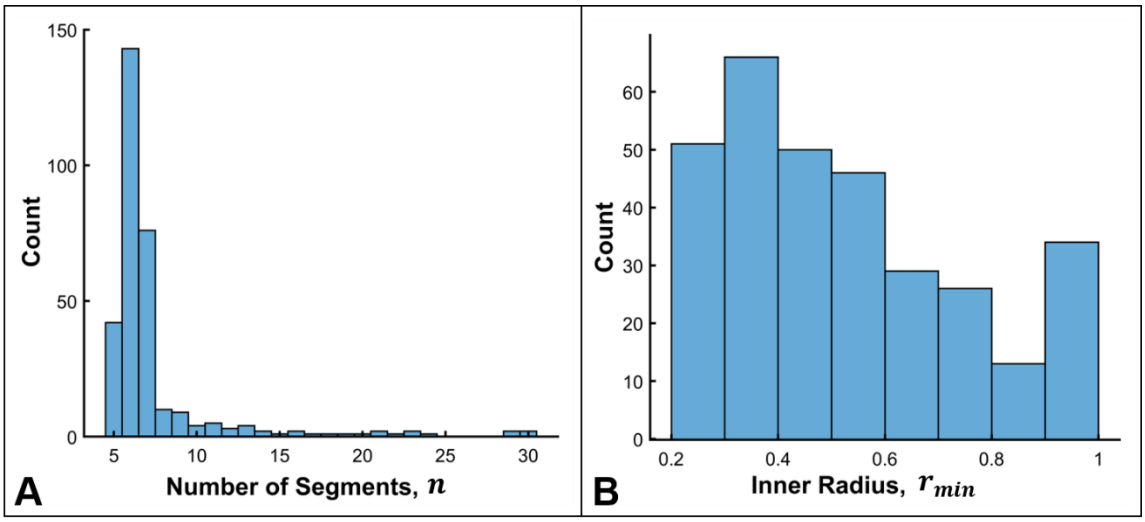


Figure 5.13: Histograms of the design variables in the pareto front for circumferential profile optimization. (A) Number of circumferential segments ranges from 5 to 30, with the highest frequency occurring between 5 to 7 segments. (B) Inner radius of the profile ranges from 0.25 to 1 and has a more uniform distribution of values than the number of segments.

5.8 Discussion

5.8.1 Longitudinal Profile

Multiobjective optimization of the longitudinal DWSG gas layer profile identified several viable designs that incorporate an adequate volume of gas to achieve capacitance without significantly disrupting hemodynamics. Most of the designs at or near the pareto front had a profile that tapered the radius more gradually on the proximal end than the distal end, leading to smooth inflow and a minimum radius positioned closer to the outlet, about two-thirds of the way through the device. These designs had a lumen volume between 30 to 33 mL, corresponding to a gas layer

of 37 to 40 mL. Previous results from Chapters 3 and 4 showed that prototypes of the DWSG with this same amount of gas were able to achieve 12-15% reduction in pulse pressure [119] and 14-29% reduction in pulse wave velocity compared to a standard, rigid stent-graft.

With the chosen objectives and constraints, the limiting factor that prevented the pareto front from further reducing the relative residence time and lumen volume was the maximum allowed TAWSS. Designs that had lower $\hat{A}_{high\ RRT}$ or a larger gas volume than the ones shown in **Fig. 5.7** exhibited at least some areas with TAWSS exceeding $50\ \mathrm{dyn/cm^2}$. This threshold was set as a conservative value, since most reports for dangerous levels of shear stress in blood vessels are reported as instantaneous stresses as opposed to time-averaged values. If the chosen threshold is ultimately decided to be lower than necessary, then it may be best to repeat the optimization procedure to better populate the expanded design space.

Although this study provided valuable insight into the key parameters that will affect DWSG performance, some limitations were identified. One issue that arose during the study was that the CFD mesh was too coarse to capture some of the finer details in the gas layer profile produced by small changes to the design variables. Because the gas layer volume was calculated theoretically from the revolved Bezier curve, this quantity was always an overestimation compared to the actual gas layer volume in the meshed model. It was consistently overestimated since the gas volume is defined by a predominantly concave surface, and when that surface is discretized and connected by straight segments, the resulting volume is smaller. The main impact of this inconsistency is that the entire set of solutions would shift to the right in the objective space (**Fig. 5.7**), and the optimal gas volume would likely be less than 37 mL. The mesh could not be refined further for the optimization study due to the high computational cost associated with conducting hundreds of CFD simulations, but more detailed studies of the final selected designs will need to have better resolution to address this limitation.

5.8.2 Circumferential Discretization

Investigation of potential designs for the circumferential discretization of the DWSG gas layer led to a few interesting findings. It wasn't clear initially whether the number of divisions or segments would have significant impact on the amount of gas that could be stored within a given space between the inner and outer radii. We found that the most optimal designs all fell within a narrow range for this value, and designs with 6 or 7 segments accounted for 70% of the points on the pareto front. As expected, decreasing the inner radius led to a larger gas layer but also a higher resistance flow path. The same objective values could be maintained by simultaneously increasing the number of divisions and increasing the inner radius.

Looking at these results in isolation, the most optimal designs would be the ones closest to zero for both objectives, which correspond to a 50% reduction in lumen radius from the unstented vessel. In the longitudinal profile study, however, we observed that high TAWSS limits were reached well before the stent exceeded the limit we placed on flow resistance. With this knowledge, the preferred circumferential profiles may be further toward the right end of the pareto front. The circumferential optimization was conducted with a highly simplified, 2D model of the gas layer, necessitating the development of simplified 2D objectives and constraints. This approach facilitated rapid generation of hundreds of designs, and the overall trends identified from this model are expected to carry over to 3D. The best approach to develop full 3D DWSG designs will be to combine the information from both of these studies and to compare those designs against the objectives.

5.8.3 Conclusions

This chapter presented two multiobjective optimization studies to explore the design space for the gas layer of a novel double-walled aortic stent-graft. The DWSG, which offers increased compliance over standard, rigid stent-grafts, operates through passive compression and expansion of an internal gas layer over the cardiac cycle. The two optimization studies were developed to for

independent investigation of the longitudinal and circumferential profiles of the gas layer design. Both studies had the dual aim of maximizing gas volume and minimizing flow disturbance. When the information from these two studies is combined, it provides a solid foundation for development of the next generation DWSG prototypes. The viable designs identified through both of these studies again validated the fundamental principle that some of the aorta's conductance can be traded for capacitance in order to reduce the effect of endovascular aortic repair on arterial stiffness and blood pressure. The framework developed for this work, especially the automated CFD workflow for the longitudinal profile optimization, has potential to be utilized for other design problems involving a balance between the geometry of a vascular implant and its effect on hemodynamics.

Chapter 6

Conclusions and Future Directions

6.1 Summary of Findings

Through the work detailed in this thesis, the double-walled stent-graft (DWSG) was conceived and tested via mathematical, computational, and experimental models. The results of the Windkessel study in Chapter 2 revealed the opportunity to trade aortic conductance for increased capacitance, though it wasn't clear at that point the most feasible way to increase capacitance without interfering with the primary protective function of standard stent-grafts. In Chapter 3, the first prototype of the DWSG was characterized through static and dynamic experiments, demonstrating the viability of a gas layer lining the inner wall of a stent-graft as a vehicle to incorporate capacitance that doesn't depend on distensibility of the surrounding vessel wall. Adding more gas to the prototypes furthered their ability to reduce peak and pulse pressures in a flow loop system, and the adverse effect of restricting the flow path wasn't observed until the gas occupied over 70% of the stent-graft volume.

The effect of the DWSG on aortic stiffness (measured via pulse wave velocity) was investigated in Chapter 4 through a computational fluid-structure interaction model and again in a flow loop model. Through both of these approaches, the DWSG consistently yielded lower pulse wave velocity values compared to a model of a standard, rigid stent-graft. Differing trends between experimental setups with a compliant versus stiff model of the aorta supported findings from Chapter 3 that the benefit of the DWSG is expected to be greater in patients with a stiffer arterial system, and a stiff aorta in particular.

Finally, an optimization study was conducted in Chapter 5 to evaluate how different configurations of the DWSG gas layer affect hemodynamics across the aorta. Rather than considering only macroscale behaviors like blood pressure and pulse wave velocity, this work gave

insight into local shear stresses and recirculation that developed upstream, downstream, or within the DWSG. Hundreds of designs were generated through the optimization procedure, but the most optimal ones shared similar characteristics, including a very gradual tapering at the inlet and a total gas volume of 30 to 40 mL in the 15 cm long segment. One strategy was investigated to make the DWSG lumen convex, enabling compression of the gas if an inextensible membrane is used to contain it. Optimal ranges for number and size of circumferentially discretized gas layer segments were identified for use in future device models and prototypes.

6.2 Potential Impact of the DWSG

Several different embodiments of the DWSG concept were developed and tested over the course of this thesis; in spite of the variation among the different models, a few promising behaviors remained consistent. Each of the DWSG models demonstrated improved performance over a standard stent-graft, either by lowering blood pressure or reducing pulse wave velocity (PWV). Either of these outcomes have potential to greatly improve the long-term health of patients receiving a stent-graft for aortic repair. A meta-analysis of the predictive value of PWV on patient health found that a 1 m/s increase in PWV was associated with a 15% increase in both cardiovascular and all-cause mortality after adjusting for other risk factors [35]. Similarly, a meta-analysis of the effect of blood pressure showed that the risk of major cardiovascular events decreased by about 10% for each 5 mmHg reduction achieved in systolic blood pressure, and a 10 mmHg reduction in systolic pressure was associated with a 13% reduction in all-cause mortality [111]. These measures – 1 m/s change in PWV and 5-10 mmHg change in systolic pressure – are within the ranges that have been achieved in experiments and simulations with the DWSG. Even if the device is unable to reduce blood pressure or aortic stiffness completely to healthy levels, it will still offer a significant positive impact on the patient population.

A device similar to the DWSG is currently undergoing clinical testing for treatment of pulmonary hypertension. In that condition, the pulmonary artery becomes unusually stiff, blood

pressure in the right heart and lungs increases, and the pressure overload causes damage to the lungs and heart. A device developed by Aria CV consists of a balloon mounted on a stent and connected to a reservoir [199]. The balloon is fixed in the pulmonary artery, and the reservoir is implanted remotely under the skin. As the heart pumps, the balloon shrinks through compression of the contained gas and through transport of some of the gas to the reservoir, and then the balloon refills when the right heart refills. Though different in configuration, and much more complex, the Aria CV device utilizes the concept increasing capacitance of a large artery through compression (and displacement) of a gas. As this device continues to move through the stages of regulatory approval, it will act as a role model for bringing the DWSG to market.

As discussed in Chapter 1, the primary target for the DWSG is patients undergoing endovascular repair for Type B aortic dissection (T_BAD). The mean age of these patients at diagnosis is 68 years, and about 75% of them have hypertension [65,90]. For these patients, it could be argued that high aortic stiffness and hypertension are significant factors contributing to the development of one or more tears in the aortic wall. Placement of currently available stent-grafts for these patients is not a cure for the underlying disease, as evidenced by 5 year survival of only 50 to 65% and development of new aortic tears in 4 to 27% of patients [90,200,201]. By treating T_BAD with the DWSG instead of a traditional stent-graft, the underlying pathology is more effectively treated. It is possible that if the aorta were stiff enough prior to stenting, placement of the DWSG may be able to therapeutically decrease the effective stiffness of the aorta and allow the patient to become less dependent on antihypertensive medications.

If the DWSG is found to be safe and effective in patients with T_BAD, who stand to benefit the most but also have several comorbidities, then it may be explored as an alternative device for many other endovascular aortic repairs, including aneurysm or dissection in other regions of the aorta. Standard stent-grafts are known to adversely affect blood pressure and arterial stiffness across all

patient demographics, so a device that reduces or eliminates these effects would undoubtably be an improvement over the current standard of care [88,101,155].

6.3 Next Steps in Device Development

Additional design and validation work must be done before the DWSG can be shown to be safe and effective for use in humans. The two main areas that must be addressed in future work are how the device will be deployed and what materials can be used to ensure long-term safety and function of the device *in vivo*. Both of these areas are briefly addressed in the following sections. Finally, plans for the next stage of device testing are discussed.

6.3.1 Deployment

Ease of deployment is a feature that most modern stent-grafts tout, making it an important consideration – and potential drawback – for the DWSG. Because the DWSG consists of two components – the stiff, outer stent-graft and the inner gas layer tube – it may be difficult for both components to fit within the same 4 to 8 mm diameter deployment system used for state-of-the-art thoracic devices. To achieve this slim profile for deployment, inspiration may be taken from the Nellix Endovascular Aneurysm Sealing System developed by Endologix for treatment of abdominal aortic aneurysms [141]. This device is constructed similarly to the DWSG, though its purpose is to fill the surrounding aneurysm sac with a hardening polymer to improve fixation and prevent leakage. It consists of a standard stent-graft with a thin plastic bag attached around the outside, much like the DWSG has a thin plastic bag attached to the inside. Despite having multiple components, the Nellix device fits within a delivery catheter with a 6 mm outer diameter. Stent-grafts for the abdominal aorta tend to be smaller than those for the thoracic aorta, but this low profile device still suggests that it will be feasible to deploy the DWSG within a standard-sized delivery system.

If the device cannot be easily compacted down to the necessary size, a different approach will need to be taken. One option is that the outer stent-graft and the inner gas tube could be two completely independent pieces, which would be deployed separately and possibly not even during the same procedure. One advantage to pursuing this option is the ability to "retrofit" previously implanted stent-grafts with the gas layer lining, which would greatly expand the pool of eligible patients. With this option, the gas layer may be similar to the Aria CV device in that it would have bare-metal stents on either end to allow it to be fixed in the vessel, either within a pre-placed stent-graft or even in the unstented aorta if it is found to have therapeutic benefit in patients with significant aortic stiffening.

Whether it is deployed with or after the stent-graft portion, the gas layer will need to be completely empty during placement. Filling the device with gas endovascularly will be another challenge to address during DWSG development. Again, inspiration can be drawn from the Nellix device, which has lines on the delivery system allowing for remote injection of the sealing polymer into the deployed bag. After injection of the gas into the DWSG, the filling port will need to easily seal through use of a self-sealing material, a one-way valve, or a deployed adhesive to ensure that the gas remains within the gas layer after the filling system is detached.

6.3.2 Materials & Durability

Any thin vessel that stores gas – tires, balloons, soda bottles – tends to leak over time. Preventing gas from leaking out of the DWSG will be one of the driving factors for deciding the final materials and configuration for the device. Although a biocompatible gas like CO_2 can be used so that leakage does not pose any risk to the patient, loss of gas from the DWSG corresponds to loss in capacitive function. One parameter that can be easily controlled to reduce leakage is the gas pressure before implantation. One of the reasons that things like balloons and soda bottles leak gas quickly is because the gas is under a high positive pressure. Something like bubble wrap, on the other hand, is not formed with the gas pressurized at all, so the surrounding plastic membrane is

loose. The lack of pressure differential in bubble wrap makes it much more stable for long-term storage of the air. Once implanted, the DWSG gas layer will be pressurized by the lumenal blood pressure, but the level of pressurization can be minimized by avoiding a positive gas pressure in the unloaded state.

The other ways to control gas diffusion out of the device are by choice of gas and choice of material for the housing film. Options for gas are limited to those that diffuse readily into the bloodstream, but it is worth investigating which biocompatible gases have the lowest diffusivity across the potential film materials. More options are available for selection of the film material, which can be modeled off of existing devices including balloon catheter balloons, intra-aortic balloon pumps, or other membranous medical device components, all of which use some type of polymer. Regardless of the material chosen, finite element simulations should be conducted to find how thick the film can be made before it becomes too stiff or prone to fracture from cyclic loading. Increasing the film thickness will always improve gas retention, but it should not be allowed to interfere with mechanical function or longevity. Because the material filling the gas layer will be precisely controlled (only CO_2 or some other specific gas compound), the film may be coated on the gas side with a material with specific pH, charge, or other treatment that is effective at repelling specifically the chemicals that constitute the contained gas. Any material chosen for the film layer will need to strike a balance between low diffusivity and high resistance to fatigue fracture, making this potentially another problem requiring an optimization study.

6.3.3 Validation Study in Cadaveric Aortas

The next step toward proving the safety and efficacy of the DWSG is to conduct flow experiments in an environment that better represents the human arterial system. All of the experiments conducted up to this point have used rubber tubing to approximate the stiffness and behavior of the aorta, but it is expected that unique challenges will arise with placement and fixation of the device in an actual vessel. It is also important quantify the effect of the DWSG on effective

arterial stiffness in models with different levels of atherosclerosis and aortic stiffening. To address these uncertainties, an experiment has been designed in which cadaveric aortas will be connected from aortic root to iliac bifurcation into a flow loop system that can reproduce physiologic input flows and downstream resistance. With this setup, pressure will be measured upstream and downstream of the aorta to provide an estimate of pulse wave velocity. The system will be run under three conditions: (1) with no stent-graft placed, (2) with a commercial stent-graft, and (3) with a DWSG prototype placed in the descending thoracic aorta. Under each condition, pressure measurements will be taken to calculate the effective stiffness of the aorta. This study will provide stronger evidence toward the ability of the DWSG to impact blood pressure and arterial stiffness *in vivo*; it will also highlight challenges with device design, relating to placement and fixation, that will need to be addressed prior to any live animal studies.

Bibliography

[1] Iaizzo, P. A., 2009, *Handbook of Cardiac Anatomy, Physiology, and Devices*, Springer.

[2] Sidebotham, D., and Le Grice, I. J., 2007, "Physiology and Pathophysiology," *Cardiothoracic Critical Care*, Elsevier, pp. 3–27.

[3] Spina, M., Garbisa, S., Hinnie, J., Hunter, J. C., and Serafini-Fracassini, A., 1983, "Age-Related Changes in Composition and Mechanical Properties of the Tunica Media of the Upper Thoracic Human Aorta," Arteriosclerosis, **3**(1), pp. 64–76.

[4] Andreotti, L., Bussotti, A., Cammelli, D., di Giovine, F., Sampognaro, S., Sterrantino, G., Varcasia, G., and Arcangeli, P., 1985, "Aortic Connective Tissue in Ageing—A Biochemical Study," Angiology, **36**(12), pp. 872–879.

[5] Emmott, A., Garcia, J., Chung, J., Lachapelle, K., El-Hamamsy, I., Mongrain, R., Cartier, R., and Leask, R. L., 2016, "Biomechanics of the Ascending Thoracic Aorta: A Clinical Perspective on Engineering Data," Can. J. Cardiol., **32**(1), pp. 35–47.

[6] Redheuil, A., Yu, W. C., Wu, C. O., Mousseaux, E., De Cesare, A., Yan, R., Kachenoura, N., Bluemke, D., and Lima, J. A. C., 2010, "Reduced Ascending Aortic Strain and Distensibility: Earliest Manifestations of Vascular Aging in Humans," Hypertension, **55**(2), pp. 319–326.

[7] Länne, T., Sonesson, B., Bergqvist, D., Bengtsson, H., and Gustafsson, D., 1992, "Diameter and Compliance in the Male Human Abdominal Aorta: Influence of Age and Aortic Aneurysm," Eur. J. Vasc. Surg., **6**(2), pp. 178–184.

[8] Redheuil, A., Wu, C., Yan, R. T., Bertoni, A. G., Hundley, G. W., Duprez, D. A., Jacobs, D. R., Daniels, L. B., Bluemke, D. A., and Lima, J. A. C., 2013, "Proximal Aortic Distensibility Is an Independent Predictor of All-Cause Mortality and Incident Cardiovascular Events in the Multi-Ethnic Study of Atherosclerosis," Eur. Heart J., **34**(suppl 1), pp. 2656–2656.

[9] Ha, H., Ziegler, M., Welander, M., Bjarnegård, N., Carlhäll, C.-J., Lindenberger, M., Länne, T., Ebbers, T., and Dyverfeldt, P., 2018, "Age-Related Vascular Changes Affect Turbulence in Aortic Blood Flow," Front. Physiol., **9**(JAN), pp. 1–10.

[10] Benim, A. C., Nahavandi, A., Assmann, A., Schubert, D., Feindt, P., and Suh, S. H., 2011, "Simulation of Blood Flow in Human Aorta with Emphasis on Outlet Boundary Conditions," Appl. Math. Model., **35**(7), pp. 3175–3188.

[11] Stalder, A. F., Frydrychowicz, A., Russe, M. F., Korvink, J. G., Hennig, J., Li, K., and Markl, M., 2011, "Assessment of Flow Instabilities in the Healthy Aorta Using Flow-Sensitive MRI," J. Magn. Reson. Imaging, **33**(4), pp. 839–846.

[12] Kousera, C. A., Wood, N. B., Seed, W. A., Torii, R., O'Regan, D., and Xu, X. Y., 2012, "A Numerical Study of Aortic Flow Stability and Comparison With In Vivo Flow Measurements," J. Biomech. Eng., **135**(1), p. 011003.

[13] Tan, F. P. P., Borghi, A., Mohiaddin, R. H., Wood, N. B., Thom, S., and Xu, X. Y., 2009, "Analysis of Flow Patterns in a Patient-Specific Thoracic Aortic Aneurysm Model," Comput. Struct., **87**(11–12), pp. 680–690.

[14] Khanafer, K., and Berguer, R., 2009, "Fluid–Structure Interaction Analysis of Turbulent

Pulsatile Flow within a Layered Aortic Wall as Related to Aortic Dissection," J. Biomech., **42**(16), pp. 2642–2648.

[15] Wan Ab Naim, W. N., Ganesan, P. B., Sun, Z., Lei, J., Jansen, S., Hashim, S. A., Ho, T. K., and Lim, E., 2018, "Flow Pattern Analysis in Type B Aortic Dissection Patients after Stent-Grafting Repair: Comparison between Complete and Incomplete False Lumen Thrombosis," Int. j. numer. method. biomed. eng., **34**(5), pp. 1–13.

[16] Gallo, D., Lefieux, A., Morganti, S., Veneziani, A., Reali, A., Auricchio, F., Conti, M., and Morbiducci, U., 2016, "A Patient-Specific Follow up Study of the Impact of Thoracic Endovascular Repair (TEVAR) on Aortic Anatomy and on Post-Operative Hemodynamics," Comput. Fluids, **141**, pp. 54–61.

[17] Chiu, T. L., Tang, A. Y. S., Cheng, S. W. K., and Chow, K. W., 2018, "Analysis of Flow Patterns on Branched Endografts for Aortic Arch Aneurysms," Informatics Med. Unlocked, **13**(August), pp. 62–70.

[18] Morbiducci, U., Ponzini, R., Gallo, D., Bignardi, C., and Rizzo, G., 2013, "Inflow Boundary Conditions for Image-Based Computational Hemodynamics: Impact of Idealized versus Measured Velocity Profiles in the Human Aorta," J. Biomech., **46**(1), pp. 102–109.

[19] Frauenfelder, T., Lotfey, M., Boehm, T., and Wildermuth, S., 2006, "Computational Fluid Dynamics: Hemodynamic Changes in Abdominal Aortic Aneurysm after Stent-Graft Implantation," Cardiovasc. Intervent. Radiol., **29**(4), pp. 613–623.

[20] Pirola, S., Cheng, Z., Jarral, O. A., O'Regan, D. P., Pepper, J. R., Athanasiou, T., and Xu, X. Y., 2017, "On the Choice of Outlet Boundary Conditions for Patient-Specific Analysis of Aortic Flow Using Computational Fluid Dynamics," J. Biomech., **60**, pp. 15–21.

[21] Zieman, S. J., Melenovsky, V., and Kass, D. A., 2005, "Mechanisms, Pathophysiology, and Therapy of Arterial Stiffness," Arterioscler. Thromb. Vasc. Biol., **25**(5), pp. 932–943.

[22] Mitchell, G. F., Hwang, S. J., Vasan, R. S., Larson, M. G., Pencina, M. J., Hamburg, N. M., Vita, J. A., Levy, D., and Benjamin, E. J., 2010, "Arterial Stiffness and Cardiovascular Events: The Framingham Heart Study," Circulation, **121**(4), pp. 505–511.

[23] Callaghan, F. J., Geddes, L. A., Babbs, C. F., and Bourland, J. D., 1986, "Relationship between Pulse-Wave Velocity and Arterial Elasticity," Med. Biol. Eng. Comput., **24**(3), pp. 248–254.

[24] Safar, M. E., O'Rourke, M. F., and Frohlich, E. D., eds., 2014, *Blood Pressure and Arterial Wall Mechanics in Cardiovascular Diseases*, Springer London, London.

[25] Van Bortel, L. M., Laurent, S., Boutouyrie, P., Chowienczyk, P., Cruickshank, J. K., De Backer, T., Filipovsky, J., Huybrechts, S., Mattace-Raso, F. U. S., Protogerou, A. D., Schillaci, G., Segers, P., Vermeersch, S., and Weber, T., 2012, "Expert Consensus Document on the Measurement of Aortic Stiffness in Daily Practice Using Carotid-Femoral Pulse Wave Velocity," J. Hypertens., **30**(3), pp. 445–448.

[26] Mattace-Raso, F. U. S., Hofman, A., Verwoert, G. C., Wittemana, J. C. M., Wilkinson, I., Cockcroft, J., McEniery, C., Yasmina, Laurent, S., Boutouyrie, P., Bozec, E., Hansen, T. W., Torp-Pedersen, C., Ibsen, H., Jeppesen, J., Vermeersch, S. J., Rietzschel, E., de Buyzere, M., Gillebert, T. C., van Bortel, L., Segers, P., Vlachopoulos, C., Aznaouridis, C., Stefanadis, C., Benetos, A., Labat, C., Lacolley, P., Stehouwer, C. D. A., Nijpels, G., Dekker, J. M., Ferreira, I., Twisk, J. W. R., Czernichow, S., Galan, P., Hercberg, S., Pannier, B.,

Guérin, A., London, G., Kennedy Cruickshank, J., Anderson, S. G., Paini, A., Rosei, E. A., Muiesan, M. L., Salvetti, M., Filipovsky, J., Seidlerova, J., and Dolejsova, M., 2010, "Determinants of Pulse Wave Velocity in Healthy People and in the Presence of Cardiovascular Risk Factors: 'Establishing Normal and Reference Values,'" Eur. Heart J., **31**(19), pp. 2338–2350.

[27] Wilkinson, I. B., MacCallum, H., Flint, L., Cockcroft, J. R., Newby, D. E., and Webb, D. J., 2000, "The Influence of Heart Rate on Augmentation Index and Central Arterial Pressure in Humans," J. Physiol., **525**(1), pp. 263–270.

[28] Xiao, N., Humphrey, J. D., and Figueroa, C. A., 2013, "Multi-Scale Computational Model of Three-Dimensional Hemodynamics within a Deformable Full-Body Arterial Network," J. Comput. Phys., **244**, pp. 22–40.

[29] Agabiti-Rosei, E., Mancia, G., O'Rourke, M. F., Roman, M. J., Safar, M. E., Smulyan, H., Wang, J. G., Wilkinson, I. B., Williams, B., and Vlachopoulos, C., 2007, "Central Blood Pressure Measurements and Antihypertensive Therapy: A Consensus Document," Hypertension, **50**(1), pp. 154–160.

[30] Cuomo, F., Roccabianca, S., Dillon-murphy, D., Xiao, N., Humphrey, J. D., and Figueroa, C. A., 2017, "Effects of Age-Associated Regional Changes in Aortic Stiffness on Human Hemodynamics Revealed by Computational Modeling," PLoS One, **12**(3), pp. 1–21.

[31] Wu, C., Liu, P., Wu, T., Hung, Y., Yang, S., and Lin, G., 2015, "Therapeutic Modification of Arterial Stiffness: An Update and Comprehensive Review," World J. Cardiol., **7**(11), pp. 742–754.

[32] Laurent, S., Boutouyrie, P., Asmar, R., Gautier, I., Laloux, B., Guize, L., Ducimetiere, P., and Benetos, A., 2001, "Aortic Stiffness Is an Independent Predictor of All-Cause and Cardiovascular Mortality in Hypertensive Patients.," Hypertension, **37**(5), pp. 1236–1241.

[33] Mitchell, G. F., 2008, "Effects of Central Arterial Aging on the Structure and Function of the Peripheral Vasculature: Implications for End-Organ Damage," J. Appl. Physiol., **105**(5), pp. 1652–1660.

[34] Adji, A., O'Rourke, M. F., and Namasivayam, M., 2011, "Arterial Stiffness, Its Assessment, Prognostic Value, and Implications for Treatment," Am. J. Hypertens., **24**(1), pp. 5–17.

[35] Vlachopoulos, C., Aznaouridis, K., and Stefanadis, C., 2010, "Prediction of Cardiovascular Events and All-Cause Mortality With Arterial Stiffness. A Systematic Review and Meta-Analysis," J. Am. Coll. Cardiol., **55**(13), pp. 1318–1327.

[36] Gkaliagkousi, E., and Douma, S., 2009, "The Pathogenesis of Arterial Stiffness and Its Prognostic Value in Essential Hypertension and Cardiovascular Diseases," Hippokratia, **13**(2), pp. 70–75.

[37] Hundley, W. G., Kitzman, D. W., Morgan, T. M., Hamilton, C. A., Darty, S. N., Stewart, K. P., Herrington, D. M., Link, K. M., and Little, W. C., 2001, "Cardiac Cycle-Dependent Changes in Aortic Area and Distensibility Are Reduced in Older Patients with Isolated Diastolic Heart Failure and Correlate with Exercise Intolerance," J. Am. Coll. Cardiol., **38**(3), pp. 796–802.

[38] Townsend, R. R., Wilkinson, I. B., Schiffrin, E. L., Avolio, A. P., Chirinos, J. A., Cockcroft, J. R., Heffernan, K. S., Lakatta, E. G., McEniery, C. M., Mitchell, G. F., Najjar, S. S., Nichols, W. W., Urbina, E. M., and Weber, T., 2015, *Recommendations for Improving and*

Standardizing Vascular Research on Arterial Stiffness: A Scientific Statement from the American Heart Association.

[39] Matsumoto, T., and Hayashi, K., 1996, "Stress and Strain Distribution in Hypertensive and Normotensive Rat Aorta Considering Residual Strain," J. Biomech. Eng., **118**(1), pp. 62–73.

[40] Bonert, M., Leask, R. L., Butany, J., Ethier, C. R., Myers, J. G., Johnston, K. W., and Ojha, M., 2003, "The Relationship between Wall Shear Stress Distributions and Intimal Thickening in the Human Abdominal Aorta," Biomed. Eng. Online, **2**(1), p. 18.

[41] Malek, A. M., Alper, S. L., and Izumo, S., 1999, "Hemodynamic Shear Stress and Its Role in Atherosclerosis," JAMA, **282**(21), p. 2035.

[42] Langille, B. L., and O'Donnell, F., 1986, "Reductions in Arterial Diameter Produced by Chronic Decreases in Blood Flow Are Endothelium-Dependent," Science (80-.)., **231**(4736), pp. 405–407.

[43] Fry, D. L., 1969, "Certain Chemorheologic Considerations Regarding the Blood Vascular Interface with Particular Reference to Coronary Artery Disease," Circulation, **39**(November), pp. IV38-57.

[44] Meneton, P., Jeunemaitre, X., de Wardener, H. E., and MacGregor, G. A., 2005, "Links between Dietary Salt Intake, Renal Salt Handling, Blood Pressure, and Cardiovascular Diseases.," Physiol. Rev., **85**(2), pp. 679–715.

[45] Avolio, A. P., Clyde, K. M., Beard, T. C., Cooke, H. M., Ho, K. K., and O'Rourke, M. F., 1986, "Improved Arterial Distensibility in Normotensive Subjects on a Low Salt Diet," Arterioscler. Thromb. Vasc. Biol., **6**(2), pp. 166–169.

[46] Levenson, J. A., Simon, A. C., Maarek, B. E., Gitelman, R. J., Fiessinger, J. N., and Safar, M. E., 1985, "Regional Compliance of Brachial Artery and Saline Infusion in Patients with Arteriosclerosis Obliterans," Arteriosclerosis, **5**(1), pp. 80–87.

[47] Kinlay, S., Creager, M. A., Fukumoto, M., Hikita, H., Fang, J. C., Selwyn, A. P., and Ganz, P., 2001, "Endothelium-Derived Nitric Oxide Regulates Arterial Elasticity in Human Arteries In Vivo," Hypertension, **38**(5), pp. 1049–1053.

[48] Xu, J., and Shi, G.-P., 2014, "Vascular Wall Extracellular Matrix Proteins and Vascular Diseases," Biochim. Biophys. Acta - Mol. Basis Dis., **1842**(11), pp. 2106–2119.

[49] Soran, O., Kennard, E. D., Kfoury, A. G., and Kelsey, S. F., 2006, "Two-Year Clinical Outcomes after Enhanced External Counterpulsation (EECP) Therapy in Patients with Refractory Angina Pectoris and Left Ventricular Dysfunction (Report from the International EECP Patient Registry)," Am. J. Cardiol., **97**(1), pp. 17–20.

[50] Nwankwo, T., Yoon, S. S. (Sarah), Burt, V., and Gu, Q., 2013, "Hypertension Among Adults in the United States : National Health and Nutrition Examination Survey , 2011 – 2012," NCHS Data Brief, (133).

[51] Whelton, P. K., Carey, R. M., Aronow, W. S., Ovbiagele, B., Casey, D. E., Smith, S. C., Collins, K. J., Spencer, C. C., Himmelfarb, C. D., Stafford, R. S., Depalma, S. M., Taler, S. J., Gidding, S., Thomas, R. J., Jamerson, K. A., Williams, K. A., Jones, D. W., Williamson, J. D., Maclaughlin, E. J., Wright, J. T., and Mauri, L., 2017, "2017 ACC / AHA / AAPA / ABC / ACPM / AGS / APhA / ASH / ASPC / NMA / PCNA Guideline for the Prevention , Detection , Evaluation , and Management of High Blood Pressure in Adults A Report of the

American College of Cardiology / American Heart Association T," J Am Coll Cardiol., p. pii: S0735-1097(17)41519-1.

[52] Benjamin EJ, Blaha MJ, Chiuve SE, Cushman M, Das SR, Deo R, de Ferranti SD, Floyd J, Fornage M, Gillespie C, Isasi CR, Jimenez MC, Jordan LC, Judd SE, Lackland D, Lichtman JH, Lisabeth L, Liu S, Longenecker CT, Mackey RH, Matsushita K, Mozaffarian D, Muss, M. P., 2017, "Heart Disease and Stroke Statistics - 2017 Update: At-a-Glance," Circulation., **135**(10), pp. E146–E603.

[53] Andreadis, E. A., ed., 2016, *Hypertension and Cardiovascular Disease*, Springer International Publishing, Cham.

[54] Learoyd, B. M., and Taylor, M. G., 1966, "Alterations with Age in the Viscoelastic Properties of Human Arterial Walls.," Circ. Res., **18**(3), pp. 278–292.

[55] Haskett, D., Johnson, G., Zhou, A., Utzinger, U., and Vande Geest, J., 2010, "Microstructural and Biomechanical Alterations of the Human Aorta as a Function of Age and Location," Biomech. Model. Mechanobiol., **9**(6), pp. 725–736.

[56] Mohiaddin, R. H., Firmin, D. N., and Longmore, D. B., 1993, "Age-Related Changes of Human Aortic Flow Wave Velocity Measured Noninvasively by Magnetic Resonance Imaging.," J. Appl. Physiol., **74**(1), pp. 492–497.

[57] Redheuil, A., Yu, W. C., Mousseaux, E., Harouni, A. A., Kachenoura, N., Wu, C. O., Bluemke, D., and Lima, J. A. C., 2011, "Age-Related Changes in Aortic Arch Geometry: Relationship with Proximal Aortic Function and Left Ventricular Mass and Remodeling," J. Am. Coll. Cardiol., **58**(12), pp. 1262–1270.

[58] Groenink, M., Langerak, S. E., Vanbavel, E., Van Der Wall, E. E., Mulder, B. J. M., Van Der Wal, A. C., and Spaan, J. A. E., 1999, "The Influence of Aging and Aortic Stiffness on Permanent Dilation and Breaking Stress of the Thoracic Descending Aorta," Cardiovasc. Res., **43**(2), pp. 471–480.

[59] Folkow, B., and Svanborg, A., 1993, "Physiology of Cardiovascular Aging," Physiol. Rev., **73**(4), pp. 725–764.

[60] Pettersen, K. H., Bugenhagen, S. M., Nauman, J., Beard, D. A., and Omholt, S. W., 2014, "Arterial Stiffening Provides Sufficient Explanation for Primary Hypertension," PLoS Comput. Biol., **10**(5).

[61] Lederle, F. A., Johnson, G., and Wilson, S., 1997, "Prevalence and Associations of Abdominal Aortic Aneurysm Detected through Screening," Ann. Intern. Med., **126**(6), p. 441.

[62] Olsson, C., Thelin, S., Ståhle, E., Ekbom, A., and Granath, F., 2006, "Thoracic Aortic Aneurysm and Dissection: Increasing Prevalence and Improved Outcomes Reported in a Nationwide Population-Based Study of More than 14 000 Cases from 1987 to 2002," Circulation, **114**(24), pp. 2611–2618.

[63] Pasta, S., Agnese, V., Gallo, A., Cosentino, F., Di Giuseppe, M., Gentile, G., Raffa, G. M., Maalouf, J. F., Michelena, H. I., Bellavia, D., Conaldi, P. G., and Pilato, M., 2020, "Shear Stress and Aortic Strain Associations With Biomarkers of Ascending Thoracic Aortic Aneurysm," Ann. Thorac. Surg., **110**(5), pp. 1595–1604.

[64] Karthikesalingam, A., Holt, P. J., Vidal-Diez, A., Ozdemir, B. A., Poloniecki, J. D., Hinchliffe, R. J., and Thompson, M. M., 2014, "Mortality from Ruptured Abdominal Aortic

Aneurysms: Clinical Lessons from a Comparison of Outcomes in England and the USA," Lancet, **383**(9921), pp. 963–969.

[65] Pacini, D., Di Marco, L., Fortuna, D., Belotti, L. M. B., Gabbieri, D., Zussa, C., Pigini, F., Contini, A., Barattoni, M. C., De Palma, R., and Di Bartolomeo, R., 2013, "Acute Aortic Dissection: Epidemiology and Outcomes," Int. J. Cardiol., **167**(6), pp. 2806–2812.

[66] Erbel, R., Aboyans, V., Boileau, C., Bossone, E., Bartolomeo, R. Di, Eggebrecht, H., Evangelista, A., Falk, V., Frank, H., Gaemperli, O., Grabenwöger, M., Haverich, A., Iung, B., Manolis, A. J., Meijboom, F., Nienaber, C. A., Roffi, M., Rousseau, H., Sechtem, U., Sirnes, P. A., Allmen, R. S. von, Vrints, C. J. M., and ESC Committee for Practice Guidelines, 2014, "2014 ESC Guidelines on the Diagnosis and Treatment of Aortic Diseases," Eur. Heart J., **35**(41), pp. 2873–2926.

[67] Prêtre, R., and Von Segesser, L. K., 1997, "Aortic Dissection," Lancet, **349**(9063), pp. 1461–4.

[68] Roselli, E. E., 2015, "Thoracic Endovascular Aortic Repair versus Open Surgery for Type-B Chronic Dissection.," J. Thorac. Cardiovasc. Surg., **149**(2 Suppl), pp. S163-7.

[69] Palma, J. H., Augusto, J., de Souza, M., Maria, C., Alves, R., Carvalho, A. C., and Buffolo, E., 2002, "Self-Expandable Aortic Stent-Grafts for Treatment of Descending Aortic Dissections," Ann Thorac Surg, **73**, pp. 1138–1142.

[70] Appelbaum, A., Karp, R. B., and Kirklin, J. W., 1976, "Ascending vs Descending Aortic Dissections," Ann. Surg., **183**(3), pp. 296–300.

[71] Nienaber, C. A., Kische, S., Rousseau, H., Eggebrecht, H., Rehders, T. C., Kundt, G., Glass, A., Scheinert, D., Czerny, M., Kleinfeldt, T., Zipfel, B., Labrousse, L., Fattori, R., and Ince, H., 2013, "Endovascular Repair of Type B Aortic Dissection: Long-Term Results of the Randomized Investigation of Stent Grafts in Aortic Dissection Trial," Circ. Cardiovasc. Interv., **6**(4), pp. 407–416.

[72] Li, F. R., Wu, X., Yuan, J., Wang, J., Mao, C., and Wu, X., 2018, "Comparison of Thoracic Endovascular Aortic Repair, Open Surgery and Best Medical Treatment for Type B Aortic Dissection: A Meta-Analysis," Int. J. Cardiol., **250**, pp. 240–246.

[73] Mani, K., Lees, T., Beiles, B., Jensen, L. P., Venermo, M., Simo, G., Palombo, D., Halbakken, E., Troëng, T., Wigger, P., and Björck, M., 2011, "Treatment of Abdominal Aortic Aneurysm in Nine Countries 2005-2009: A Vascunet Report," Eur. J. Vasc. Endovasc. Surg., **42**(5), pp. 598–607.

[74] Findeiss, L. K., and Cody, M. E., 2011, "Endovascular Repair of Thoracic Aortic Aneurysms," Semin. Intervent. Radiol., **28**(1), pp. 107–117.

[75] Huang, C. Y., Hsu, H. L., Chen, P. L., Chen, I. M., Hsu, C. P., and Shih, C. C., 2018, "The Impact of Distal Stent Graft–Induced New Entry on Aortic Remodeling of Chronic Type B Dissection," Ann. Thorac. Surg., **105**(3), pp. 785–793.

[76] Criado, F. J., 2011, "The TEVAR Landscape in 2012," Endovasc. Today, (Figure 1), pp. 34–47.

[77] Parodi, J. C., Palmaz, J. C., and Barone, H. D., 1991, "Transfemoral Intraluminal Graft Implantation for Abdominal Aortic Aneurysms," Ann. Vasc. Surg., **5**(6), pp. 491–499.

[78] Chaikof, E. L., Dalman, R. L., Eskandari, M. K., Jackson, B. M., Lee, W. A., Mansour, M. A., Mastracci, T. M., Mell, M., Murad, M. H., Nguyen, L. L., Oderich, G. S., Patel, M. S.,

Schermerhorn, M. L., and Starnes, B. W., 2018, "The Society for Vascular Surgery Practice Guidelines on the Care of Patients with an Abdominal Aortic Aneurysm," J. Vasc. Surg., **67**(1), pp. 2-77.e2.

[79] Nienaber, C. A., Rousseau, H., Eggebrecht, H., Kische, S., Fattori, R., Rehders, T. C., Kundt, G., Scheinert, D., Czerny, M., Kleinfeldt, T., Zipfel, B., Labrousse, L., and Ince, H., 2009, "Randomized Comparison of Strategies for Type B Aortic Dissection: The INvestigation of STEnt Grafts in Aortic Dissection (INSTEAD) Trial," Circulation, **120**(25), pp. 2519–2528.

[80] Eggebrecht, H., Nienaber, C. A., Neuhäuser, M., Baumgart, D., Kische, S., Schmermund, A., Herold, U., Rehders, T. C., Jakob, H. G., and Erbel, R., 2006, "Endovascular Stent-Graft Placement in Aortic Dissection: A Meta-Analysis," Eur. Heart J., **27**(4), pp. 489–498.

[81] Sobocinski, J., Patterson, B. O., Karthikesalingam, A., and Thompson, M. M., 2016, "The Effect of Left Subclavian Artery Coverage in Thoracic Endovascular Aortic Repair," Ann Thorac Surg, **101**(2), pp. 810–7.

[82] Piffaretti, G., Rivolta, N., Fontana, F., Carrafiello, G., Mariscalco, G., and Castelli, P., 2013, "Aortic Arch Aneurysm Repair with a New Branched Device," J. Vasc. Surg., **57**(6), pp. 1664–1667.

[83] Yang, J., Liu, Y., Duan, W., Yi, D., Yu, S., Ma, R., and Ren, J., 2016, "A Feasibility Study of Total Endovascular Aortic Arch Replacement: From Stent-Graft Design to Preclinical Testing," J. Thorac. Cardiovasc. Surg., **151**(4), pp. 1203–1212.

[84] Lu, Q., Feng, J., Zhou, J., Zhao, Z., Li, H., Teng, Z., and Jing, Z., 2015, "Endovascular Repair by Customized Branched Stent-Graft: A Promising Treatment for Chronic Aortic Dissection Involving the Arch Branches," J. Thorac. Cardiovasc. Surg., **150**(6), pp. 1631-1638.e5.

[85] Appoo, J. J., and Pozeg, Z., 2013, "Strategies in the Surgical Treatment of Type A Aortic Arch Dissection.," Ann. Cardiothorac. Surg., **2**(2), pp. 205–11.

[86] Tzilalis, V. D., Kamvysis, D., Panagou, P., Kaskarelis, I., Lazarides, M. K., Perdikides, T., Prassopoulos, P., and Boudoulas, H., 2012, "Increased Pulse Wave Velocity and Arterial Hypertension in Young Patients With Thoracic Aortic Endografts," Ann. Vasc. Surg., **26**, pp. 462–467.

[87] OBrien, T., Morris, L., and McGloughlin, T., 2008, "Evidence Suggests Rigid Aortic Grafts Increase Systolic Blood Pressure: Results of a Preliminary Study," Med. Eng. Phys., **30**(1), pp. 109–115.

[88] Kadoglou, N. P. E., Moulakakis, K. G., Papadakis, I., Ikonomidis, I., Alepaki, M., Spathis, A., Karakitsos, P., Lekakis, J., and Liapis, C. D., 2014, "Differential Effects of Stent-Graft Fabrics on Arterial Stiffness in Patients Undergoing Endovascular Aneurysm Repair," J. Endovasc. Ther., **21**(6), pp. 850–858.

[89] Dong, Z. H., Fu, W. G., Wang, Y. Q., Guo, D. Q., Xu, X., and Ji, Y., 2009, "Retrograde Type A Aortic Dissection After Endovascular Stent Graft Placement for Treatment of Type B Dissection," Circulation.

[90] Pantaleo, A., Jafrancesco, G., Buia, F., Leone, A., Lovato, L., Russo, V., Di Marco, L., Di Bartolomeo, R., and Pacini, D., 2016, "Distal Stent Graft-Induced New Entry: An Emerging Complication of Endovascular Treatment in Aortic Dissection," Ann. Thorac. Surg., **102**(2), pp. 527–532.

[91] Subramanian, S., and Roselli, E. E., 2009, "Thoracic Aortic Dissection: Long-Term Results of Endovascular and Open Repair," Semin. Vasc. Surg., **22**(2), pp. 61–68.

[92] Pamler, R. S., Kotsis, T., and Go, J., 2002, "Complications After Endovascular Repair of Type B Aortic Dissection," J. Endovasc. Ther., **9**, pp. 822–828.

[93] Duarte, J. J., Pontes;, J. C. D. V., Benfatti;, R. A., Ferrachini;, A. L., Karakhanian, W. K., and Filho, Á. R., 2014, "Indication of Endovascular Treatment of Type B Aortic Dissection - Literature Review," Brazil J. Cardiovasc. Surg., **29**(3), pp. 396–401.

[94] Rubin, S., Poncet, A., and Baehrel, B., 2017, "Negative Results - Vascular Thoracic Retrograde Aortic Dissection after a Stent Graft Repair of a Type B Dissection : How to Improve the Endovascular Technique," Interact. Cardiovasc. Thorac. Surg., **5**(October), pp. 746–748.

[95] Grabenwoger, M., Fleck, T., Ehrlich, M., Czerny, M., and Hutschala, D., 2004, "Secondary Surgical Interventions after Endovascular Stent-Grafting of the Thoracic Aorta," Eur. J. Cardio-thoracic Surg., **26**, pp. 608–613.

[96] Neuhauser, B., Greiner, A., Jaschke, W., Chemelli, A., and Fraedrich, G., 2017, "Serious Complications Following Endovascular Thoracic Aortic Stent-Graft Repair for Type B Dissection," Eur. J. Cardio-thoracic Surg., **33**(October), pp. 58–63.

[97] Kizilski, S. B., Amili, O., Coletti, F., Faizer, R., and Barocas, V. H., 2018, "Identifying Properties for an Aortic Stent-Graft That Counteracts Hypertension," *2018 Design of Medical Devices Conference*, American Society of Mechanical Engineers, pp. 1–3.

[98] Benjamin, E. J., Blaha, M. J., Chiuve, S. E., Cushman, M., Das, S. R., Deo, R., de Ferranti, S. D., Floyd, J., Fornage, M., Gillespie, C., Isasi, C. R., Jiménez, M. C., Jordan, L. C., Judd, S. E., Lackland, D., Lichtman, J. H., Lisabeth, L., Liu, S., Longenecker, C. T., Mackey, R. H., Matsushita, K., Mozaffarian, D., Mussolino, M. E., Nasir, K., Neumar, R. W., Palaniappan, L., Pandey, D. K., Thiagarajan, R. R., Reeves, M. J., Ritchey, M., Rodriguez, C. J., Roth, G. A., Rosamond, W. D., Sasson, C., Towfighi, A., Tsao, C. W., Turner, M. B., Virani, S. S., Voeks, J. H., Willey, J. Z., Wilkins, J. T., Wu, J. H., Alger, H. M., Wong, S. S., and Muntner, P., 2017, "Heart Disease and Stroke Statistics — 2017 Update A Report From the American Heart Association," Circulation, **135**(10), pp. e146–e603.

[99] Pinto, E., 2007, "Blood Pressure and Ageing," Postgrad. Med. J., **83**(976), pp. 109–114.

[100] Steppan, J., Barodka, V., Berkowitz, D. E., and Nyhan, D., 2011, "Vascular Stiffness and Increased Pulse Pressure in the Aging Cardiovascular System," Cardiol. Res. Pract., **2011**, pp. 1–8.

[101] Yamashita, Y., Oishi, Y., Matsuyama, S., Ushijima, T., Fujita, S., Kimura, S., Sonoda, H., Tanoue, Y., and Shiose, A., 2021, "Determinants of Changes in Arterial Stiffness after Thoracic Endovascular Aortic Repair," Ann. Vasc. Surg., **70**, pp. 474–480.

[102] Westerhof, N., Lankhaar, J. W., and Westerhof, B. E., 2009, "The Arterial Windkessel," Med. Biol. Eng. Comput., **47**(2), pp. 131–141.

[103] Westerhof, N., and Elzinga, G., 1991, "Normalized Input Impedance and Arterial Decay Time over Heart Period Are Independent of Animal Size.," Am. J. Physiol., **261**(30), pp. R126–R133.

[104] Stergiopulos, N., Westerhof, B. E., Meister, J., and Westerhof, N., 1996, "The Four-Element Windkessel Model," 18th Annu. Int. Conf. IEEE Eng. Med. Biol. Soc., pp. 1715–1716.

[105] Stergiopulos, N., Westerhof, B. E., and Westerhof, N., 1999, "Total Arterial Inertance as the Fourth Element of the Windkessel Model," Am. J. Physiol. Circ. Physiol., **276**(1), pp. H81–H88.
[106] Saouti, N., Marcus, J. T., Vonk Noordegraaf, A., and Westerhof, N., 2012, "Aortic Function Quantified: The Heart's Essential Cushion," J. Appl. Physiol., **113**(8), pp. 1285–1291.
[107] Kokalari, I., Karaja, T., and Guerrisi, M., 2013, "Review on Lumped Parameter Method for Modeling the Blood Flow in Systemic Arteries," J. Biomed. Sci. Eng., **06**(01), pp. 92–99.
[108] Kind, T., Faes, T. J. C., Lankhaar, J. W., Vonk-Noordegraaf, A., and Verhaegen, M., 2010, "Estimation of Three- and Four-Element Windkessel Parameters Using Subspace Model Identification," IEEE Trans. Biomed. Eng., **57**(7), pp. 1531–1538.
[109] Segers, P., Stergiopulos, N., and Westerhof, N., 2000, "Quantification of the Contribution of Cardiac and Arterial Remodeling to Hypertension.," Hypertension, **36**(5), pp. 760–765.
[110] Tremblay, D., Zigras, T., Cartier, R., Leduc, L., Butany, J., Mongrain, R., and Leask, R. L., 2009, "A Comparison of Mechanical Properties of Materials Used in Aortic Arch Reconstruction," Ann. Thorac. Surg., **88**(5), pp. 1484–1491.
[111] Ettehad, D., Emdin, C. A., Kiran, A., Anderson, S. G., Callender, T., Emberson, J., Chalmers, J., Rodgers, A., and Rahimi, K., 2016, "Blood Pressure Lowering for Prevention of Cardiovascular Disease and Death: A Systematic Review and Meta-Analysis," Lancet, **387**(10022), pp. 957–967.
[112] Liu, L., Zhang, S., Lu, Q., Jing, Z., Zhang, S., and Xu, B., 2016, "Impact of Oversizing on the Risk of Retrograde Dissection After TEVAR for Acute and Chronic Type B Dissection," J. Endovasc. Ther., **23**(4), pp. 620–625.
[113] Nienaber, C. A., Fattori, R., Lund, G., Dieckmann, C., Wolf, W., von Kodolitsch, Y., Nicolas, V., and Pierangeli, A., 1999, "Nonsurgical Reconstruction of Thoracic Aortic Dissection by Stent–Graft Placement," N. Engl. J. Med., **340**(20), pp. 1539–1545.
[114] Chang, G. -q., and Li, Z. -lu., 2009, "Endovascular Stent-Graft Placement in Stanford Type B Aortic Dissection in China," Eur. J. Vasc. Endovasc. Surg., **37**(6), pp. 646–653.
[115] Foran, J. P., Jain, A. K., Casserly, I. P., Kandzari, D. E., Rocha-Singh, K. J., Witkowski, A., Katzen, B. T., Deaton, D., Balmforth, P., and Sobotka, P. A., 2015, "The ROX Coupler: Creation of a Fixed Iliac Arteriovenous Anastomosis for the Treatment of Uncontrolled Systemic Arterial Hypertension, Exploiting the Physical Properties of the Arterial Vasculature," Catheter. Cardiovasc. Interv., **85**(5), pp. 880–886.
[116] Faul, J., Schoors, D., Brouwers, S., Scott, B., Jerrentrup, A., Galvin, J., Luitjens, S., and Dolan, E., 2014, "Creation of an Iliac Arteriovenous Shunt Lowers Blood Pressure in Chronic Obstructive Pulmonary Disease Patients with Hypertension," J. Vasc. Surg., **59**(4), pp. 1078–1083.
[117] Sultan, S., Mustafa, M. K. E., Barrett, N., Hynes, N., Kundi, H., Adjedj, J., De Biase, C., Akhtar, M. M., and Thomson, R., 2020, "Midterm Complications of ROX Arteriovenous Coupler Device, Managed by Targeted Endovascular Repair: A Case Report," Eur. Hear. J. - Case Reports, **4**(4), pp. 1–5.
[118] Lobo, M. D., Ott, C., Sobotka, P. A., Saxena, M., Stanton, A., Cockcroft, J. R., Sulke, N., Dolan, E., Van Der Giet, M., Hoyer, J., Furniss, S. S., Foran, J. P., Witkowski, A., Januszewicz, A., Schoors, D., Tsioufis, K., Rensing, B. J., Scott, B., Ng, G. A., and

Schmieder, R. E., 2017, "Central Iliac Arteriovenous Anastomosis for Uncontrolled Hypertension: One-Year Results from the ROX CONTROL HTN Trial," Hypertension, **70**(6), pp. 1099–1105.

[119] Kizilski, S. B., Amili, O., Coletti, F., Faizer, R., and Barocas, V. H., 2020, "Conceptual Framework Development for a Double-Walled Aortic Stent-Graft to Manage Blood Pressure," J. Med. Device., **14**(3).

[120] Lewington, S., Clarke, R., Qizilbash, N., Peto, R., and Collins, R., 2002, "Age-Specific Relevance of Usual Blood Pressure to Vascular Mortality: A Meta-Analysis of Individual Data for One Million Adults in 61 Prospective Studies.," Lancet, **360**(9349), pp. 1903–13.

[121] Vasan, R. S., Larson, M. G., Leip, E. P., Evans, J. C., O'Donnell, C. J., Kannel, W. B., and Levy, D., 2001, "Impact of High-Normal Blood Pressure on the Risk of Cardiovascular Disease," N. Engl. J. Med., **345**(18), pp. 1291–1297.

[122] Stamler, J., Stamler, R., and Neaton, J. D., 1993, "Blood Pressure, Systolic and Diastolic, and Cardiovascular Risks: US Population Data," Arch. Intern. Med., **153**, pp. 598–615.

[123] Swerdlow, N. J., Wu, W. W., and Schermerhorn, M. L., 2019, "Open and Endovascular Management of Aortic Aneurysms," Circ. Res., **124**(4), pp. 647–661.

[124] Harky, A., Chan, J. S. K., Wong, C. H. M., and Bashir, M., 2019, "Open versus Endovascular Repair of Descending Thoracic Aortic Aneurysm Disease : A Systematic Review and Meta-Analysis," Ann. Vasc. Surg., **54**, pp. 304–315.

[125] Szeto, W. Y., McGarvey, M., Pochettino, A., Moser, G. W., Hoboken, A., Cornelius, K., Woo, E. Y., Carpenter, J. P., Fairman, R. M., and Bavaria, J. E., 2008, "Results of a New Surgical Paradigm: Endovascular Repair for Acute Complicated Type B Aortic Dissection," Ann. Thorac. Surg., **86**(1), pp. 87–94.

[126] Hansen, T. W., Staessen, J. A., Torp-Pedersen, C., Rasmussen, S., Thijs, L., Ibsen, H., and Jeppesen, J., 2006, "Prognostic Value of Aortic Pulse Wave Velocity as Index of Arterial Stiffness in the General Population," Circulation, **113**(5), pp. 664–670.

[127] Mitchell, G. F., 2014, "Recent Advances in Hypertension: Arterial Stiffness and Hypertension," Hypertension, **64**(1), pp. 13–18.

[128] Azadani, A. N., Chitsaz, S., Mannion, A., Mookhoek, A., Wisneski, A., Guccione, J. M., Hope, M. D., Ge, L., and Tseng, E. E., 2013, "Biomechanical Properties of Human Ascending Thoracic Aortic Aneurysms," Ann. Thorac. Surg., **96**(1), pp. 50–58.

[129] Sachs, T., Pomposelli, F., Hagberg, R., Hamdan, A., Wyers, M., Giles, K., and Schermerhorn, M., 2010, "Open and Endovascular Repair of Type B Aortic Dissection in the Nationwide Inpatient Sample," J. Vasc. Surg., **52**(4), pp. 860–866.

[130] Aquaro, G. D., Cagnolo, A., Tiwari, K. K., Todiere, G., Bevilacqua, S., Di Bella, G., Ait-Ali, L., Festa, P., Glauber, M., and Lombardi, M., 2013, "Age-Dependent Changes in Elastic Properties of Thoracic Aorta Evaluated by Magnetic Resonance in Normal Subjects," Interact. Cardiovasc. Thorac. Surg., **17**(4), pp. 674–679.

[131] Moulakakis, K. G., Kadoglou, N. P. E., Antonopoulos, C. N., Mylonas, S. N., Kakisis, J., Papadakis, I., Karakitsos, P., and Liapis, C. D., 2017, "Changes in Arterial Stiffness and N-Terminal pro-Brain Natriuretic Peptide Levels after Endovascular Repair of Descending Thoracic Aorta," Ann. Vasc. Surg., **38**, pp. 220–226.

[132] Vorp, D. A., Mandarino, W. A., Webster, M. W., and Gorcsan, J., 1996, "Potential Influence

of Intraluminal Thrombus on Abdominal Aortic Aneurysm as Assessed by a New Non-Invasive Method," Cardiovasc. Surg., **4**(6), pp. 732–739.

[133] Schurink, G. W. H., Aarts, N. J. M., Wilde, J., Van Baalen, J. M., Chuter, T. A. M., Kool, L. J. S., and Van Bockel, J. H., 1998, "Endoleakage after Stent-Graft Treatment of Abdominal Aneurysm: Implications on Pressure and Imaging - An in Vitro Study," J. Vasc. Surg., **28**(2), pp. 234–241.

[134] Faizer, R., Barocas, V., Coletti, F., Kizilski, S., Datta, A., and Amili, O., 2018, "Compliant Aortic Stent Grafts and Related Systems and Methods."

[135] Zamir, M., 2005, *The Physics of Coronary Blood Flow*, Springer.

[136] Cho, K. J., 2015, "Carbon Dioxide Angiography: Scientific Principles and Practice," Vasc. Spec. Int., **31**(3), pp. 67–80.

[137] Schindelin, J., Arganda-Carreras, I., Frise, E., Kaynig, V., Longair, M., Pietzsch, T., Preibisch, S., Rueden, C., Saalfeld, S., Schmid, B., Tinevez, J. Y., White, D. J., Hartenstein, V., Eliceiri, K., Tomancak, P., and Cardona, A., 2012, "Fiji: An Open-Source Platform for Biological-Image Analysis," Nat. Methods, **9**(7), pp. 676–682.

[138] Matthys, K. S., Alastruey, J., Peiró, J., Khir, A. W., Segers, P., Verdonck, P. R., Parker, K. H., and Sherwin, S. J., 2007, "Pulse Wave Propagation in a Model Human Arterial Network: Assessment of 1-D Numerical Simulations against in Vitro Measurements," J. Biomech., **40**(15), pp. 3476–3486.

[139] Team, Rs., 2019, "RStudio: Integrated Development Environment for R."

[140] Segers, P., Rietzschel, E. R., De Buyzere, M. L., Stergiopulos, N., Westerhof, N., Van Bortel, L. M., Gillebert, T., and Verdonck, P. R., 2008, "Three-and-Four-Element Windkessel Models: Assessment of Their Fitting Performance in a Large Cohort of Healthy Middle-Aged Individuals," Proc. Inst. Mech. Eng. Part H J. Eng. Med., **222**(4), pp. 417–428.

[141] Batagini, N. C., Hardy, D., Clair, D. G., and Kirksey, L., 2016, "Nellix EndoVascular Aneurysm Sealing System: Device Description, Technique of Implantation, and Literature Review," Semin. Vasc. Surg., **29**(1–2), pp. 55–60.

[142] Kizilski, S. B., Coletti, F., Faizer, R., and Barocas, V. H., 2020, "Evaluating the Effect of a Double-Walled Aortic Stent-Graft Prototype on Pulse Wave Velocity in an in Vitro Flow Loop," Front. Biomed. Devices, BIOMED - 2020 Des. Med. Devices Conf. DMD 2020, pp. 7–8.

[143] Lyle, A. N., and Raaz, U., 2017, "Killing Me Un-Softly: Causes and Mechanisms of Arterial Stiffness Recent Highlights of ATVB: Early Career Committee Contribution.," Arterioscler. Thromb. Vasc. Biol., **37**(2), pp. e1–e11.

[144] Larson, E. W., and Edwards, W. D., 1984, "Risk Factors for Aortic Dissection: A Necropsy Study of 161 Cases," Am. J. Cardiol., **53**(6), pp. 849–855.

[145] Bellini, C., Ferruzzi, J., Roccabianca, S., Di Martino, E. S., and Humphrey, J. D., 2014, "A Microstructurally Motivated Model of Arterial Wall Mechanics with Mechanobiological Implications," Ann. Biomed. Eng., **42**(3), pp. 488–502.

[146] Pasta, S., Cho, J. S., Dur, O., Pekkan, K., and Vorp, D. A., 2013, "Computer Modeling for the Prediction of Thoracic Aortic Stent Graft Collapse," J. Vasc. Surg., **57**(5), pp. 1353–1361.

[147] Storåkers, B., 1986, "On Material Representation and Constitutive Branching in Finite Compressible Elasticity," J. Mech. Phys. Solids, **34**(2), pp. 125–145.

[148] Schrodt, M., Benderoth, G., Kühhorn, A., and Silber, G., 2005, "Hyperelastic Description of Polymer Soft Foams at Finite Deformations," Tech. Mech., **25**(3–4), pp. 162–173.

[149] Horný, L., Adámek, T., and Kulvajtová, M., 2017, "A Comparison of Age-Related Changes in Axial Prestretch in Human Carotid Arteries and in Human Abdominal Aorta," Biomech. Model. Mechanobiol., **16**(1), pp. 375–383.

[150] Williams, B., Mancia, G., Spiering, W., Agabiti Rosei, E., Azizi, M., Burnier, M., Clement, D. L., Coca, A., de Simone, G., Dominiczak, A., Kahan, T., Mahfoud, F., Redon, J., Ruilope, L., Zanchetti, A., Kerins, M., Kjeldsen, S. E., Kreutz, R., Laurent, S., Lip, G. Y. H., McManus, R., Narkiewicz, K., Ruschitzka, F., Schmieder, R. E., Shlyakhto, E., Tsioufis, C., Aboyans, V., Desormais, I., De Backer, G., Heagerty, A. M., Agewall, S., Bochud, M., Borghi, C., Boutouyrie, P., Brguljan, J., Bueno, H., Caiani, E. G., Carlberg, B., Chapman, N., Cífková, R., Cleland, J. G. F., Collet, J.-P., Coman, I. M., de Leeuw, P. W., Delgado, V., Dendale, P., Diener, H.-C., Dorobantu, M., Fagard, R., Farsang, C., Ferrini, M., Graham, I. M., Grassi, G., Haller, H., Hobbs, F. D. R., Jelakovic, B., Jennings, C., Katus, H. A., Kroon, A. A., Leclercq, C., Lovic, D., Lurbe, E., Manolis, A. J., McDonagh, T. A., Messerli, F., Muiesan, M. L., Nixdorff, U., Olsen, M. H., Parati, G., Perk, J., Piepoli, M. F., Polonia, J., Ponikowski, P., Richter, D. J., Rimoldi, S. F., Roffi, M., Sattar, N., Seferovic, P. M., Simpson, I. A., Sousa-Uva, M., Stanton, A. V, van de Borne, P., Vardas, P., Volpe, M., Wassmann, S., Windecker, S., Zamorano, J. L., Windecker, S., Aboyans, V., Agewall, S., Barbato, E., Bueno, H., Coca, A., Collet, J.-P., Coman, I. M., Dean, V., Delgado, V., Fitzsimons, D., Gaemperli, O., Hindricks, G., Iung, B., Jüni, P., Katus, H. A., Knuuti, J., Lancellotti, P., Leclercq, C., McDonagh, T. A., Piepoli, M. F., Ponikowski, P., Richter, D. J., Roffi, M., Shlyakhto, E., Simpson, I. A., Sousa-Uva, M., Zamorano, J. L., Tsioufis, C., Lurbe, E., Kreutz, R., Bochud, M., Rosei, E. A., Jelakovic, B., Azizi, M., Januszewics, A., Kahan, T., Polonia, J., van de Borne, P., Williams, B., Borghi, C., Mancia, G., Parati, G., Clement, D. L., Coca, A., Manolis, A., Lovic, D., Benkhedda, S., Zelveian, P., Siostrzonek, P., Najafov, R., Pavlova, O., De Pauw, M., Dizdarevic-Hudic, L., Raev, D., Karpettas, N., Linhart, A., Olsen, M. H., Shaker, A. F., Viigimaa, M., Metsärinne, K., Vavlukis, M., Halimi, J.-M., Pagava, Z., Schunkert, H., Thomopoulos, C., Páll, D., Andersen, K., Shechter, M., Mercuro, G., Bajraktari, G., Romanova, T., Trušinskis, K., Saade, G. A., Sakalyte, G., Noppe, S., DeMarco, D. C., Caraus, A., Wittekoek, J., Aksnes, T. A., Jankowski, P., Polonia, J., Vinereanu, D., Baranova, E. I., Foscoli, M., Dikic, A. D., Filipova, S., Fras, Z., Bertomeu-Martínez, V., Carlberg, B., Burkard, T., Sdiri, W., Aydogdu, S., Sirenko, Y., Brady, A., Weber, T., Lazareva, I., Backer, T. De, Sokolovic, S., Jelakovic, B., Widimsky, J., Viigimaa, M., Pörsti, I., Denolle, T., Krämer, B. K., Stergiou, G. S., Parati, G., Trušinskis, K., Miglinas, M., Gerdts, E., Tykarski, A., de Carvalho Rodrigues, M., Dorobantu, M., Chazova, I., Lovic, D., Filipova, S., Brguljan, J., Segura, J., Gottsäter, A., Pechère-Bertschi, A., Erdine, S., Sirenko, Y., and Brady, A., 2018, "2018 ESC/ESH Guidelines for the Management of Arterial Hypertension," Eur. Heart J., **39**(33), pp. 3021–3104.

[151] "Centers for Disease Control and Prevention, National Center for Health Statistics. Underlying Cause of Death 1999-2019. Data Are from the Multiple Cause of Death Files,

1999-2019, Compiled from Data Provided by the Vital Statistics Cooperative Program.," CDC WONDER Online Database, released 2020 [Online]. Available: http://wonder.cdc.gov/ucd-icd10.html. [Accessed: 14-Jan-2021].

[152] Spadaccio, C., Nappi, F., Al-Attar, N., Sutherland, F. W., Acar, C., Nenna, A., Trombetta, M., Chello, M., and Rainer, A., 2016, "Old Myths, New Concerns: The Long-Term Effects of Ascending Aorta Replacement with Dacron Grafts. Not All That Glitters Is Gold," J. Cardiovasc. Transl. Res., **9**(4), pp. 334–342.

[153] Morris, L., Stefanov, F., Hynes, N., Diethrich, E. B., and Sultan, S., 2016, "An Experimental Evaluation of Device/Arterial Wall Compliance Mismatch for Four Stent-Graft Devices and a Multi-Layer Flow Modulator Device for the Treatment of Abdominal Aortic Aneurysms," Eur. J. Vasc. Endovasc. Surg., **51**(1), pp. 44–55.

[154] Takeda, Y., Sakata, Y., Ohtani, T., Tamaki, S., Omori, Y., Tsukamoto, Y., Aizawa, Y., Shimamura, K., Shirakawa, Y., Kuratani, T., Sawa, Y., Yamamoto, K., Mano, T., and Komuro, I., 2014, "Endovascular Aortic Repair Increases Vascular Stiffness and Alters Cardiac Structure and Function," Circ. J., **78**(2), pp. 322–328.

[155] Tzilalis, V. D., Kamvysis, D., Panagou, P., Kaskarelis, I., Lazarides, M. K., Perdikides, T., Prassopoulos, P., and Boudoulas, H., 2012, "Increased Pulse Wave Velocity and Arterial Hypertension in Young Patients With Thoracic Aortic Endografts," Ann. Vasc. Surg., **26**, pp. 462–467.

[156] Lantelme, P., Dzudie, A., Milon, H., Bricca, G., Legedz, L., Chevalier, J. M., and Feugier, P., 2009, "Effect of Abdominal Aortic Grafts on Aortic Stiffness and Central Hemodynamics," J. Hypertens., **27**(6), pp. 1268–1276.

[157] Desai, M., Bakhshi, R., Zhou, X., Odlyha, M., You, Z., Seifalian, A. M., and Hamilton, G., 2012, "A Sutureless Aortic Stent-Graft Based on a Nitinol Scaffold Bonded to a Compliant Nanocomposite Polymer Is Durable for 10 Years in a Simulated in Vitro Model," J. Endovasc. Ther., **19**(3), pp. 415–427.

[158] Chen, Y., Ding, X., Li, Y., King, M. W., Gao, J., and Zhao, X., 2012, "A Bilayer Prototype Woven Vascular Prosthesis with Improved Radial Compliance," J. Text. Inst., **103**(1), pp. 106–111.

[159] Singh, C., and Wang, X., 2014, "A Biomimetic Approach for Designing Stent-Graft Structures: Caterpillar Cuticle as Design Model," J. Mech. Behav. Biomed. Mater., **30**, pp. 16–29.

[160] Shen, X., Zhu, H., Jiang, J., Deng, Y., and Ji, S., 2019, "Multi-Objective Optimization Design of Balloon-Expandable Coronary Stent," Cardiovasc. Eng. Technol., **10**(1), pp. 10–21.

[161] Blouza, A., Dumas, L., and M'Baye, I., 2008, "Multiobjective Optimization of a Stent in a Fluid-Structure Context," GECCO'08 Proc. 10th Annu. Conf. Genet. Evol. Comput. 2008, pp. 2055–2060.

[162] Pant, S., Limbert, G., Curzen, N. P., and Bressloff, N. W., 2011, "Multiobjective Design Optimisation of Coronary Stents," Biomaterials, **32**(31), pp. 7755–7773.

[163] Alaimo, G., Auricchio, F., Conti, M., and Zingales, M., 2017, "Multi-Objective Optimization of Nitinol Stent Design," Med. Eng. Phys., **47**(2017), pp. 13–24.

[164] Blair, R. W., Dunne, N. J., Lennon, A. B., and Menary, G. H., 2019, "Multi-Objective

Optimisation of Material Properties and Strut Geometry for Poly(L-Lactic Acid) Coronary Stents Using Response Surface Methodology," PLoS One, **14**(8), pp. 1–21.

[165] Timmins, L. H., Moreno, M. R., Meyer, C. A., Criscione, J. C., Rachev, A., and Moore, J. E., 2007, "Stented Artery Biomechanics and Device Design Optimization," Med. Biol. Eng. Comput., **45**(5), pp. 505–513.

[166] Srinivas, K., Townsend, S., Lee, C. J., Nakayama, T., Ohta, M., Obayashi, S., and Yamaguchi, T., 2010, "Two-Dimensional Optimization of a Stent for an Aneurysm," J. Med. Devices, Trans. ASME, **4**(2), pp. 1–7.

[167] Stockle, J., Romero, D. A., and Amon, C. H., 2020, "Optimization of Porous Stents for Endovascular Repair of Abdominal Aortic Aneurysms," Int. j. numer. method. biomed. eng., **36**(6).

[168] Deb, K., 2011, "Multi-Objective Optimisation Using Evolutionary Algorithms: An Introduction," *Multi-Objective Evolutionary Optimisation for Product Design and Manufacturing*, Springer London, London, pp. 3–34.

[169] Ngatchou, P., Zarei, A., and El-Sharkawi, A., 2005, "Pareto Multi Objective Optimization," *Proceedings of the 13th International Conference on, Intelligent Systems Application to Power Systems*, IEEE, pp. 84–91.

[170] Tahmasbi, V., Safikhani, H., and Setoudeh, F., 2018, "Multi-Objective Pareto Optimization of Bone Drilling Process Using NSGA II Algorithm," Iran. J. Mater. Form., **5**(2), pp. 72–83.

[171] Xu, Z., Yang, M., Wang, X., and Wang, Z., 2015, "Multi-Objective Optimization of Pulsatile Ventricular Assist Device Hemocompatibility Based on Neural Networks and a Genetic Algorithm," Int. J. Artif. Organs, **38**(6), pp. 325–336.

[172] Datta, S., Zhang, Q., Sultana, N., and Mahfouf, M., 2013, "Optimal Design of Titanium Alloys for Prosthetic Applications Using a Multiobjective Evolutionary Algorithm," Mater. Manuf. Process., **28**(7), pp. 741–745.

[173] Brown, A. G., Shi, Y., Marzo, A., Staicu, C., Valverde, I., Beerbaum, P., Lawford, P. V., and Hose, D. R., 2012, "Accuracy vs. Computational Time: Translating Aortic Simulations to the Clinic," J. Biomech., **45**(3), pp. 516–523.

[174] Chiu, J. J., and Chien, S., 2011, "Effects of Disturbed Flow on Vascular Endothelium: Pathophysiological Basis and Clinical Perspectives," Physiol. Rev., **91**(1), pp. 327–387.

[175] Tricarico, R., Tran-Son-Tay, R., Laquian, L., Scali, S. T., Lee, T. C., Beck, A. W., Berceli, S. A., and He, Y., 2020, "Haemodynamics of Different Configurations of a Left Subclavian Artery Stent Graft for Thoracic Endovascular Aortic Repair," Eur. J. Vasc. Endovasc. Surg., **59**(1), pp. 7–15.

[176] Raptis, A., Xenos, M., Spanos, K., Kouvelos, G., Giannoukas, A., and Matsagkas, M., 2019, "Endograft Specific Haemodynamics After Endovascular Aneurysm Repair: Flow Characteristics of Four Stent Graft Systems," Eur. J. Vasc. Endovasc. Surg., **58**(4), pp. 538–547.

[177] Shek, T. L. T., Tse, L. W., Nabovati, A., and Amon, C. H., 2012, "Computational Fluid Dynamics Evaluation of the Cross-Limb Stent Graft Configuration for Endovascular Aneurysm Repair," J. Biomech. Eng., **134**(12), pp. 1–9.

[178] Chong, C. K., and How, T. V., 2004, "Flow Patterns in an Endovascular Stent-Graft for

Abdominal Aortic Aneurysm Repair," J. Biomech., **37**(1), pp. 89–97.
[179] Peng, L., Qiu, Y., Yang, Z., Yuan, D., Dai, C., Li, D., Jiang, Y., and Zheng, T., 2019, "Patient-Specific Computational Hemodynamic Analysis for Interrupted Aortic Arch in an Adult: Implications for Aortic Dissection Initiation," Sci. Rep., **9**(1), pp. 1–8.
[180] LaDisa, J. F. J., Dholakia, R. J., Figueroa, C. A., Vignon-Clementel, I. E., Chan, F. P., Samyn, M. M., Cava, J. R., Taylor, C. A., and Feinstein, J. A., 2011, "Stress in Aortic Coarctation Patients Treated by Resection with End-to-End Anastomosis," Congenit. Heart Dis., **6**, pp. 432–443.
[181] Knight, J., Olgac, U., Saur, S. C., Poulikakos, D., Marshall, W., Cattin, P. C., Alkadhi, H., and Kurtcuoglu, V., 2010, "Choosing the Optimal Wall Shear Parameter for the Prediction of Plaque Location-A Patient-Specific Computational Study in Human Right Coronary Arteries," Atherosclerosis, **211**(2), pp. 445–450.
[182] Stefanov, F., McGloughlin, T., and Morris, L., 2016, "A Computational Assessment of the Hemodynamic Effects of Crossed and Non-Crossed Bifurcated Stent-Graft Devices for the Treatment of Abdominal Aortic Aneurysms," Med. Eng. Phys., **38**(12), pp. 1458–1473.
[183] Ku, D. N., Giddens, D. P., Zarins, C. K., and Glagov, S., 1985, "Pulsatile Flow and Atherosclerosis in the Human Carotid Bifurcation. Positive Correlation between Plaque Location and Low and Oscillating Shear Stress," Arteriosclerosis, **5**(3), pp. 293–302.
[184] Peiffer, V., Sherwin, S. J., and Weinberg, P. D., 2013, "Does Low and Oscillatory Wall Shear Stress Correlate Spatially with Early Atherosclerosis? A Systematic Review," Cardiovasc. Res., **99**(2), pp. 242–250.
[185] Himburg, H. A., Grzybowski, D. M., Hazel, A. L., LaMack, J. A., Li, X.-M., and Friedman, M. H., 2004, "Spatial Comparison between Wall Shear Stress Measures and Porcine Arterial Endothelial Permeability," Am. J. Physiol. Circ. Physiol., **286**(5), pp. H1916–H1922.
[186] Casa, L. D. C., Deaton, D. H., and Ku, D. N., 2015, "Role of High Shear Rate in Thrombosis," J. Vasc. Surg., **61**(4), pp. 1068–1080.
[187] Deb, K., Pratap, A., Agarwal, S., and Meyarivan, T., 2002, "A Fast and Elitist Multiobjective Genetic Algorithm: NSGA-II," IEEE Trans. Evol. Comput., **6**(2), pp. 182–197.
[188] Chen, T., Tang, K., Chen, G., and Yao, X., 2012, "A Large Population Size Can Be Unhelpful in Evolutionary Algorithms," Theor. Comput. Sci., **436**, pp. 54–70.
[189] Alajmi, A., and Wright, J., 2014, "Selecting the Most Efficient Genetic Algorithm Sets in Solving Unconstrained Building Optimization Problem," Int. J. Sustain. Built Environ., **3**(1), pp. 18–26.
[190] Custódio, A. L., Madeira, J. F. A., Vaz, A. I. F., and Vicente, L. N., 2011, "Direct Multisearch for Multiobjective Optimization," SIAM J. Optim., **21**(3), pp. 1109–1140.
[191] dhadka, "Project-Platypus/Platypus."
[192] Lan, H., Updegrove, A., Wilson, N. M., Maher, G. D., Shadden, S. C., and Marsden, A. L., 2018, "A Re-Engineered Software Interface and Workflow for the Open-Source SimVascular Cardiovascular Modeling Package," J. Biomech. Eng., **140**(2), pp. 1–11.
[193] Hermes, D., 2017, "Helper for Bézier Curves, Triangles, and Higher Order Objects," J. Open Source Softw., **2**(16), p. 267.
[194] eric-yim, "Simvascular_scripts."

[195] Esmaily-Moghadam, M., Bazilevs, Y., and Marsden, A. L., 2015, "A Bi-Partitioned Iterative Algorithm for Solving Linear Systems Arising from Incompressible Flow Problems," Comput. Methods Appl. Mech. Eng., **286**, pp. 40–62.

[196] "Simulation Guide," SimVascular Dev. Team - 2017 [Online]. Available: http://simvascular.github.io/docsFlowSolver.html#solverinp. [Accessed: 14-Sep-2020].

[197] Simone, 2021, "Pareto Filtering."

[198] Fleischer, M., 2002, *The Measure of Pareto Optima : Applications to Multi-Objective Metaheuristics*.

[199] Gerges, C., Vollmers, K., Pritzker, M. R., Gainor, J., Scandurra, J., Weir, E. K., and Lang, I. M., 2020, "Pulmonary Artery Endovascular Device Compensates for Loss of Vascular Compliance in Pulmonary Arterial Hypertension," J. Am. Coll. Cardiol., **76**(19), pp. 2284–2286.

[200] Fann, J. I., 1995, "Surgical Management of Aortic Dissection During a 30-Year Period," Circulation, **92**(9), p. 9.

[201] Ma, T., Dong, Z. H., Fu, W. G., Guo, D. Q., Xu, X., Chen, B., Jiang, J. H., Yang, J., Shi, Z. Y., Zhu, T., Shi, Y., Jiang, B. H., and Xu, X. Y., 2017, "Incidence and Risk Factors for Retrograde Type A Dissection and Stent Graft-Induced New Entry after Thoracic Endovascular Aortic Repair," J. Vasc. Surg., **67**(4), pp. 1026-1033.e2.